Investigation of the dynamic response of a spar FOWT, and its sensitivity to variations in draft

University of Bergen

Faculty of Mathematics and Natural Sciences

Author: Ane Sighaug Vatshelle

Supervisor: Univ.-Prof. Finn Gunnar Nielsen

MASTER THESIS

JUNE, 2020

Acknowledgement

This 60 ECT master thesis is written as a part of the Master's program in Energy at the Geophysical institute, University of Bergen.

A special thanks to my supervisor, professor Finn Gunnar Nielsen, for his support, guidance and help during this project. Thank you for sharing your immense knowledge and for helping me develop my understanding of the dynamics of floating offshore wind turbines.

Abstract

The objective of this thesis is to investigate how the dynamic properties of a spar supported FOWT change when the draft is reduced, and what draft is needed in order to support a 10 MW wind turbine.

Design solutions of four spar-buoy concepts with drafts ranging from 60 to 120 m are identified in order to support the DTU 10 MW reference wind turbine. They are based on the "OC3-Hywind" spar, developed by the National Renewable Energy Laboratory. Modifications have been made to the wind turbine tower to make it more suitable for an offshore location. The diameter of the main hull of the spar has been adjusted to achieve the necessary stability. The designs have been modelled using a geometry modelling tool, and hydrostatic and hydrodynamic analyses have been performed using 3D potential theory. The mooring system was simplified to a horizontal stiffness component included in the restoring matrix. Analyses of the natural periods and dynamic response in surge, heave and pitch have been performed for varying environmental loads.

The dynamic response was found to increase when the draft was reduced, however, for 60 m draft it was still considered to be within acceptable limits. It is concluded that it is possible to design a shallow draft spar-buoy with the necessary stability to support a 10 MW wind turbine. This will however lead to an increased volume which would mean higher material expenses. Furthermore, a more detailed analysis of the mooring system is needed as this has a significant impact on the dynamic response.

Contents

List of Figures

List of Tables

Nomenclature

Abbreviations

BEM	Blade element momentum
CAPEX	Capital expenditure
CM	Center of mass
DNVGL	Det Norske Veritas - Germanischer Lloyd
DOF	Degree of freedom
DTU	Danmarks Tekniske Universitet
EU	European Union
FOWT	Floating offshore wind turbine
IEC	International Electrotechnical Commission
LC	Load case
MATLAB	Matrix laboratory
NREL	National Renewable Energy Laboratory
OC3	Offshore Code Comparison Collaboration
rpm	Revolutions per minute
RWT	Reference wind turbine
SWL	Still water level
TLP	Tension leg platform

Greek symbols

Δt	Time step
δ	Separation distance
ϵ	Bandwidth of notch filter
$\boldsymbol{\eta_R}$	Response vector
$\boldsymbol{\eta}$	Motion vector
η_n	Motion in n-th DOF
∇	Gradient
ω	Angular frequency
ω_e	Natural frequency
ϕ	Velocity potential
ρ	Mass density, subscript: a = air, M = material, w = water
σ	Bending stress of tower, subscript: 0 = original, new = modified
σ_u	Standard deviation of wind speed
ζ_{jj}	Linear damping ratio in j-th DOF

Latin symbols

A_R	Area swept by rotor
a_x	Horizontal acceleration
A_{kj}	Added mass matrix elements
A_{WP}	Waterplane area
$\mathbf{A}(\omega)$	Added mass matrix
$B_{kj,critical}$	Critical damping
B_{kj}	Damping matrix elements
$\mathbf{B}(\omega)$	Damping matrix
c	Decay constant, subscript: y = y-direction, z = z-direction
C_A	Added mass coefficient
C_D	Drag coefficient
C_M	Inertia coefficient
C_P	Power coefficient
C_T	Thrust coefficient
$C_{H,kj}$	Hydrostatic restoring matrix elements
C_{kj}	Restoring matrix elements
$C_{M,kj}$	Mooring restoring matrix elements
$\mathbf{C}$	Restoring matrix
Coh(δ,f)	Coherence spectrum, sub-

	script: y = y-direction, z = z-direction
D	Diameter or typical cross-sectional dimension
D_{bottom}	Bottom diameter of floater
f	Frequency
$F_{a,j}(t)$	Wave excitation force
$F_{n,drag}(t)$	Drag force in n-th DOF
$F_{n,wave}(t)$	Wave force in n-th DOF
$F_{n,wind}(t)$	Wind force in n-th DOF
F	Force vector
g	Gravitational constant
$H_a(f)$	Transfer function of exciting forces and moments
H_S	Significant wave height
I_{kj}	Mass moment of inertia elements
I_{WP}	Second moment of water plane area
k_x	Linearized horizontal mooring stiffness
L_u	Integral length scale in wind spectrum
M	Bending moment of tower, subscript: 0 = original, new = modified
m	Mass
M_H	Hydrostatic restoring moment
M_W	Overturning moment from thrust
M_{kj}	Mass matrix elements
M	Mass matrix
M	Moment vector
n	Normal vector
P	Power
R_T	Radius of rotor
r	Moment arm vector
$S_J(f)$	JONSWAP spectrum
$S_R(f)$	Excitation spectrum
$S_u(f)$	Turbulence spectrum
t	Time
T_P	Peak period
T_W	Thrust force
$T_{e,n}$	Natural period in n-th DOF
th	Wall thickness of turbine tower, subscript: 0 = original, new = modified
TI	Turbulence intensity
u_c	Wind turbulence
u_M	Mean wind speed
u_W	Wind speed
u_{10}	10-minute mean wind speed
u_{nac}	Wind speed at nacelle
u_{rel}	Relative velocity
V	Displaced volume
$\vec{V}$	Velocity vector
v_H	Horizontal velocity
V_X	Eigenvector in x-direction
V_Z	Eigenvector in z-direction
z	Vertical position, subscript: G = center of gravity, B = center of buoyancy, R = center of rotation, m = fairlead, nac = nacelle

1 Introduction

1.1 Background

Wind energy is one of the fastest growing sources of electricity production in the world and is viewed as an important contributor to lowering carbon emissions [1]. For the past years there have been an international effort to reduce the use of fossil fuels, in order to minimize the emissions of greenhouse gases. Two important agreements illustrating this are the Kyoto protocol (1997) and the Paris agreement (2015). In the European Union (EU), the " renewable energy directive" have greatly influenced the endeavor to move towards renewable energy sources. It states that by 2030, renewables must account for at least 32% of its total energy consumption [2]. In December 2019, the EU also presented "The European Green Deal" which is a roadmap for making the EU's economy sustainable, and become climate neutral (no net emissions of greenhouse gases) in 2050. It states that increasing offshore wind production will be essential to achieving this goal [3].

The first offshore wind farm, *Vindeby*, was installed in Denmark in 1991. Since then, the technology has grown rapidly, making it possible to support larger turbines, and moving them further offshore. In 2019, Europe had a total of 22.1 GW of installed offshore wind power capacity [4]. The share of renewables in the EU electricity supply have increased steadily for many years, amounting to 18 % in 2019 [5]. However, there is still a way to go to reach the 2030 targets.

Floating offshore wind turbines (FOWT) have the ability to reach areas with a very high potential for harvesting wind energy. It is estimated that 80% of the wind energy resources in Europe are located at water depths above 60 m [6]. They also allow for larger turbines, more distance between turbines (reducing the wake effect), and have less impact on the environment compared to bottom-fixed turbines.

The first fully scaled floating offshore wind turbine, *Hywind demo*, was installed in 2009 by the Norwegian company Equinor (formerly Statoil). It was followed by Principle Power's WindFloat which started production in 2011. The first floating wind farm was Hywind Scotland, which consisted of five turbines of 6 MW each, it started producing in 2017 [7]. At the end of 2019, the first turbine in the WindFloat Atlantic project was

installed. The wind farm will consist of three wind turbines of 8.4 MW each, which is the largest turbine installed on a floating platform [8]. There are many floating offshore wind projects planned in the near future [9]. The largest one is Hywind Tampen, an 88 MW floating wind farm set for completion in 2022 [10].

1.2 Support structures for offshore wind turbines

The main purpose of the support structure is to provide stability for the turbine, and to transfer the loads on the turbine to the foundation where they are absorbed. It is important that the support structure can withstand extreme and fatigue loads, and that its own resonant frequency does not coincide with the frequency of the external loads. Furthermore, the transportation and installation methods available for each structure are important in choosing a design for a specific site.

1.2.1 Bottom fixed support structures

Different bottom-fixed support structures are described below [11]. The type of structure is chosen based on several conditions, such as water depth and seabed conditions.

Gravity base

The gravity base foundation (fig. 1a) is a large concrete foundation placed on the sea floor. The weight of the foundation provides stability for the turbine. It can be a good choice for hard sea bottom conditions which does not allow for piling. The gravity-base may require seabed preparations as it must be placed on a level surface. It is typically used for water depths below 30 m.

Monopile

The monopile (fig. 1b) is a steel tube that extends deep into the seabed. With 81% of the European marked (2019), it is the most installed substructure for offshore wind turbines [4]. For sandy or sedimentary surfaces, the monopile can be hammered into the ground. For rocky surfaces, a hole must be drilled and the monopile cemented into place. The pile and turbine tower are connected using a transition piece, which also provides access to the turbine. The monopile is typically used for water depths below 30 m.

Multipods

Multipods consists of a metal frame and reinforced girders. The tripod (fig. 1c) and jacket (fig. 1d) are examples of multipods. The tripod has three legs which are anchored by piles driven into the ground. The jacket typically consists of three or four main pillars connected by girders. The multipods are most suitable for water depths between 30 and 60 m.

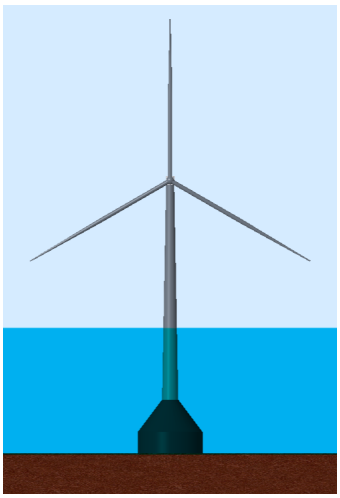

(a) Gravity-based

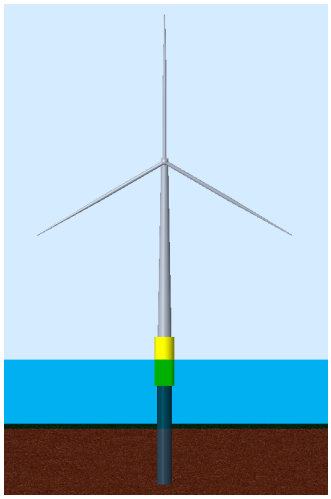

(b) Monopile

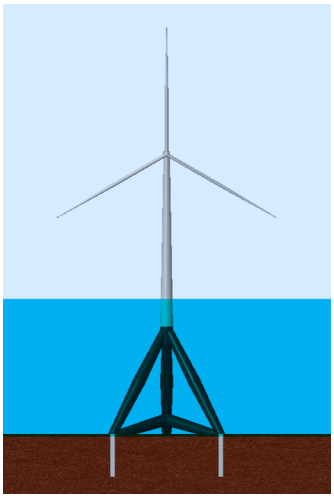

(c) Tripod

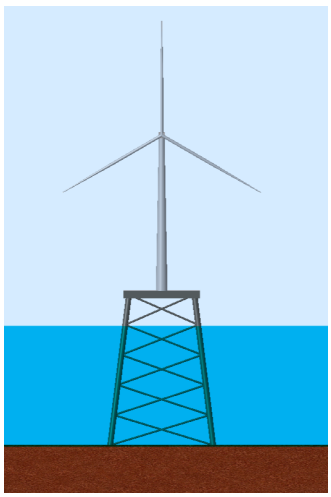

(d) Jacket

Figure 1: Bottom fixed support structures for offshore wind turbines. Figures are made based on [11]

1.2.2 Floating support structures

A floating support structure is typically used for water depths above 60 m. There are three primary concepts for how a floating platform achieves basic static stability:

- Waterplane area stabilized: shallow draft structure with a large second moment of waterplane area.
- Ballast stabilized: slender structure with a large draft. A deep placement of the ballast weight yields a large distance between the center of buoyancy and center of gravity, which counter the overturning moments.
- Mooring line stabilized/tension-leg platform: large mooring forces which prevents roll, heave and pitch motions.

Eq. 5c in sec. 2.2.1 show how the different parameters affect the static stability. This is described more thoroughly in sec. 2.2.3 and sec. 2.2.4.

Tension leg platform

The tension leg platform (TLP) is stabilized by vertical mooring lines held in tension by the buoyancy of the platform. The tensioned mooring lines makes the TLP behave like a rigid structure in the vertical plane, with very little motion response in roll, heave and pitch [12]. The first FOWT prototype, made by Blue H Engineering, was a TLP. It supported a 80 kW wind turbine and was installed off the coast of Puglia, Italy [13].

Spar platform

The spar has a slim, cylindrical shape and deep draft. It is ballast stabilized, meaning that its center of gravity is placed below its center of buoyancy. Due to its low center of gravity and slender design, it usually has a high metacentric height (see sec. 2.2.3) and small heave motions. It is a simple structure that is easy to manufacture, and has low CAPEX. However, since it requires a deep draft it is not feasible in shallow waters [11]. Hywind (fig. 2a) is an example of a spar platform supported wind turbine.

Semi-submersible platform

The semi-submersible is a buoyancy-stabilized platform. It consists of columns that are usually connected by submerged pontoons, which provides buoyancy. It can experience

large heave motions in extreme weather conditions [12]. Heave plates can be used to adjust the response in heave, as they provide added hydrodynamic mass and damping. One of the main advantages of the semi-submersible is that it can operate in a wide range of water depths [14]. Principle Power's "WindFloat" (fig. 2b) and Dr. Techn. Olav Olsen's "OO-Star-Wind" are examples of semi-subs.

Barge

Ideol has created a 2 MW demonstrator floating wind turbine, FloatGen (fig. 2c), supported by a barge-like structure called a "Damping Pool". It is a ring shaped structure made in concrete, with a shallow draft of 7.5 m. The FloatGen demonstrator has been in commission since 2018 [15].

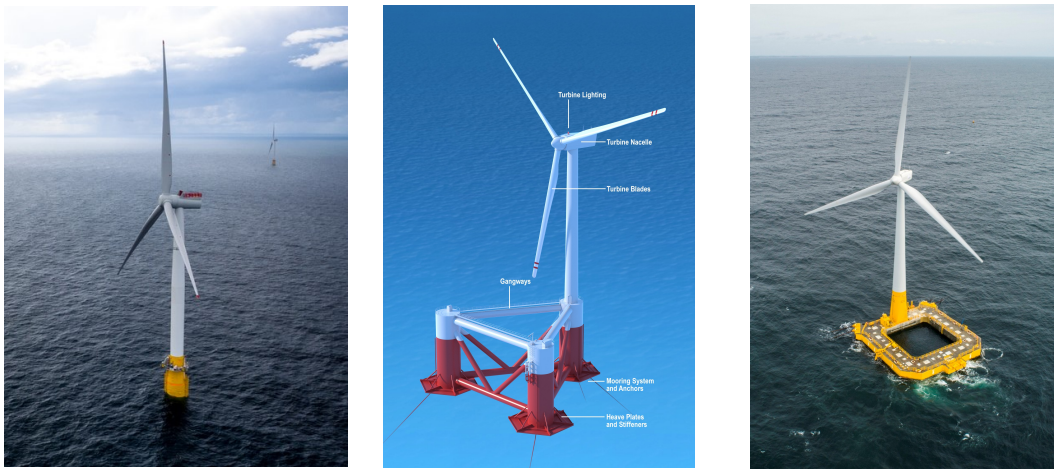

(a) Hywind [16] (b) WindFloat [17] (c) FloatGen [18]

Figure 2: Floating support structures

1.3 Thesis overview

1.3.1 Aim

The aim of this thesis is to contribute towards finding better solutions for floating offshore wind power systems.

1.3.2 Objectives

This master thesis will look further into the spar-platform concept. As previously mentioned, the spar requires a deep draft in order to obtain stability. The objective of this thesis is to investigate how the dynamic properties of the spar-platform change when the draft is reduced, and what draft is needed in order to support a 10 MW wind turbine.

This objective is achieved by:

- Determining key design criteria
- Identify possible design solutions for different drafts
- Identify natural periods
- Perform dynamic analyses in wind and waves

The turbine and floater described below will be used as a basis to create models featuring different drafts, based on chosen design criteria. The models will then be tested to obtain hydrostatic and hydrodynamic properties, in order to identify natural periods and investigate the movements of the systems in wind and waves.

Thesis overview:

Chapter 1 is an introduction to offshore wind, including an overview of different support structures. It also presents the aim and structure of the thesis.

Chapter 2 presents the relevant theory within aerodynamics, hydrostatics and hydrodynamics, used to solve this project.

Chapter 3 describes the methods used in defining and modelling the systems, defining environmental loads and performing the analyses.

Chapter 4 presents the results obtained from the analyses.

Chapter 5 and 6 provides a discussion and conclusion of the findings of the thesis, and recommendations for future work.

1.3.3 Properties of the OC3-Hywind floater

The spar-platform in this thesis is based on the OC3-Hywind spar. The OC3 (Offshore Code Comparison Collaboration) was established to test and verify areo-servo-elastic codes developed for offshore installations. The project investigated several support structures, all supporting the NREL 5MW wind turbine. A detailed description of the spar-platform system is provided in [19]. The key properties are listed in tab. 1.

Depth to Platform Base Below SWL (Total Draft)	120 m
Elevation to Platform Top (Tower Base) Above SWL	10 m
Depth to Top of Taper Below SWL	4 m
Depth to Bottom of Taper Below SWL	12 m
Platform Diameter Above Taper	6.5 m
Platform Diameter Below Taper	9.4 m
Platform mass, Including Ballast	7.466E06 kg
CM Location Below SWL Along Platform Centerline	89.9155 m
Platform Roll and Pitch Inertia about CM	4.229E09 kg*m^2
Platform Yaw Inertia about Platform Centerline	0.164E09 kg*m^2

Table 1: Description of the Hywind OC3 floating system, from [19]. *SWL = still water level, CM = center of mass*.

1.3.4 Properties of the DTU 10MW turbine and tower

The DTU 10 MW reference wind turbine (RWT) is used for analyses of the spar floater in this thesis, it is described in [20]. The turbine is developed by the Technical University of Denmark, and consists of a 10 MW reference rotor, blades, support tower and drive train. It was developed as a part of the "Light Rotor Project" and is meant as a basis for design of new and optimized rotors. The design is based on the NREL 5 MW reference turbine, which was used in the definition of the Hywind OC3. The key parameters for the DTU 10 MW RWT are listed in tab. 2. The turbine is designed for an onshore location.

The tower is 115.63 m high (from the ground), with an outer diameter that decrease linearly from 8.3 m at the bottom to 5.5 m at the top. The tower is modelled in 10 sections

with different wall thicknesses. The material used is steel S355 with a mass density of $\rho_M = 7850kg/m^3$. The material density is increased to $\rho_M = 8500kg/m^3$ in the analyses to account for the mass of secondary structures ([20]). The total mass of the tower is 628,442 kg.

Parameter	DTU 10MW RWT
Wind Regime	IEC Class 1A
Rotor Orientation	Clockwise rotation - Upwind
Control	Variable Speed
Cut in wind speed	4 m/s
Cut out wind speed	25 m/s
Rated wind speed	11.4 m/s
Rated power	10 MW
Number of blades	3
Rotor Diameter	178.3 m
Hub Diameter	5.6 m
Hub Height (from ground)	119.0 m
Drivetrain	Medium Speed, Multiple-Stage Gearbox
Minimum Rotor Speed	6.0 rpm
Maximum Rotor Speed	9.6 rpm
Maximum Generator Speed	480.0 rpm
Gearbox Ratio	50
Maximum Tip Speed	90.0 m/s
Hub Overhang	7.1 m
Shaft Tilt Angle	5.0 deg
Rotor Precone Angle	-2.5 deg
Blade Prebend	3.332 m
Rotor Mass	227,962 kg
Nacelle Mass	446,036 kg
Tower Mass	628,442 kg

Table 2: Key parameters of the DTU 10 MW reference wind turbine, from [20].

2 Theoretical background

2.1 Properties of wind turbines

2.1.1 Main components

Fig. 3 shows the main components of a horizontal axis wind turbine. The rotor blades are connected to the hub, which is connected to the rotor shaft. Some wind turbines are equipped with a blade pitch control system (described below), which is embedded in the hub. This system adjusts the angle of attack, and thus the input power. This is done to ensure that the turbine does not exceed its maximum rotational speed.

The nacelle houses the drive-train and the yaw system. The yaw system enables the rotor to be turned into the wind. The drive-train converts the kinetic energy from the rotating blades into electricity. Most turbines include a gearbox that connects the rotor to the generator. Traditionally, this configuration was associated with a lower weight and could be assembled using standard components. In recent years, a direct drive system using permanent magnets have become more popular. Due to developments in design, the weight argument against a direct drive system has been nearly eliminated. Studies show that both these drive train configurations have the potential to become dominant [21].

2.1.2 Power curve

The power curve (see fig. 4) show the power output of a wind turbine as a function of wind speed. The cut-in wind speed is the wind speed at which the turbine starts to rotate to produce power. The rated wind speed is where the turbine reaches its nominal power. Below rated speed the blade pitch is kept constant and the rotational speed increase with increasing wind speed to achieve maximum efficiency. Above rated speed, the rotational speed is controlled by the blade pitch angle and the effect is kept constant. At cut-out wind speed the turbine shuts down to avoid damage.

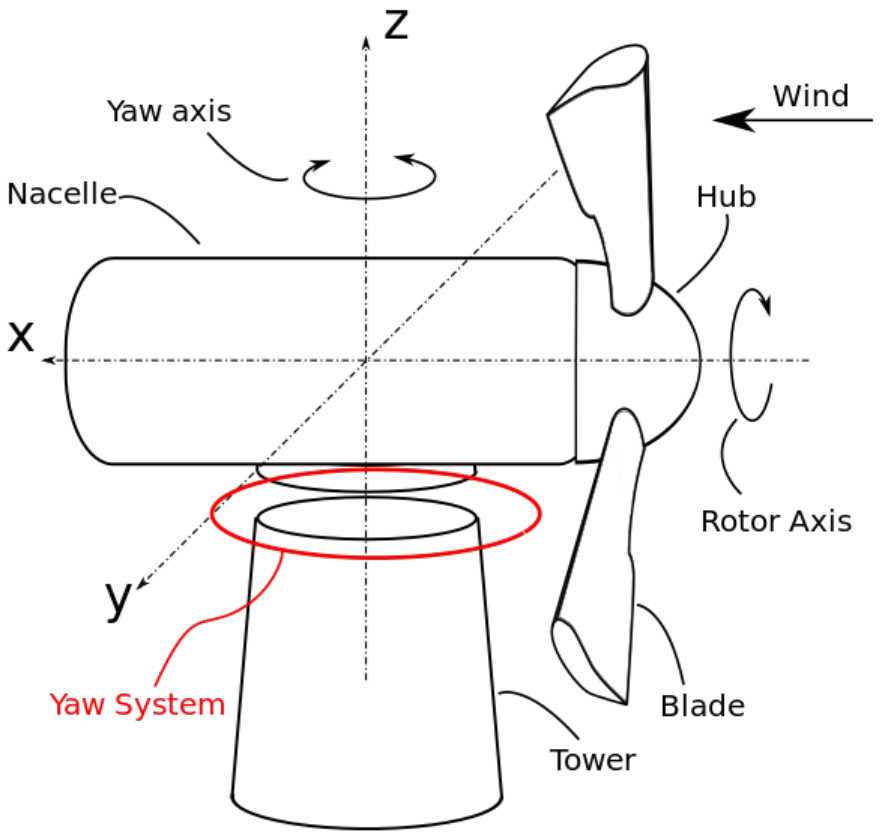

Figure 3: Main components of a wind turbine, from [22]

2.1.3 Extracting energy

A wind turbine extracts kinetic energy from the wind. The maximum power that can be extracted is given by Betz's law, which is described in [24]. This theory uses the continuity equation, Bernoulli's equation and the law of conservation of momentum to calculate the power available for extraction. This power output is given by the equation:

$$P = \frac{1}{2} C_P \rho_a A_R u_W^3 \tag{1}$$

Where C_P is the power coefficient, ρ_a is the air mass density, A_R is the area swept by the rotor and u_W is the wind speed. The power coefficient accounts for the disturbance in the air flow due to the converter. The maximum value of C_P is $\frac{16}{27}$, which is known as the Lanchester-Betz limit.

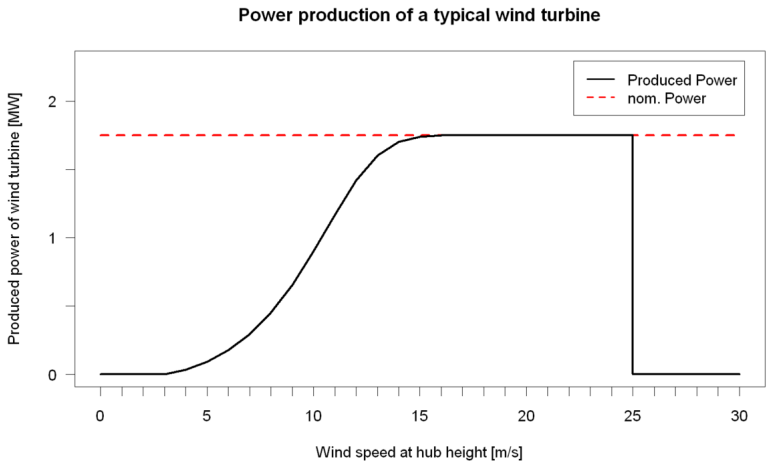

Figure 4: Power curve for a typical wind turbine, from [23]

2.1.4 Variations in wind speed

The wind consists of two components, the steady (mean) and the fluctuating (turbulence), ($u_W = u_M + u_C$). The mean wind speed is usually defined as averaged over 1 minute, 10 minutes or 1 hour [25]. The mean wind speed varies with height, as it is affected by friction from the earth's surface. This variation becomes smaller with height. The standard deviation (σ_u) is a measure of how the wind varies about the mean, in the direction of the mean, at the specified height. The turbulence intensity (TI) is defined as σ_u / u_M.

The variation in wind in the longitudinal direction can be modelled using the Kaimal spectrum, as described in DNV-RP-C205 [25]. The spectral density is given by the following expression:

$$S_u(f) = \sigma_u^2 \frac{6.868 \frac{L_u}{u_{10}}}{\left(1 + 10.32 \frac{f L_u}{u_{10}}\right)^{5/3}} \tag{2}$$

Where u_{10} is the 10-minute mean wind speed, f is the frequency and L_u is the integral length scale, which can be estimated as [25]:

$$L_u = \begin{cases} 3.33z & \text{for z} < 60 \text{ m} \\ 200m & \text{for z} \geq 60 \text{ m} \end{cases}$$

Where z is the wind speed reference height.

The wind speed in the longitudinal direction also varies vertically and laterally. This means that the wind field is not necessarily homogeneous over the entire wind turbine rotor. The spatial coherence of wind speed can be calculated using the Davenport coherence function (eq. 3).

$$Coh(\delta, f) = exp\left(-cf\frac{\delta}{u_M}\right) \tag{3}$$

Where δ is the separation distance, u_M is the mean wind speed at the considered height and c is the decay constant.

Tab. 3 show the vertical (z) and lateral (y) coherence of the wind speed in the longitudinal (x) direction, relevant to the investigated wind turbine, for different mean wind speeds. Here the separation distance is set equal to 0.7 times the rotor diameter and the frequency is set to 1/100 Hz, which is the largest typical natural frequency for floaters. The mean wind speeds and associated decay constants are taken from [26].

u_M [m/s]	c_z	Coh_z	c_y	Coh_y
7.5	3.8	0.53	6.6	0.33
12.5	4.7	0.63	8.1	0.45
18	6.3	0.65	7.7	0.59

Table 3: Coherence of wind speeds over rotor for f = 1/100 Hz

For simplicity, the spatial variability is omitted in this thesis, which means it assumes that the wind speed is fully coherent (Coh = 1) over the rotor. This is clearly not the case, as shown in tab. 3, which means that this will cause some uncertainties in the results. The significance of wind variability and coherence for the response of FOWT are investigated in [27, 28].

2.2 Properties of floating structures

The motions of a rigid floating body are defined as follows (fig. 5).

- **Surge** (η_1): translation along the longitudinal axis (x-axis), (1)
- **Sway** (η_2): translation along the transverse axis (y-axis), (2)
- **Heave** (η_3): translation along the vertical axis (z-axis), (3)
- **Roll** (η_4): rotation about the longitudinal axis, (4)
- **Pitch** (η_5): rotation about the transverse axis, (5)
- **Yaw** (η_6): rotation about the vertical axis, (6)

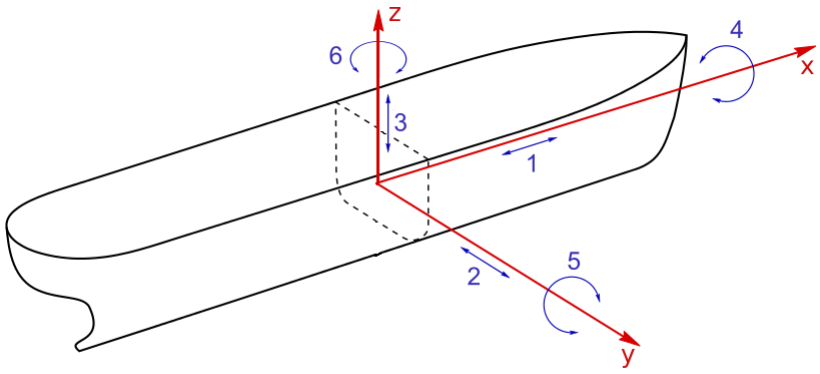

Figure 5: Definition of ship motions, from [29]

2.2.1 Equation of motion

The equation of motion for a rigid floating body are described in [30], and the mass and hydrostatic restoring matrices are given in DNV-RP-C205 [25]. The linear equation of motion for a rigid floating body can be expressed in matrix form as:

$$\boldsymbol{F}(\omega) = (\boldsymbol{M} + \boldsymbol{A}(\omega))\ddot{\boldsymbol{\eta}} + \boldsymbol{B}(\omega)\dot{\boldsymbol{\eta}} + \boldsymbol{C}\boldsymbol{\eta} \tag{4}$$

Since the added mass and damping matrices are frequency dependant, the force must be calculated for each frequency when using this equation. For a six degrees of freedom (DOF) system, the matrices are 6x6 matrices. The terms of the equation are called:

- $\boldsymbol{F}(\omega)$: excitation force
- $(\boldsymbol{M} + \boldsymbol{A}(\omega))\ddot{\boldsymbol{\eta}}$: inertial force

- $\boldsymbol{B}(\omega)\dot{\boldsymbol{\eta}}$: damping force
- $\boldsymbol{C}\boldsymbol{\eta}$: restoring force

The dry mass matrix, for a body with a centre of gravity at $(0, 0, z_G)$, can be written as:

$$\mathbf{M} = \begin{bmatrix} m & 0 & 0 & 0 & mz_G & 0 \\ 0 & m & 0 & -mz_G & 0 & 0 \\ 0 & 0 & m & 0 & 0 & 0 \\ 0 & -mz_G & 0 & I_{44} & 0 & 0 \\ mz_G & 0 & 0 & 0 & I_{55} & 0 \\ 0 & 0 & 0 & 0 & 0 & I_{66} \end{bmatrix}$$

Where m is the dry mass of the body, and the I-terms are the mass moments of inertia.

The added mass is a part of the force that acts on the body due to pressure in the water when the body is accelerating. It is frequency dependent and determined by numerical methods (see sec. 2.3.2).

The restoring matrix consists of hydrostatic stiffness and possible additional stiffness, e.g. from mooring. The hydrostatic stiffness matrix is dependent on the geometry of the body. The $\mathrm{C}_{H,11}$, $\mathrm{C}_{H,33}$ and $\mathrm{C}_{H,55}$ terms are given by:

$$C_{H,11} = 0 \tag{5a}$$

$$C_{H,33} = \rho_W g A_{WP} \tag{5b}$$

$$C_{H,55} = \rho_W g(I_{WP} + V z_B) - mgz_G \tag{5c}$$

Where V is the displaced volume of the body, A_{WP} is the waterplane area, I_{WP} is the second moment of the waterplane area and z_B is the vertical distance to the center of buoyancy. The complete hydrostatic stiffness matrix can be found in [25].

Another contribution to the restoring matrix is the mooring system. The natural period in surge, sway and yaw are determined by the mooring stiffness, as there are no hydrostatic stiffness associated with these DOF. The placement of the mooring line attachment point (fairlead) affects both the natural periods and response of the floater. Here it is relevant to

mention the center of rotation, which is the point about which the floater rotates. When the fairleads are placed at the center of rotation, there are no surge-pitch and sway-roll coupling. The coupling increase as the fairleads are placed further away from this point.

The vertical center of rotation z_R can be found from the roll/pitch eigenvectors:

$$z_R = -\frac{V_x}{V_z} \tag{6}$$

Where V_x and V_z are the roll/pitch eigenvectors in x- and z-direction, respectively.

The damping is also frequency dependant. It consists of potential damping due to waves forming at the surface, and viscous damping due to friction and vortices. These can be calculated using potential theory and Morison theory (see sec. 2.3). For FOWT the wind turbine and wind force can also contribute to damping [31, 32].

The damping ratio is a measure of the damping, and describes how the oscillations of a vibrating system decay. The linear damping ratio in j-th DOF is given by:

$$\zeta_{jj} = \frac{B_{jj}}{B_{jj,critical}} \tag{7}$$

where

$$B_{jj,critical} = 2\sqrt{(M_{jj} + A_{jj})C_{jj}} \tag{8}$$

2.2.2 Natural frequency

The natural frequency is the frequency at which a system will vibrate freely. If an external force with a frequency equal to the natural frequency is applied, it can cause violent vibrations, known as resonance. Thus it is important to avoid natural frequencies within the high energy part of the wave spectra ($\sim$5 - 25s).

The natural frequency (ω_e) and natural period (T_e) is related by:

$$T_e = \frac{2\pi}{\omega_e} \tag{9}$$

The undamped natural frequency (**B** = 0) can be found by assuming an harmonic solution ($\boldsymbol{\eta} = \boldsymbol{\eta_s} sin(\omega t)$) to eq. 4 [33]. Then the equation can be simplified to:

$$(-(\boldsymbol{M} + \boldsymbol{A}(\omega))\omega^2 + \boldsymbol{C})\boldsymbol{\eta_s} = 0 \tag{10}$$

And the expression for ω becomes:

$$\omega_i = \sqrt{\frac{C_i}{M_i + A_i}} \tag{11a}$$

The equations for natural periods in surge ($T_{e,1}$) , heave ($T_{e,3}$) and pitch ($T_{e,5}$) are written out below. These are representative for the spar-floater system investigated in this thesis.

$$T_{e,1} = 2\pi\sqrt{\frac{2a}{-b - \sqrt{b^2 - 4ac}}}, \quad T_{e,3} = 2\pi\sqrt{\frac{M_{33} + A_{33}}{C_{33}}}, \quad T_{e,5} = 2\pi\sqrt{\frac{2a}{-b + \sqrt{b^2 - 4ac}}}$$

Where:

$$a = (M_{11} + A_{11})(I_{55} + A_{55}) - (M_{15} + A_{15}^2)$$

$$b = -C_{11}(I_{55} + A_{55}) - C_{55}(M_{11} + A_{11}) + 2C_{15}(M_{15} + A_{15}^2)$$

$$c = C_{11}C_{55} - C_{15}^2 \tag{12a}$$

The above natural periods in surge and pitch are coupled, while the natural period in heave is uncoupled. When the center of reference is close to the vertical center of gravity ($z_G \approx 0$) and the mooring lines are connected at the vertical center of rotation, surge and pitch are almost uncoupled. Then their natural periods can be calculated in the same manner as for heave. When there is no mooring system present, the natural periods in surge, sway and yaw approaches infinity, as there are no hydrostatic stiffness associated with these degrees of freedom.

Typical natural periods of deep water floaters are given in tab. 4. As seen, these are designed to lie outside the range of 5 - 20 s, to avoid wave frequencies associated with significant wave energy.

Mode	Spar	TLP	Semi-sub.
Surge	> 100	> 100	> 100
Sway	> 100	> 100	> 100
Heave	20 - 35	< 5	20 - 50
Roll	50 - 90	< 5	30 - 60
Pitch	50 - 90	< 5	30 - 60
Yaw	> 100	> 100	> 50 - 60

Table 4: Typical natural periods [s] of deep water floaters, from [25]

2.2.3 Stability

DNVGL describes the stability requirements for a FOWT [34]. It states that "the floating structure shall be capable of maintaining stability during operation of the wind turbine at the wind speed that produces the largest rotor thrust". Furthermore, for Spar buoys it is required that the metacentric height is greater than 1.0 m.

The basic stability of a floating body is described in [35]. The metacenter (M), center of gravity (G) and center of buoyancy (B) are defined in fig. 6. The metacentric height can be given as:

$$GM = KB + BM - KG \tag{13}$$

Where K is the keel, which is the bottom central part of the hull.

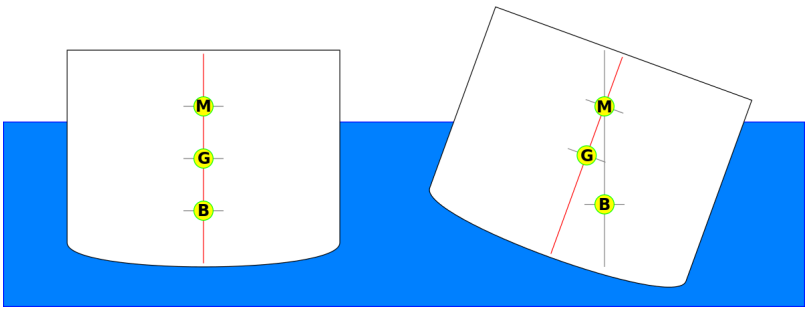

Figure 6: Metacentric height of a floating structure, from [36].

The distance between the center of buoyancy and the metacenter can be found from:

$$BM = \frac{I_{WP}}{V} \tag{14}$$

Due to its slender design (the waterplane area is very small relative to its displaced volume), the BM for a spar buoy is very small. Hence, for small angles (< 10 °) the metacentric height is approximately equal to the distance between the center of gravity (z_G) and center of buoyancy (z_B).

Since the spar platform is a ballast stabilized platform, its stability is sensitive to changes in draft and ballast placement.

2.2.4 Static pitch

Steady wind forces induce a static heeling of the wind turbine, here referred to as "static pitch". When moored, the restoring forces acts from the mooring line attachment point. Hence, the overturning moment is given by:

$$M_W = T_W(z_{nac} - z_m) \tag{15}$$

Where T_W is the thrust force, z_{nac} is the nacelle height (hub height) and z_m is the vertical distance to the mooring line attachment point.

The overturning moment is balanced by the hydrostatic restoring moment (eq. 16), which can be found from the hydrostatic restoring coefficient (not taking into account the contribution from mooring).

$$M_H = C_{H,55}\eta_5 \tag{16}$$

$C_{H,55}$ is defined in eq. 5c. As previously mentioned, the spar buoy is a slender structure so the moment of the waterplane area (I_{WP}) can be neglected:

$$C_{H,55} \approx \rho_W g V z_B - mgz_g = mg(z_B - z_G) \tag{17}$$

Eq. 16 can then be simplified to:

$$M_H \approx mg(z_B - z_G)\eta_5 \tag{18}$$

For a moment equilibrium ($M_W = M_H$), η_5 can be obtained as:

$$\eta_5 = \frac{M_W}{C_{H,55}} \approx \frac{T_W(z_a - z_m)}{mg(z_B - z_G)} \tag{19}$$

2.3 Calculation of hydrodynamic forces

Structures subjected to hydrodynamic loads are often classified as small volume or large volume structures. For large volume structures the characteristic length (width/diameter) is comparable to the wavelength, and thus the pressure on the structure affects the surrounding wave field. For these structures, wave diffraction loads are much larger than drag induced loads. This is usually defined to be for wavelengths smaller than five times the characteristic length [30].

2.3.1 Morison's equation

Morison's equation [30] can be used to calculate hydrodynamic forces on small volume structures. It is typically used for long slender cylinder elements, where the diameter is much smaller than the wave length. Morison equation is a semi-empirical equation. It is given as the sum of two force components, an inertia force and a drag force. The inertia force is in phase with the acceleration of the flow, and the drag force is proportional with the square of the flow velocity. For a vertical cylinder, the horizontal force acting on a strip with length dz, is given as:

$$dF = \rho_W \frac{\pi D^2}{4} C_M a_x dz + \frac{1}{2}\rho_W C_D D u_{rel} \mid u_{rel} \mid dz \tag{20}$$

Where D is the diameter (or width) of the structure, a_x is the horizontal acceleration, u_{rel} is the relative horizontal velocity between the water and body, and C_M and C_D are the inertia- and drag coefficients.

The inertia coefficient includes the added mass coefficient ($C_M = 1 + C_A$), which accounts for the deflection of surrounding fluid due to acceleration. The drag coefficient is a function of Reynold's number and Keulegan-Carpenter number, which both describe the importance of viscous forces over inertial forces. Recommended values can be found in e.g. DNVGL-RP-C205 [25].

The relative horizontal velocity used to calculate the drag force is given as:

$$u_{rel} = v_h - \dot{\eta_1} - \dot{\eta_5} z_{nac} \tag{21}$$

Where v_h is the horizontal velocity of the water. The drag force contributes both to excitation through the v_h term, and damping through the $-\dot{\eta_1} - \dot{\eta_5} z_{nac}$ term.

2.3.2 Potential flow theory

Potential flow theory [37] can be used to calculate wave loads on large volume structures, where the viscous effects are negligible. The potential flow theory assumes an ideal (inviscid) fluid, which is incompressible and irrotational. Then the linearized Bernoulli's equation can be applied to obtain the pressure acting on the structure. A detailed description of the potential theory for calculating wave loads can be found in [38].

The velocity vector ($\vec{V}$) is given by the velocity potential (ϕ(x,y,z,t)):

$$\vec{V} = -\nabla\phi \tag{22}$$

Thus, the velocity components become:

$$u = -\frac{\partial\phi}{\partial x}, \qquad v = -\frac{\partial\phi}{\partial y}, \qquad w = -\frac{\partial\phi}{\partial z},$$

This definition of the velocity potential ensures that the irrotational condition is satisfied, since $curl(grad(\phi)) \equiv 0$.

The forces and moments are obtained by integrating the dynamic pressure of the fluid

over the body surface:

$$\mathbf{F} = -\rho_W \iint_{S_B} \left[\frac{\partial \phi}{\partial t} + \frac{1}{2} \nabla \phi \cdot \nabla \phi \right] \mathbf{n} dS \tag{23a}$$

$$\mathbf{M} = -\rho_W \iint_{S_B} \left[\frac{\partial \phi}{\partial t} + \frac{1}{2} \nabla \phi \cdot \nabla \phi \right] (\mathbf{r} \times \mathbf{n}) dS \tag{23b}$$

The quadratic terms are neglected in linear theory. The integral is calculated over the mean position of the body and up to the mean free surface. Potential theory can be solved in the frequency domain and thus used to find the frequency dependent added mass and damping coefficients.

2.4 Modelling and analyses software

This thesis utilizes software from Sesam for modelling and hydrodynamic analyses, and purpose made MATLAB routines for analyses of dynamic response. Sesam is a software suit provided by DNVGL used for hydrodynamic and structural analyses of ships and offshore structures.

2.4.1 Modelling

GeniE [39] is a modelling tool that allows you to make finite element models. A panel model is always required to perform hydrodynamic analyses. This model describes the geometry of the hull of the floating structure. The panel model also has to include a defined wet surface and an associated hydro pressure loadcase, in order to compute hydrodynamic loads and accelerations.

A structural model can also be made in GeniE. This model can be built from structural mass and/or specifically given point masses. The masses of the structure can also be given directly as input in HydroD.

GeniE also has a built in compartment manager that identifies void spaces in the structure and saves them as compartments. These compartments may be viewed and filled in HydroD

2.4.2 Hydrodynamic analysis

HydroD is a tool used for hydrostatic and stability analyses. It implements Wadam to compute wave loads and motion response. Wadam is used for calculating wave-structure interaction. It uses Morisons equation and MacCamy and Fuchs theory for slender structures, and first and second order 3D potential theory for large volume structures. More information on the software can be found in [40] and [41].

HydroD calculates the hydrostatic properties from the panel and mass model, including center of gravity, center of buoyancy, displaced volume, waterplane area, metacentric height and the global hydrostatic restoring coefficients. In this project, the global mass matrix is calculated from a structural model. Wadam calculates the frequency dependent added mass and damping matrices from potential theory. The output from Wadam also includes transfer functions for exciting forces/moments and motion responses in the frequency domain. The transfer functions are normalised by the wave amplitude. This project did not include a Morison model in the hydrodynamic analyses, the relevant calculations are performed using linear potential theory for large volume structures.

3 Methods

The design and analyses process is presented as a flowchart in fig. 7. Four spar floaters with different drafts are established to support the DTU 10 MW turbine. Models of the four systems are made in GeniE, and are used to obtain hydrostatic properties and perform hydrodynamic analyses in HydroD. The dry and added mass matrices, potential damping matrix, hydrostatic restoring matrix and excitation forces are found from the hydrodynamic analyses. Load cases are determined and used to make time series of the horizontal wind, and the wave forces. This is then used as input in the dynamic analyses performed in MATLAB, to calculate the natural periods and dynamic response.

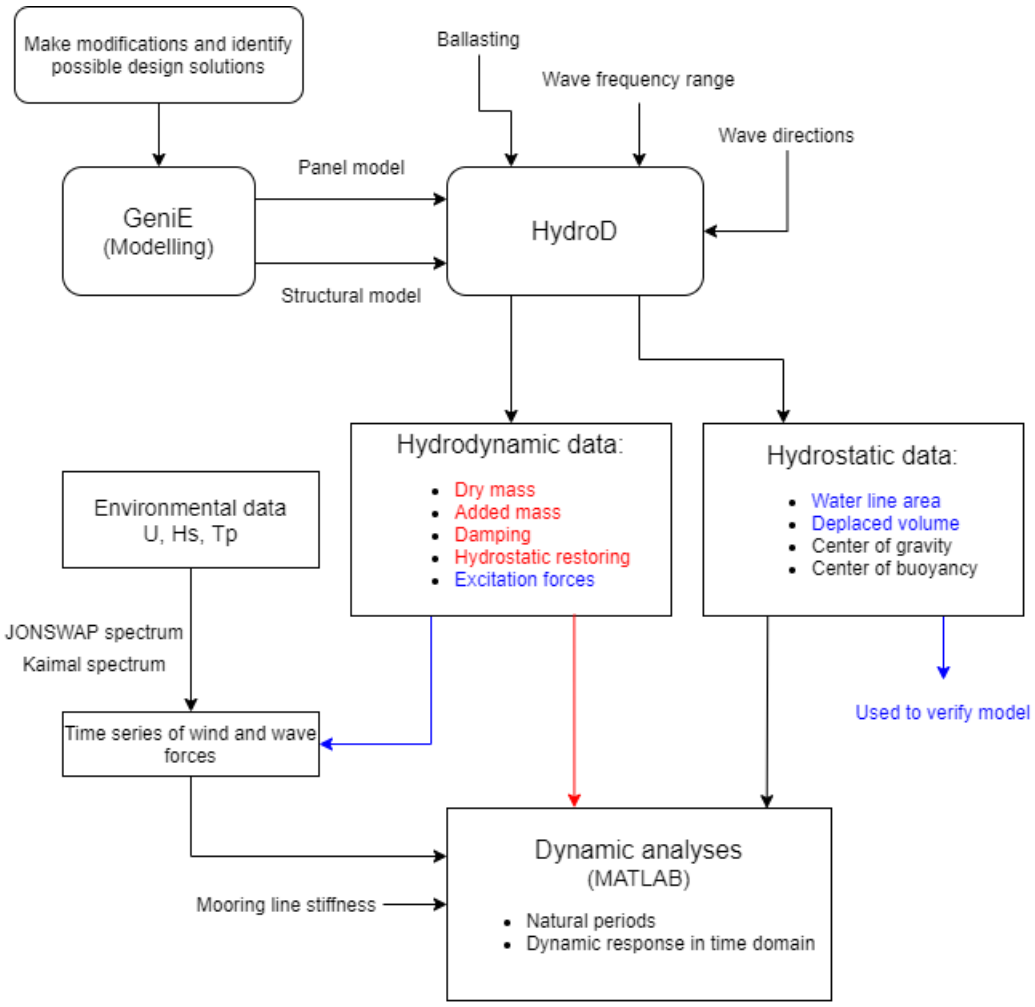

Figure 7: Flowchart describing the design and analyses process

3.1 Modifications of spar floater and tower

To modify the tower and determine the design of the floaters, a maximum static pitch angle of six degrees when subjected to the the maximum thrust force, is set as a design criteria.

3.1.1 Tower

The tower supporting the turbine is described in [20]. The tower is originally designed for an onshore location, and needs to be modified to withstand the additional bending stress from heeling. For the original tower, the contributors are the maximum thrust force and a small offset of the center of mass of the rotor ($x_{g,rotor}$) (eq. 24a). For the modified tower, the bending moment from the weight of the tower when heeling is added (eq. 24b).

$$M_0 = T_{W,max} z_{nac} + m_{rotor} x_{g,rotor} g \tag{24a}$$

$$M_{new} = M_0 + (m_{rotor} z_{g,rotor} + m_{tower} z_{g,tower}) g \eta_5 \tag{24b}$$

The wall thickness is increased so that at a heeling angle of six degrees, the new bending stress does not exceed the bending stress of the original tower. This is a simplified method to determine the necessary wall thickness, but is considered adequate for the purpose of this thesis. The new wall thickness is calculated as a function of the original wall thickness multiplied by a linear function of the height (z) from the base of the tower (eq. 25).

$$th_{new} = th_0 * (az + b) \tag{25}$$

Fig. 8 show the bending stress of the original and modified tower. The overall bending stress is highest at z $\approx$ 50m. This is due to the defined variations in outer diameter and thickness. The bending stress from heeling is highest at the base of the tower and decreases with height, hence the increase in thickness is largest at base and also decrease with height. The thicknesses are given in tab. 5.

Additionally, since the floater extends 10 m above SWL, the height of the tower is cut by 10 m to attain the correct hub height. That is why there is a horizontal offset between the

curves in fig. 8. The mass of the modified tower is 859 ton, an increase of 37% compared to the original tower.

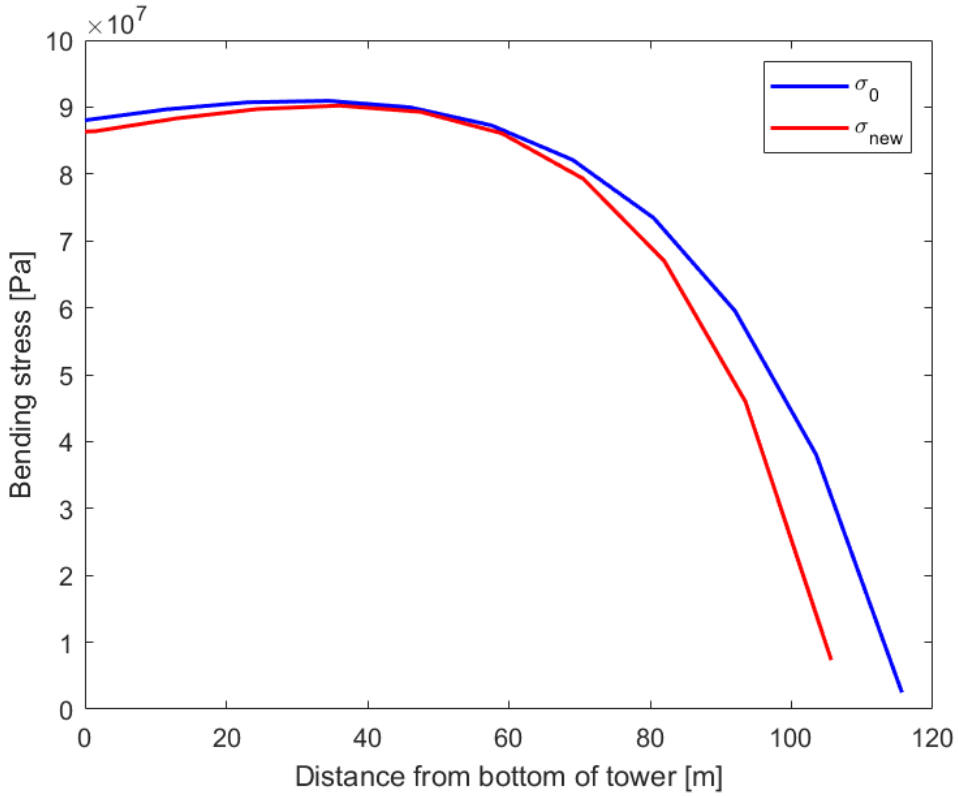

Figure 8: Bending stress of original (σ_0) and modified (σ_{new}) tower

Height [m]	Outer diameter [m]	Orig. thickness [mm]	New thickness [mm]
0.000	8.300	38	66.5
1.500	8.0215	38	66.5
1.501	8.0215	36	62.8
13.000	7.7431	36	62.8
13.001	7.7431	34	57.7
24.500	7.4646	34	57.7
24.501	7.4646	32	52.5
36.000	7.1861	32	52.5
36.001	7.1861	30	47.6
47.500	6.9076	30	47.6
47.501	6.9076	28	43
59.000	6.6292	28	43
59.001	6.6292	26	38.6
70.500	6.3507	26	38.6
70.501	6.3507	24	34.4
82.000	6.0722	24	34.4
82.001	6.0722	22	30.4
93.500	5.7937	22	30.4
93.501	5.7937	20	26.6
105.630	5.500	20	26.6

Table 5: Diameter and wall thickness of tower, including modifications

3.1.2 Floater

The Hywind OC3 system is used as a basis for identifying the different design solutions.

In order to make a model of the floater in GeniE, a wall thickness and material properties have to be specified. As a simple approach, the wall thickness of the hull is set equal to the thickness at the bottom of the tower. This is justified since this thesis does not include any strength or fatigue analyses. Furthermore, the change in weight distribution caused

by different hull wall thicknesses has a negligible effect on the overall weight distribution of the system. This is later confirmed in a sensitivity analysis of the wall thickness' effect on the center of mass (see tab. 7). The material is assumed to be steel (S355, $\rho_M = 7850kg/m^3$), with a 25% increase to account for secondary structures ($\rho_M = 9812.5kg/m^3$) (*F.G., Nielsen, Personal communication, 11-01-19*). Iron ore is chosen as ballast, due to its high mass density ($\rho_M = 3600kg/m^3$).

The geometry of the floater is described in fig. 9. The diameter above the taper is set equal to the bottom diameter of the tower.

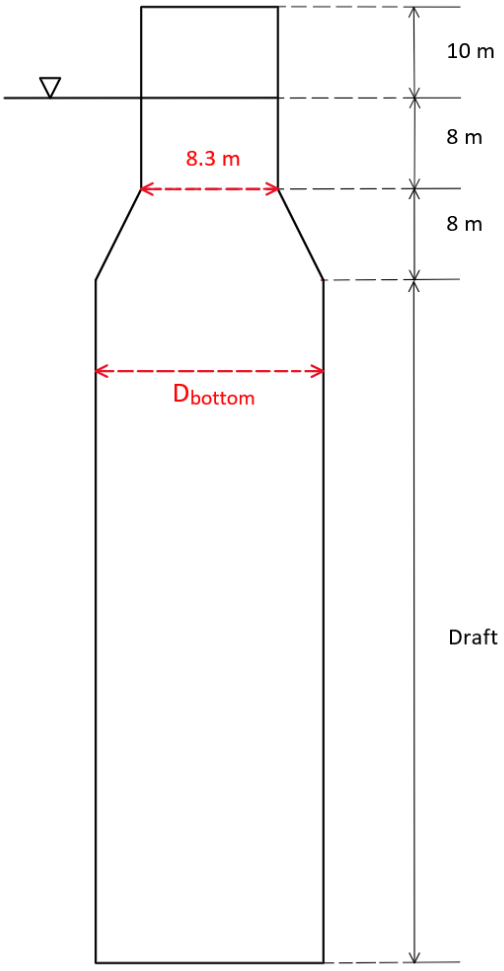

Figure 9: Geometry of floater

3.1.3 Design solutions for different drafts

A total of four different drafts, from 120 m to 60 m, are investigated. As design criteria, the static pitch angle should not exceed 6 degrees when the system is subjected to the maximum thrust force. Eq. 19 in sec. 2.2.4 is used to calculate the static pitch angle. The maximum thrust force was estimated to be between 1505 and 1560 kN in Bak et al. [20], 1555 kN is used in this thesis. The vertical position of the fairlead is set to be at the center of gravity. In order to obtain the correct static pitch angle, the bottom diameter of the floater is increased. The static pitch angle is calculated for different diameters in a loop in MATLAB to find the solution which fits the criteria. The diameter at SWL is held constant to avoid a too low natural period in heave. The solutions are presented in tab. 6. As seen, the increase in mass is mainly ballast.

Draft [m]	D_{bottom} [m]	Hull mass [kg]	Ballast mass [kg]	Total mass of floater [kg]
120	13.7	3.61E06	11.81E06	15.42E06
100	16.1	3.56E06	13.77E06	17.33E06
80	19.8	3.59E06	16.86E06	20.45E06
60	26.7	3.89E06	22.48E06	26.37E06

Table 6: Resulting design solutions for floaters of different drafts

The variation in center of gravity (z_G, measured from SWL) for the system was tested for different wall thicknesses to check its sensitivity (see tab. 7). The wall thicknesses ranged from 50 mm to 100 mm. The largest difference is seen for 120 m draft. Here z_G increased by 1.3 m for each 25 mm increase in wall thickness. The change in z_G would have an effect on the natural periods and dynamic response investigated, however it is considered negligible for the purpose of this thesis.

3.2 Modelling

3.2.1 Panel model

The panel model describes the geometry of the submerged part of the structure, and is used to compute the hydrodynamic pressures on panels. Thus, the panel model only needs

Wall thickness	z_G (from SWL)			
	120 m	100 m	80 m	60 m
25 mm	-82.5 m	-70.1 m	-57.5 m	-44.6 m
50 mm	-81.2 m	-69.2 m	-56.9 m	-44.3 m
75 mm	-80.0 m	-68.3 m	-56.3 m	-44.0 m

Table 7: Variations in center of gravity (z_G) for different wall thicknesses

to include the floater (see fig. 11a). The panel size in the meshing analysis of the panel model is important in order to capture the geometry and hydrodynamic loads accurately. DNVGL-RP-C205 describes the modelling principles related to panel mesh requirements as:

- The diagonal length of panel mesh should be less than 1/6 of smallest wave length analysed.
- The waterplane area and volume of the discretized model should match closely to the real structure.

To make the analyses less time consuming, the panel sizes are set to be 1 m (width and height). This means it is valid for wavelengths larger than $\sim$8.5 m. This is considered acceptable since it applies for wave periods above 3 s. For wave periods below 3 s the hydrodynamic forces are very small. To capture the correct wateplane area and volume of the real structure, the modelled radii of the floaters are increased slightly to compensate, as shown in fig. 10.

3.2.2 Structural model

The structural model is used to describe the mass of the system. The structure is modelled with plates, which are assigned thicknesses and material properties, as described earlier in this chapter. The floater consists of the outer hull and internal ballast tanks. The material density of the floater is 9812.5 kg/m^3. The tower is modelled in ten sections with different diameters and thicknesses as described in [20]. The material density of the tower is 8500 kg/m^3. The diameters and thicknesses of the tower is given in tab. 5. The thickness of

$$
\begin{aligned}
A_{triangle} &= A_{section} \\
r_t^2 cos\left(\frac{\Theta}{2}\right) sin\left(\frac{\Theta}{2}\right) &= \frac{1}{2} r^2 \Theta \\
r_t &= \sqrt{\frac{r^2\Theta}{2cos\left(\frac{\Theta}{2}\right) sin\left(\frac{\Theta}{2}\right)}}
\end{aligned}
$$

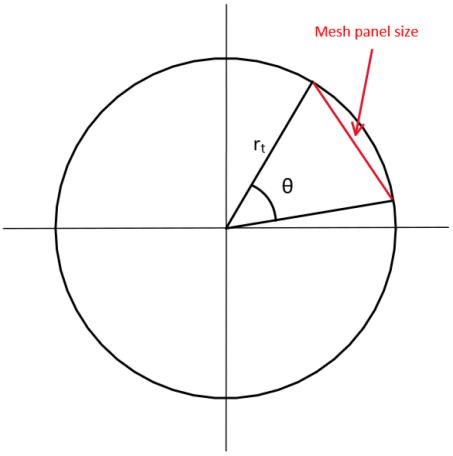

Figure 10: Increasing the modelled radii r_t to capture the correct geometry in the meshing analysis.

the floater is 0.0665 m, which is the same as at the bottom of the tower.

The mass of the rotor, hub and nacelle are modelled as a single point load at their common center of mass (see tab. 8). This center of mass is located outside the tower geometry. To ensure that this load is captured by the meshing analysis, it is modelled at an intersection of beams connected to the tower (see fig. 12). The beams are assigned $\rho_M = 0$, so they are not included in the overall mass of the structure. For simplification, the offset in CM for the rotor in x-direction is omitted in the dynamic response analyses.

Component	Mass [kg]	x [m]	y [m]	z [m]
Nacelle	446,036	2.687	0	121.45
Rotor (hub + blades)	230.667	-7.07	0	119
Total	676,703	-0.64	0	120.6

Table 8: Mass and center of mass of rotor and nacelle. Reference frame origin at base and geometric center of tower. z is positive upwards. x is positive in the direction of the wind.

3.2.3 Hydrostatic and hydrodynamic analyses

In HydroD the origin of the reference frame is defined to be at the center of the cylinder at SWL, and the z-axis is positive upwards.

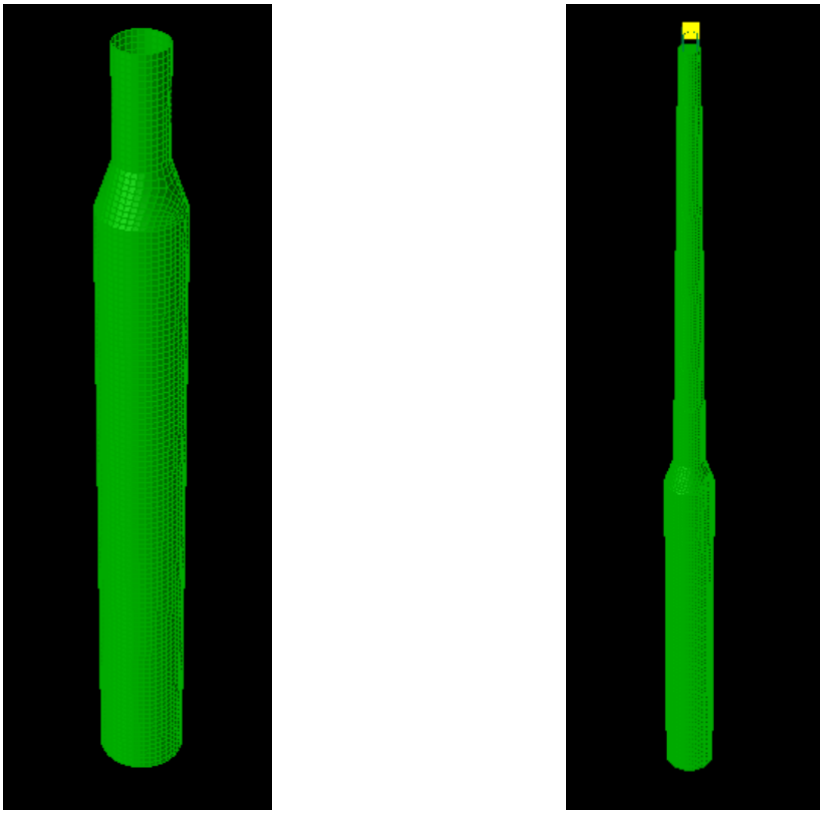

(a) Panel model (b) Structural model

Figure 11: Mesh of panel model and structural model in GeniE

First, the wave directions and frequencies are defined. In the later analyses, only one direction is tested. However, additional directions are cheap in terms of computational effort. Therefore, several directions are defined so that the motion and excitation transfer functions can be checked and compared for different directions, to help verify the results. It is important that the frequency set covers the natural periods (without mooring) of the system. The frequency range is set as 1 to 100 s with 1 s increments. The hydro model is defined as a "deep draft floating installation".

The ballast tanks are filled automatically by HydroD to obtain the specified draft and trim angle (0 deg), with the highest metacentric height possible. The ballast density is 3600 $\frac{kg}{m^3}$. After the structure is properly ballasted, a table with hydrostatic data is generated in HydroD. The displaced volume and waterplane area are checked to make sure the geometry is captured accurately.

The dry mass, added mass, potential damping and hydrostatic restoring matrices, as well

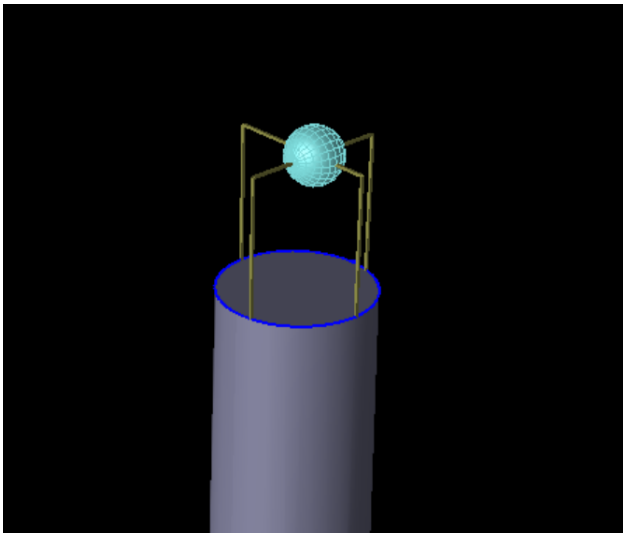

Figure 12: Mass of rotor, hub and nacelle modelled as point load, placed at beam intersection.

as transfer functions for wave excitation forces and moments, are computed in the hydrodynamic analysis. These are later used in the dynamic response analyses. The natural periods in heave and pitch are checked to ensure that they are above the acceptable limit (> 25 s). The matrices used in the dynamic response analyses are given in tab. 19 - 23 in appendix A.

3.3 Environmental loads

The power curve and thrust curve for the DTU 10 MW wind turbine is shown in fig.13a and fig. 13b. As specified in tab. 2, sec. 1.3.4, it has a cut-in wind speed of 4 m/s, rated wind speed of 11.4 m/s and cut-out wind speed of 25 m/s.

Mean wind speeds (u_M) at hub height (119 m) below rated, near rated and above rated, and corresponding turbulence intensities, are selected based on the work of Nybø et al. [26]. The wind speeds are obtained from the FINO-1 platform in the North Sea. They are measured at 80 m and scaled to 119 m (hub height) using the logarithmic law. The turbulence intensities (TI) are found from standard deviations calculated at 80 m.

Probable combinations of significant wave heights (H_S) and peak periods (T_P) are identified for each of the chosen wind speeds, based on statistical data from the North Sea.

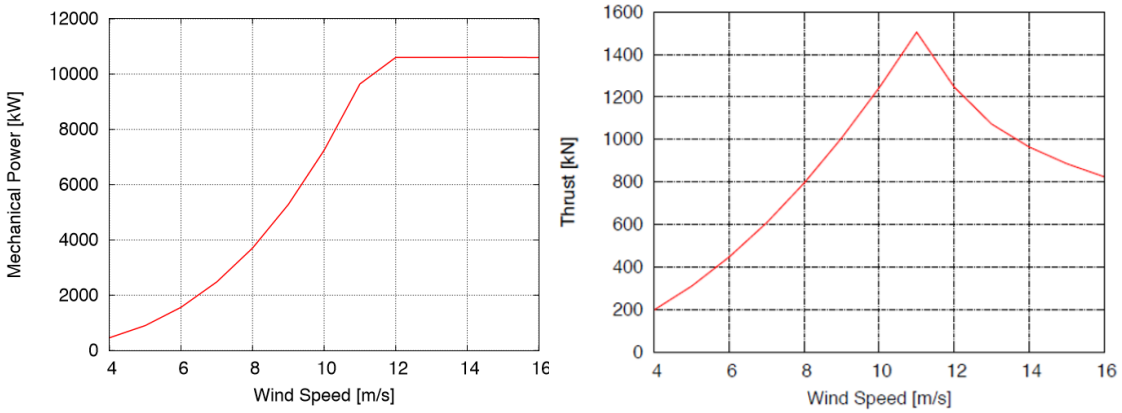

(a) Power curve

(b) Thrust curve

Figure 13: Power and thrust curve for the DTU 10 MW RWT based on BEM theory. From [20]

The load cases are given in tab. 9.

Load case no.	u_M [$\frac{m}{s}$]	TI [%]	H_S [m]	T_P [s]
1 (below rated)	7.6	5.2	1.8	10
2 (near rated)	12.4	5.9	3.2	8.8
3 (above rated)	17.6	6.3	5.1	10.6

Table 9: Load cases

3.4 Calculating the dynamic response

The frame of reference is defined so that z = 0 at SWL. The z-axis is positive upwards and the x-axis is positive in the direction of the wind and waves.

3.4.1 Mooring system

The mooring system is modelled as an additional restoring matrix with the following terms:

$$C_{M,11} = k_x \qquad [N/m] \tag{26a}$$

$$C_{M,15} = C_{M,51} = z_m \cdot k_x \qquad [N] \tag{26b}$$

$$C_{M,55} = z_m^2 \cdot k_x \qquad [Nm] \tag{26c}$$

Where k_x is the horizontal component of the resulting restoring stiffness from all the mooring lines and z_M is the vertical position of the fairleads. Since the horizontal component of the mooring stiffness is dominant in surge and pitch, the vertical component is neglected. In the vertical direction (heave), the hydrostatic stiffness is dominant. The restoring matrix elements are given in tab. 22 and 23 in appendix A.

The natural period in surge and pitch are investigated for different k_x. The mooring line stiffness is then set to a value where the natural period in surge is above 100 s for all modelled drafts.

3.4.2 Forces

As mentioned in sec. 2.4.2, Wadam calculates the transfer functions of the exciting forces and moments (for each DOF) in the frequency domain. These are normalised by the wave amplitude, thus the wave excitation spectra can by found from these transfer functions and the wave spectrum [25].

The amplitude and frequency for the wave exciting forces/moment ($H_a(f)$) in surge, heave and pitch are collected from Wadam. A JONSWAP spectrum ($S_J(f)$) is generated for the specified H_S and T_P for the three specified load cases (see tab. 9). Then the wave excitation spectra ($S_R(f)$) in surge, heave and pitch for each load case is calculated using eq. 27.

$$S_R(f) = S_J(f)H_a(f)^2 \tag{27}$$

The spectra is then converted to time domain using inverse fast Fourier transform. The result is time series ($F_{a,j}(t)$) of the wave loads in surge (1), heave (3) and pitch (5) for each load case.

Hydrostatic and hydrodynamic data found in the previous analyses are used to calculate the natural periods and dynamic response. The added mass and damping matrices (which are frequency dependant) are chosen for the natural period of pitch, and assumed constant.

The added mass and damping for different DOF and drafts are enclosed in appendix A. It can be seen that for the range of periods of interest (25 s - 150 s) they show very little variation.

The response parameters are defined as follows:

- η_1 = surge [m]
- η_3 = heave [m]
- η_5 = pitch [rad]
- $\dot{\eta_1}$ = surge velocity [m/s]
- $\dot{\eta_3}$ = heave velocity [m/s]
- $\dot{\eta_5}$ = pitch velocity [rad/s]

The wind in the horizontal direction at hub height is modelled by first making time series of the wind and then calculate the thrust force. The turbulence is modelled using the Kaimal spectrum, with the mean wind speeds and turbulence intensities specified in the load cases. A time history of the wind turbulence spectrum is found using inverse fast Fourier transform. The mean wind speed is then added to make time series of the wind (u_{nac}). As mentioned in sec. 2.1.4 this method neglects the spatial variability in wind speed over the rotor.

The relative velocity is calculated using eq. 21. A notch filter is used to simulate a controller in a simplistic manner. It filters the relative wind speed at rated and above rated, to avoid forces with frequencies equal to the natural frequency in pitch. This is done to avoid resonant motion response in pitch and surge. By using a filter, some parts of the forces are removed. Thus, the width of the filter should be as narrow as possible, while still hindering the resonant build up.

The drag force with a drag coefficient of 0.6 is included to account for viscous effects. This will contribute to some excitation and damping in surge and pitch. A small linear damping (ζ_{jj}) of 1 % is added in all modes (surge, heave and pitch) to account for hydrodynamic damping, and prevent a build up of resonant response. Both the drag coefficient and added linear damping is chosen in accordance with Jonkman [19].

The wind and drag forces in surge (1) and pitch (5) are calculated using eq. 28a - 28i, there is no contribution in heave from wind and drag. The thrust coefficient used to calculate the wind force is shown in fig. 13b. All the forces (wave, wind and drag) are then added together for each direction (F_1 = surge, F_3 = heave and F_5 = pitch).

$$F_{1,wind}(t) = \frac{1}{2} C_T(u) \rho_a \pi R_T^2 u_{rel,nac}^2(t) \tag{28a}$$

$$F_{3,wind}(t) = 0 \tag{28b}$$

$$F_{5,wind}(t) = F_{1,wind}(t) z_a \tag{28c}$$

$$F_{1,wave}(t) = F_{a,1}(t) \tag{28d}$$

$$F_{3,wave}(t) = F_{a,3}(t) \tag{28e}$$

$$F_{5,wave}(t) = F_{a,5}(t) \tag{28f}$$

$$F_{1,drag}(t) = \sum_{z=0}^{draft} \left(\frac{1}{2} C_D \rho_W D_{bottom} u_{rel}(z,t) \mid u_{rel}(z,t) \mid dz \right) \tag{28g}$$

$$F_{3,drag}(t) = 0 \tag{28h}$$

$$F_{5,drag}(t) = \sum_{z=0}^{draft} \left(\frac{1}{2} C_D \rho_W D_{bottom} u_{rel}(z,t) \mid u_{rel}(z,t) \mid dz z_a \right) \tag{28i}$$

3.4.3 Dynamic response

Time series of the dynamic response in surge, heave and pitch are calculated using forward Euler integration, where the next step is calculated as:

$$\boldsymbol{\eta_R}(t + dt) = \boldsymbol{\eta_R}(t) + dt(\boldsymbol{A}\boldsymbol{\eta_R}(t) + \boldsymbol{bF}(t)) \tag{29}$$

$$\boldsymbol{\eta_R} = \begin{bmatrix} \eta_1 \\ \eta_3 \\ \eta_5 \\ \dot{\eta_1} \\ \dot{\eta_3} \\ \dot{\eta_5} \end{bmatrix} \quad \mathbf{A} = \begin{bmatrix} \mathbf{0} & \mathbf{I} \\ -\mathbf{M}^{-1}\mathbf{C} & -\mathbf{M}^{-1}\mathbf{B} \end{bmatrix} \quad \mathbf{b} = \begin{bmatrix} \mathbf{0} \\ \mathbf{M}^{-1} \end{bmatrix} \qquad \mathbf{F} = \begin{bmatrix} F_1 \\ F_3 \\ F_5 \end{bmatrix}$$

Where **M** is the total mass matrix (dry and added mass), **B** is the damping matrix and **C** is the restoring matrix.

The simulation length is 3600 s. The analyses are run ten times with different seed numbers. The mean values of the responses are set as starting values, to minimize the start-up transient effects.

4 Results

Four spar floaters with drafts ranging from 60 - 120 m have been modelled, with enough buoyancy to support the DTU 10 MW RWT (sec. 3.1). The initial criteria was a maximum static pitch angle of 6 degrees when subjected to maximum thrust force. This was achieved by increasing the bottom diameter of the floater. The wall thickness of the tower has been increased in order to withstand the additional bending stress from heeling. Hydrostatic and hydrodynamic analyses were performed in HydroD (sec. 3.2.3) Three load cases were defined (sec. 3.3) and used to determine the wind, wave and drag forces acting on the structures, which in turn were used to calculate the dynamic response (sec. 3.4).

This chapter will present the results of the hydrodynamic and dynamic response analyses. They will be discussed further in sec. 5. The results include:

- Hydrostatic properties: center of gravity, center of buoyancy, displaced volume and waterplane area.
- Natural periods without mooring lines.
- Natural periods for different mooring line stiffness'. These results are used to determine the stiffness used in the dynamic response analyses.
- Test of bandwidth and time steps in the dynamic analyses. These results are used to determine the bandwith and time step in the dynamic response analyses.
- Sensitivity analyses of the natural periods and repsonse in surge and pitch for different fairlead locations.
- Resulting wind, wave and drag forces in surge, heave and pitch for 120 m draft for the three load cases.
- Dynamic response in surge, heave and pitch for all drafts and load cases.

4.1 Hydrostatic data

The vertical center of buoyancy (z_B) and center of gravity (z_G) calculated in HydroD are shown in tab. 10.

Draft	z_B	z_G
120	-63.7	-81.4
100	-54.4	-63.9
80	-45	-56.9
60	-35.6	-44.2

Table 10: Vertical center of buoyancy (z_B) and center of gravity (z_G) for different drafts

The displaced volume and waterplane area calculated in HydroD, and their real, values are presented in tab. 11. The values match very well, which shows that the accuracy of the models are acceptable.

Draft [m]	$A_{WP}[m^2]$ (HydroD)	Real $A_{WP}[m^2]$	$V[m^3]$ (HydroD)	Real $V[m^3]]$
120	54.2	54.1	16531	16544
100	54.2	54.1	18413	18401
80	53.9	54.1	21454	21451
60	54.0	54.1	27201	27222

Table 11: Displaced volume (V) and waterplane area A_{WP} from HydroD, and their real values, for different drafts

4.2 Natural periods

The natural periods in pitch and heave, without mooring, are listed in tab. 12. Since the frame of reference in HydroD is defined so that z=0 at SWL, the surge-pitch coupling terms must be included when calculating the natural period in pitch (sec. 2.2.2).

Natural periods in surge and pitch for different mooring line stiffness' (k_x) are presented in fig. 14 and 15. The fairleads are placed midway between the center of buoyancy and center of gravity, which is approximately at the center of rotation. It can be seen that the natural period in surge approaches infinity as k_x approaches zero. This is because there is no hydrostatic stiffness associated with surge. A k_x of 1e5 N/m was chosen for the further analyses, as this keeps the natural period in surge between 100 and 150 s for all drafts.

Draft [m]	$T_{e,3}$ [s]	$T_{e,5}$ [s]
120	35.9	32.2
100	38.5	29.6
80	40.7	27.2
60	51.3	24.5

Table 12: Natural periods in heave and pitch, without mooring

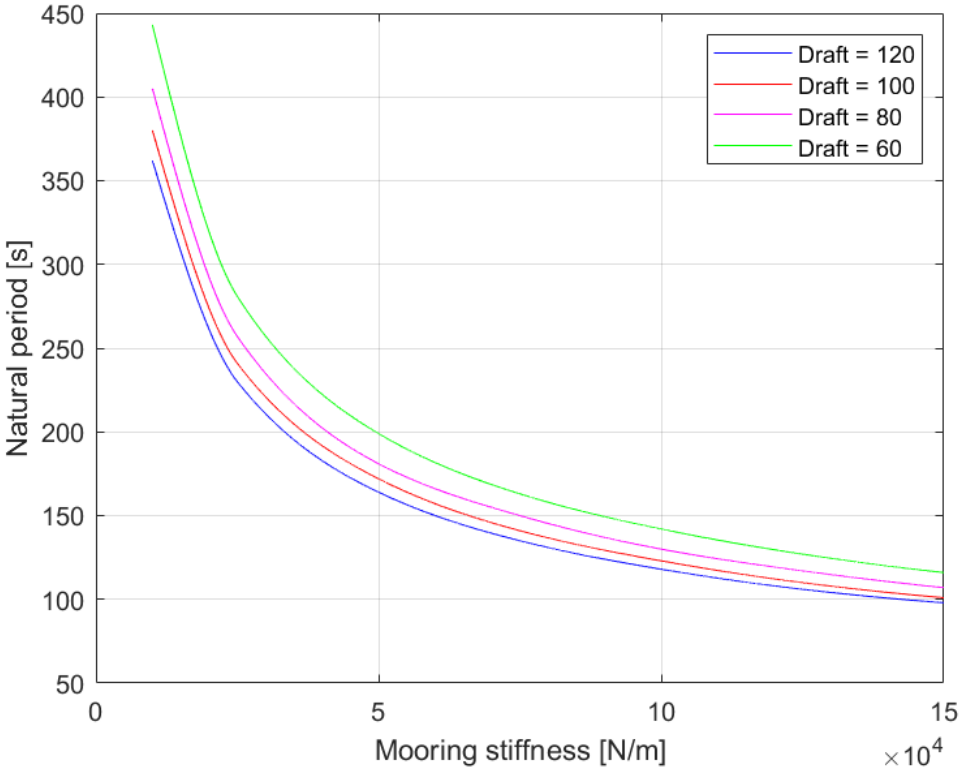

Figure 14: Natural period in surge for different mooring line stiffness

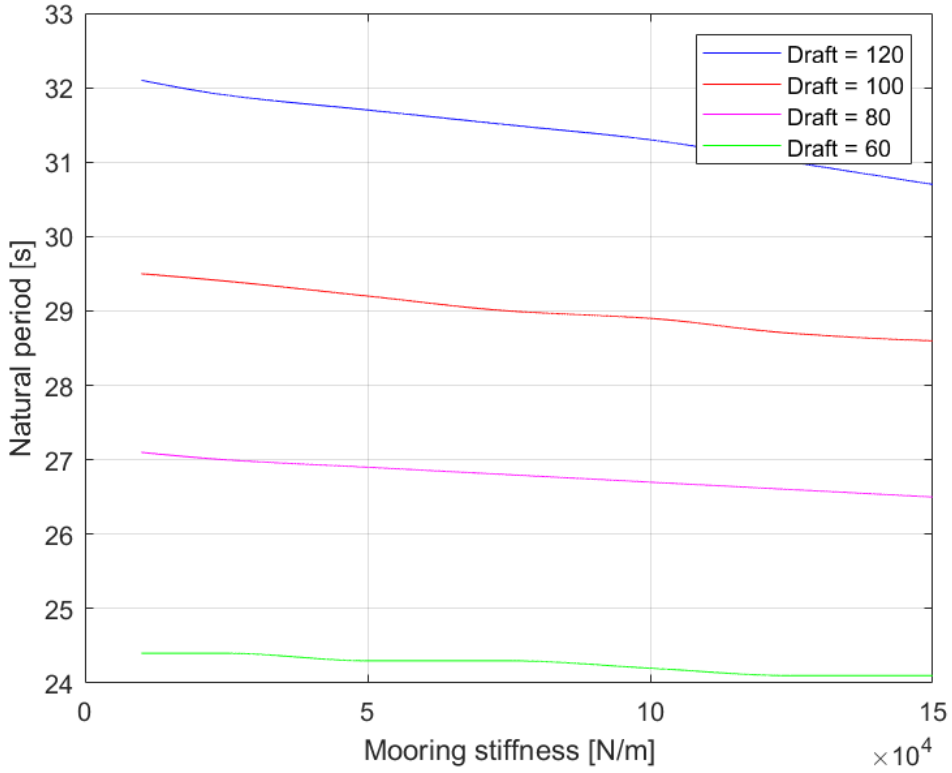

Figure 15: Natural period in pitch for different mooring line stiffness

4.3 Dynamic response analyses

The load cases (LC) used in the dynamic response analyses are defined in sec. 3.3. LC1 is below rated, LC2 is near rated and LC3 is above rated.

4.3.1 Bandwidth and time step

The bandwidth and time step were investigated to determine their values in the further analyses. Here k_x = 1e5 N/m and the vertical position of the fairlead are approximately at the center of rotation. All cases were run for draft = 120 m with load case 2 (near rated wind speed).

Fig. 17 and 18 show time series of pitch and surge with different filter bandwidths (ϵ = 0, 0.1 and 0.2) for different time steps (Δt = 0.1, 0.01 and 0.005 s). As mentioned in sec. 3.4.2, the filter should be as narrow as possible, while still remove resonant motion response.

When comparing fig. 17a - 17c it can be seen that without filter, there is a large build up of resonant motion corresponding to the pitch natural frequency ($\sim$32 s), and the surge motion is dominated by the pitch motion. The resonant motion is limited both by increasing the bandwidth and decreasing the time step. Since the resonant motion build up is still substantial for $\epsilon = 0.1$, a bandwidth of 0.2 was chosen for the further analyses.

Fig. 16 show the time series of pitch for $\epsilon = 0.2$ with different time steps. Ideally, the time step should be small enough that the time series converges to the same value. However, a smaller time step drastically increases the computational time. And so, due to limited time available, a time step of 0.1 was chosen for the further analyses. The mean and standard deviation is 4.77 degrees and 0.98 degrees for Δt = 0.01 s, and 4.78 and 0.95 for Δt = 0.005 s. Their similarities indicate that this simplification will not significantly impact the results. In later studies it is recommended to use a more accurate integration methods, e.g. 4th order Runge Kutta.

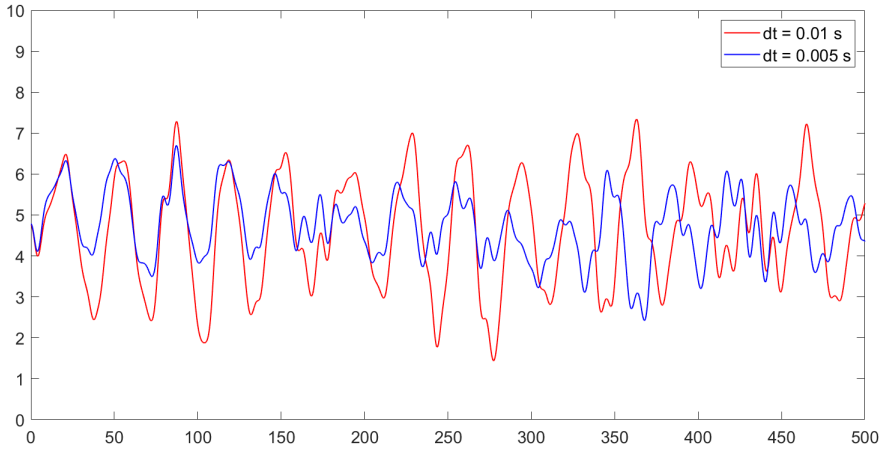

Figure 16: Pitch with different time steps, for e = 0.2

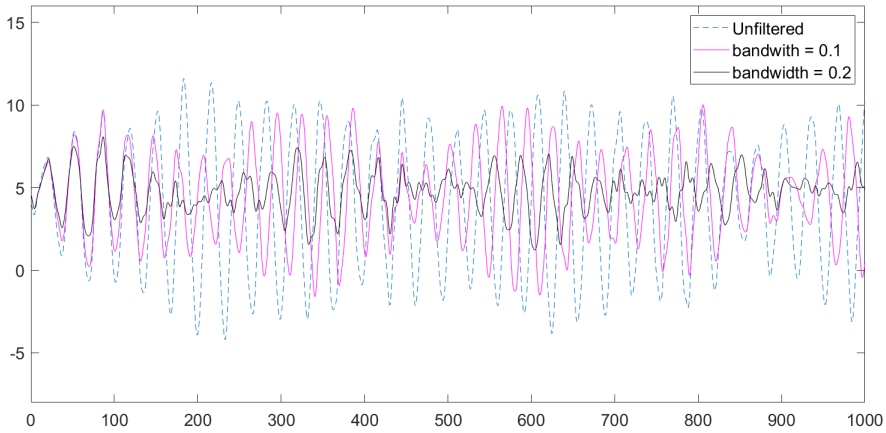

(a) Pitch, $\Delta t = 0.1$

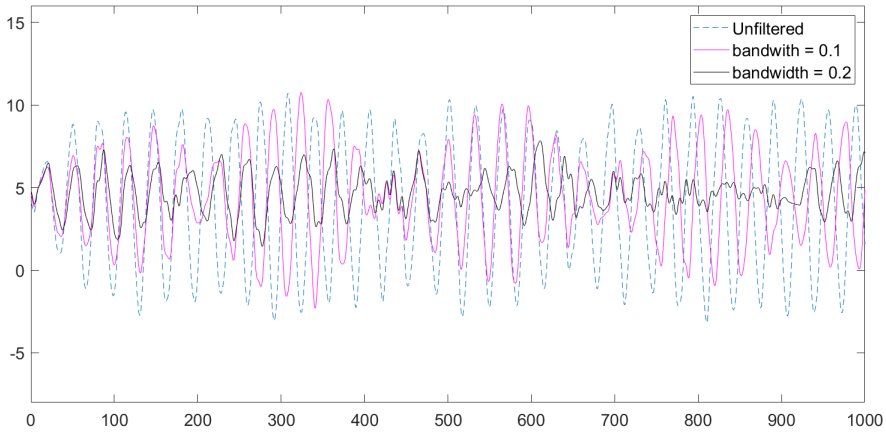

(b) Pitch, $\Delta t = 0.01$

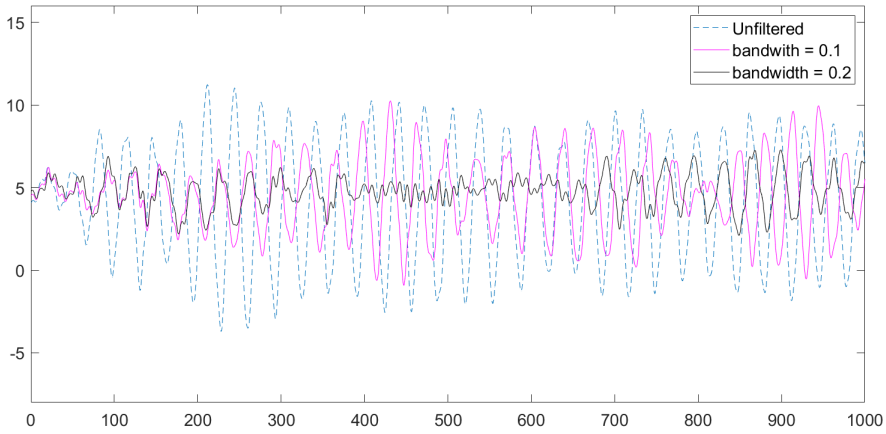

(c) Pitch, $\Delta t = 0.005$

Figure 17: Time series of pitch with different filter width and time steps.

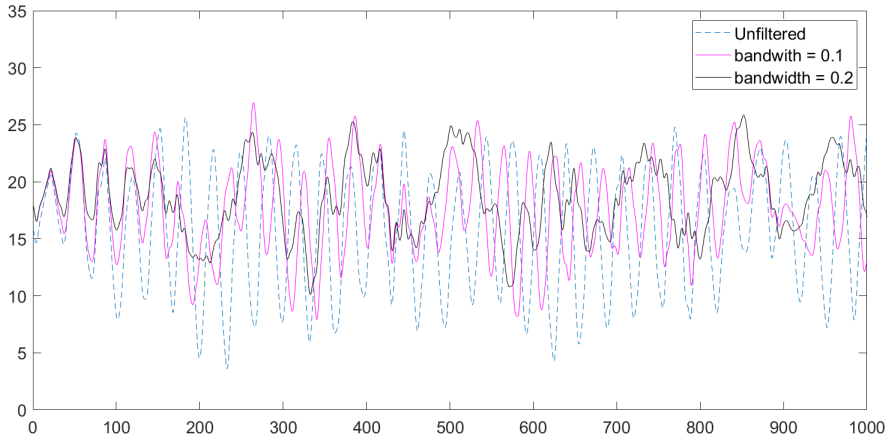

(a) Surge, $\Delta t = 0.1$

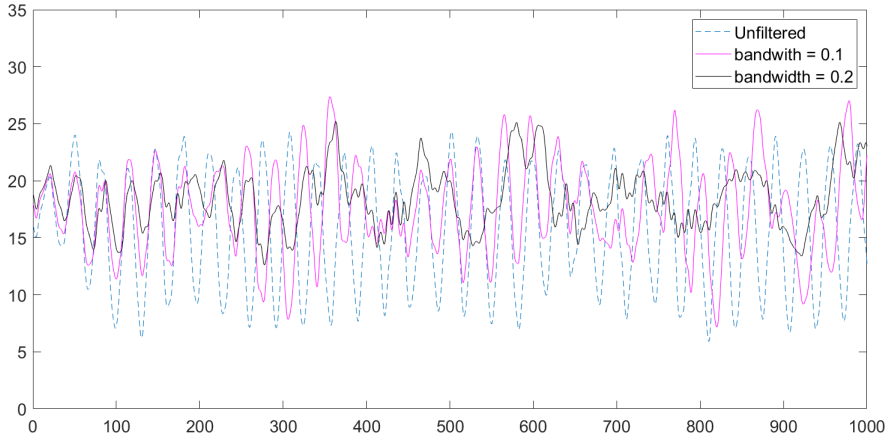

(b) Surge, $\Delta t = 0.01$

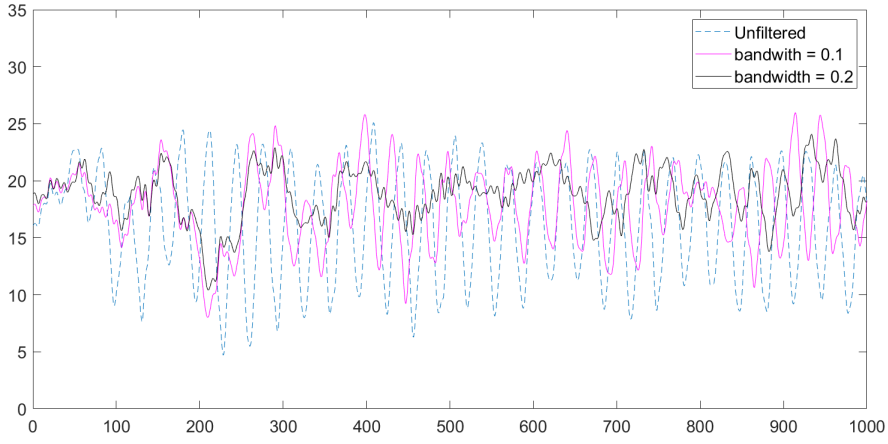

(c) Surge, $\Delta t = 0.005$

Figure 18: Time series of surge with different filter width and time steps.

4.3.2 Significance of fairlead location

Tab. 13 and 14 show the natural periods and responses in surge and pitch for different vertical positions of the fairlead (z_m), for 120 m and 60 m draft. The middle values in the z_m column are the vertical center of rotation (z_R).

As described in sec. 2.2.1, the surge-pitch restoring is uncoupled when the fairleads are placed at the center of rotation (eq. 6). This placement gives the highest natural frequency in pitch. This is especially advantageous for the 60 m draft where the natural period is near the undesired range.

For the further analyses the fairleads were placed at the center of rotation. This was done to avoid coupling between surge and pitch, and to keep the natural period in pitch as high as possible.

z_m [m] (from SWL)	$T_{e,1}$ [s]	$T_{e,5}$ [s]	Surge, mean [m]	Pitch, mean [deg]
0	125	29.5	11.7	2.7
-36.1	117	31.4	13.75	3.5
-72.2	114	32.2	17	4.3
-96.1	116	31.8	19.5	4.8
-120	119	30.9	22.55	5.3

Table 13: Variations in natural periods and response for different vertical positions of the fairlead. Draft = 120 m, center of rotation: -72.2 m

z_m [m] (from SWL)	$T_{e,1}$ [s]	$T_{e,5}$ [s]	Surge, mean [m]	Pitch, mean [deg]
0	145	23.7	11.7	3.4
-20	141	24.2	13.1	3.9
-40	140	24.5	14.9	4.5
-50	140	24.4	16	4.8
-60	141	24.3	17.1	5.1

Table 14: Variations in natural periods and response for different vertical positions of the fairlead. Draft = 60 m, center of rotation: -40 m

4.3.3 Forces

Fig. 19, 21 and 20 show time series of the wind, wave and drag forces in surge for all load cases, for 120 m draft (one seed number). Fig. 22 show time series of the wave forces in heave for all load cases, for 120 m draft (one seed number). Their mean, standard deviation, maximum and minimum values are given in tab. 15.

The maximum occurring wind force is found to be $\sim$1500 kN. The wind force is lowest for LC1 and highest for LC2, which corresponds to the thrust curve (fig. 13b, sec. 3.3). The wave and drag forces are nearly symmetrical about the mean, which is zero. The amplitude and standard deviation increase for higher waves. The amplitudes of the drag forces are very small compared to wave forces.

Relative wind speed				
	Mean [m/s]	St.dev [m/s]	Maximum [m/s]	Minimum [m/s]
LC1	7.3	0.48	9.2	5.6
LC2	11.9	0.91	15.8	9.2
LC3	16.9	1.54	24.3	10.9
Surge - 120 m draft				
Wind	Mean [kN]	St.dev [kN]	Maximum [kN]	Minimum [kN]
LC1	691	74.6	1015	410
LC2	1281	145	1506	842
LC3	793	81	1504	592
Waves	Mean [kN]	St.dev [kN]	Maximum [kN]	Minimum [kN]
LC1	0	929	3398	-3610
LC2	0	1541	5554	-6138
LC3	0	2694	8725	-8789
Drag	Mean [kN]	St.dev [kN]	Maximum [kN]	Minimum [kN]
LC1	-0.02	7	44	-66
LC2	-0.37	35	180	-206
LC3	-0.12	59	334	-470
Heave - 120 m draft				
Waves	Mean [kN]	St.dev [kN]	Maximum [kN]	Minimum [kN]
LC1	0	226	794	-737
LC2	0	348	1084	-1173
LC3	0	674	2287	-2644

Table 15: Forces - mean, standard deviation, maximum and minimum, for 120 m draft in time simulation

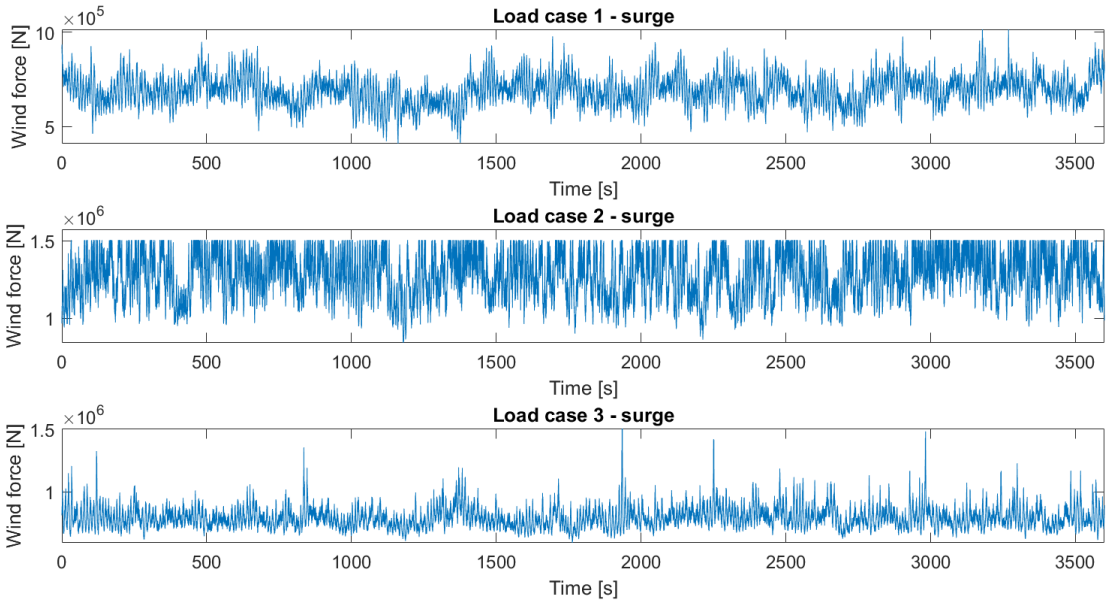

Figure 19: Wind forces in surge for all load cases, draft = 120 m

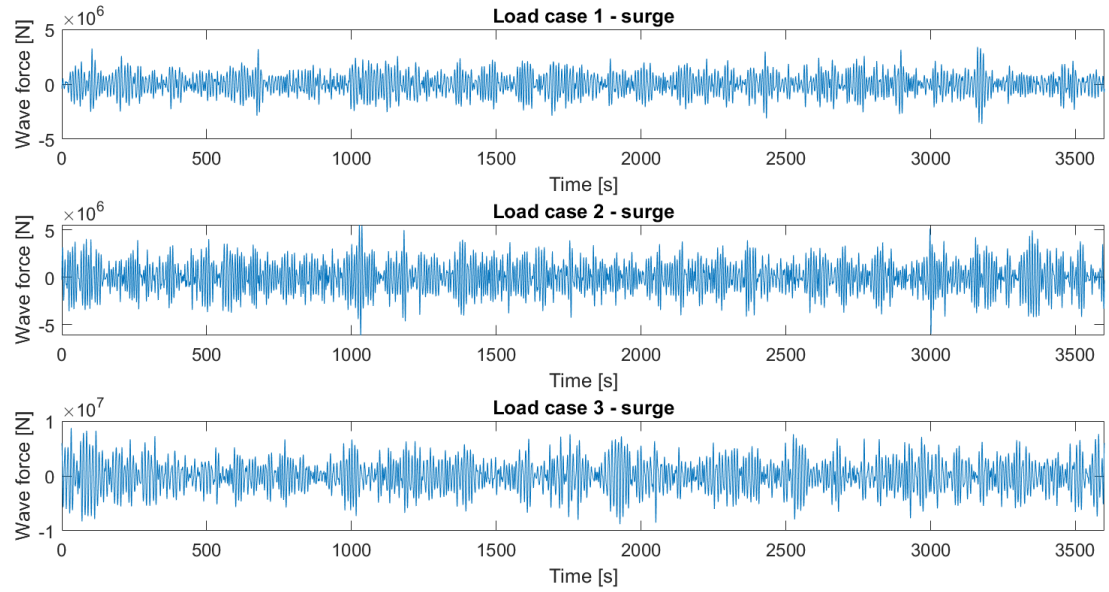

Figure 20: Wave forces in surge for all load cases, draft = 120 m

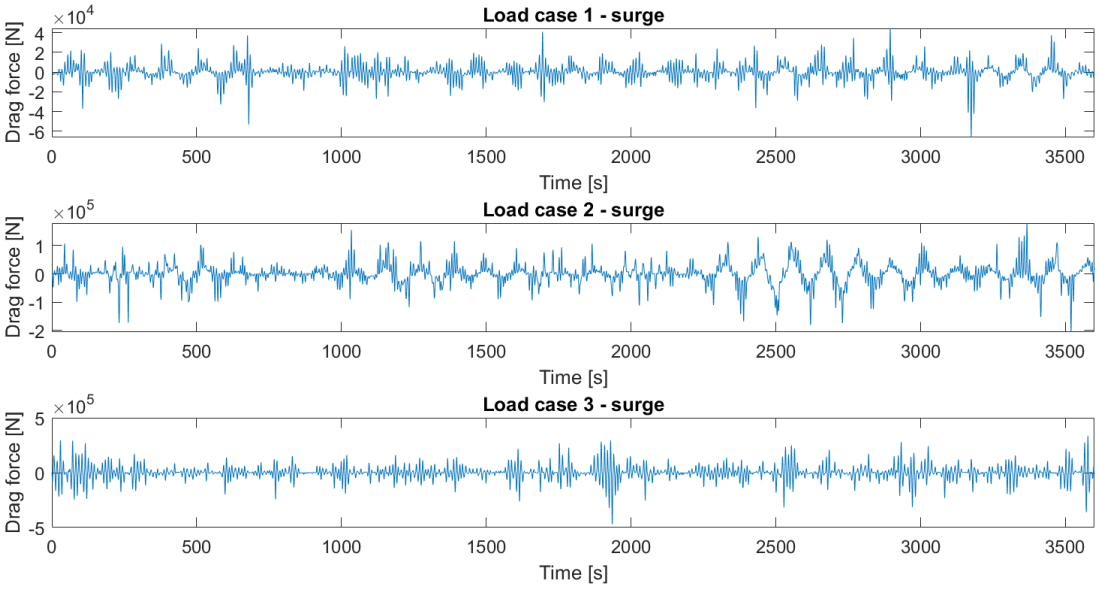

Figure 21: Drag forces in surge for all load cases, draft = 120 m

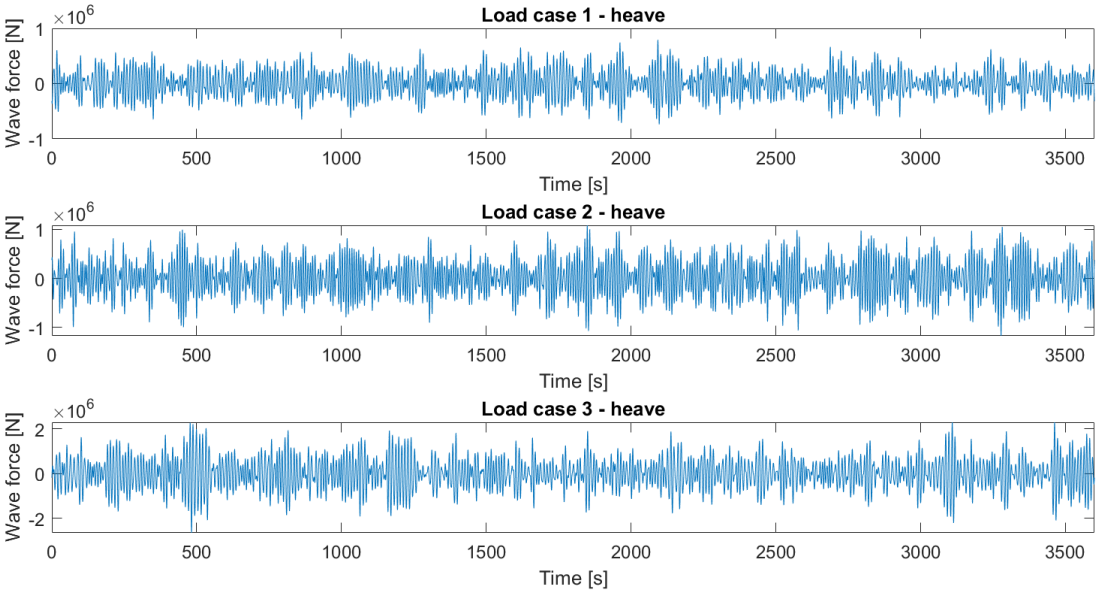

Figure 22: Wave forces in heave for all load cases, draft = 120 m

4.3.4 Dynamic response

The results of the dynamic response analyses are given in fig. 16 (surge), 17 (heave) and 18 (pitch). They are given as mean, standard deviation, maximum and minimum. The results are mean and standard deviations (in parenthesis) of ten time series with different seed numbers.

Surge				
Load case no. 1				
Draft [m]	Mean [m]	Standard deviation [m]	Maximum [m]	Minimum [m]
120	10.16 (0.01)	1.15 (0.04)	13.65 (0.43)	6.15 (0.61)
100	9.70 (0.01)	1.17 (0.02)	13.41 (0.58)	6.1 (0.33)
80	9.26 (0.01)	1.18 (0.04)	12.76 (0.34)	5.69 (0.41)
60	8.87 (0.01)	1.21 (0.04)	12.82 (0.52)	5.19 (0.55)
Load case no. 2				
Draft [m]	Mean [m]	Standard deviation [m]	Maximum [m]	Minimum [m]
120	18.88 (0.03)	3.46 (0.33)	28.11 (0.83)	8.95 (1.32)
100	17.87 (0.03)	3.30 (0.32)	26.64 (0.79)	8.53 (0.93)
80	16.80 (0.04)	2.77 (0.32)	24.75 (0.73)	8.41 (0.87)
60	15.48 (0.05)	2.51 (0.28)	22.84 (0.92)	7.81 (1.02)
Load case no. 3				
Draft [m]	Mean [m]	Standard deviation [m]	Maximum [m]	Minimum [m]
120	11.67 (0.01)	1.57 (0.09)	16.79 (0.23)	6.90 (0.65)
100	11.18 (0.02)	1.65 (0.11)	16.71 (0.75)	5.90 (0.89)
80	10.80 (0.03)	1.92 (0.14)	17.41 (0.63)	4.53 (0.72)
60	10.51 (0.06)	2.18 (0.18)	18.03 (1.57)	2.41 (2.55)

Table 16: Results of dynamic response in surge, for all load cases. Numbers are mean and standard deviations of ten wave and wind realizations.

Heave				
Load case no. 1				
Draft [m]	Mean [m]	Standard deviation [m]	Maximum [m]	Minimum [m]
120	~ 0 (0)	0.04 (0.01)	0.17 (0.03)	-0.17 (0.04)
100	~ 0 (0)	0.07 (0.01)	0.27 (0.07)	-0.26 (0.08)
80	~ 0 (0)	0.10 (0.02)	0.37 (0.11)	-0.39 (0.13)
60	~ 0 (0)	0.13 (0.04)	0.52 (0.20)	-0.51 (0.20)
Load case no. 2				
Draft [m]	Mean [m]	Standard deviation [m]	Maximum [m]	Minimum [m]
120	~ 0 (0)	0.06 (0.01)	0.26 (0.08)	-0.26 (0.08)
100	~ 0 (0)	0.09 (0.02)	0.34 (0.12)	-0.37 (0.14)
80	~ 0 (0)	0.13 (0.03)	0.51 (0.14)	-0.52 (0.16)
60	~ 0 (0)	0.21 (0.08)	0.86 (0.35)	-0.87 (0.38)
Load case no. 3				
Draft [m]	Mean [m]	Standard deviation [m]	Maximum [m]	Minimum [m]
120	~ 0 (0)	0.15 (0.03)	0.62 (0.19)	-0.61 (0.21)
100	~ 0 (0)	0.23 (0.05)	0.89 (0.23)	-0.95 (0.27)
80	~ 0 (0)	0.34 (0.09)	1.39 (0.49)	-1.40 (0.51)
60	~ 0 (0)	0.49 (0.15)	1.97 (0.78)	-2.00 (0.77)

Table 17: Results of dynamic response in heave, for all load cases. Numbers are mean and standard deviations of ten wave realizations.

Pitch				
Load case no. 1				
Draft [m]	Mean [deg]	Standard deviation [deg]	Maximum [deg]	Minimum [deg]
120	2.58 (0)	0.26 (0.01)	3.48 (0.1)	1.72 (0.09)
100	2.58 (0)	0.30 (0.01)	3.71 (0.13)	1.58 (0.06)
80	2.62 (0)	0.38 (0.01)	4.08 (0.10)	1.35 (0.16)
60	2.68 (0)	0.57 (0.01)	4.81 (0.14)	0.84 (0.15)
Load case no. 2				
Draft [m]	Mean [deg]	Standard deviation [deg]	Maximum [deg]	Minimum [deg]
120	4.79 (0.01)	0.94 (0.06)	7.79 (0.35)	1.42 (0.44)
100	4.76 (0.01)	0.98 (0.06)	7.90 (0.30)	1.60 (0.29)
80	4.75 (0.01)	1.01 (0.08)	7.95 (0.32)	1.26 (0.45)
60	4.68 (0.01)	1.19 (0.05)	8.33 (0.28)	0.37 (0.37)
Load case no. 3				
Draft [m]	Mean [deg]	Standard deviation [deg]	Maximum [deg]	Minimum [deg]
120	2.96 (0)	0.59 (0.02)	5.19 (0.20)	0.89 (0.37)
100	2.98 (0)	0.81 (0.02)	6.22 (0.40)	0.12 (0.56)
80	3.05 (0.01)	1.20 (0.03)	7.48 (0.26)	-1.09 (0.89)
60	3.18 (0.01)	1.98 (0.06)	9.95 (0.87)	-4.25 (0.75)

Table 18: Results of dynamic response in pitch, for all load cases. Numbers are mean and standard deviations of ten wave realizations.

Surge

Since the surge motion is dominated by wind forces, its mean and standard deviation is largest for LC2 and smallest for LC1. It is also increasing with decreasing draft, which is because the motions are referred to SWL, and the surge motion is affected by pitch. The dynamic response measured at center of gravity were also investigated, the results are given in appendix B.

Heave

The heave motion is determined by the wave forces. It is symmetric about the mean, which is zero. Its amplitude and standard deviation is smallest for LC1 and highest for LC3, and it is increasing for decreasing draft.

Pitch The pitch motion is largest for LC2 and smallest for LC1, as it is dominated by wind forces. The pitch values are increasing as the draft is reduced, although the change in mean values are very small.

5 Discussion

5.1 Natural periods

Tab. 12 show that the natural period in pitch is decreasing for decreasing draft. This is due to a smaller vertical distance between the center of buoyancy and center of gravity. For 60 m draft it is just below the recommended limit (> 25s), hence it may not be suitable for some locations. The natural period in heave is well above the recommended limit for all drafts, and increase for decreasing draft. This is because the displaced volume is increasing while the waterplane area is held constant. This means that a higher waterplane area would be tolerated.

Fig. 15 show that the mooring line stiffness has little influence on the pitch natural period. This is as expected, especially as the mooring lines are attached near the center of rotation.

The mooring line stiffness' used in the analyses are the same for all drafts, which means that the systems essentially have the same mooring system. This is done because the aim of this thesis is to find how changes to the draft itself would affect the dynamic response. In reality, the mooring system would have to be adapted for each location. The purpose of a more shallow draft would necessarily be to utilize a more shallow location, hence an identical mooring system is not realistic. The mooring system have a significant impact on the dynamic response of the system, consequently the application of the shallow draft systems depends on whether the necessary mooring line stiffness can be achieved.

5.2 Influence of bandwidth and time step

A notch filter were implemented in the dynamic response analyses to filter out wind velocities with frequencies near the natural period in pitch, for wind speeds at and above rated. This is a simplified methodology to imitate a motion controller, and is done to remove the resonant motion build up in pitch.

The dynamic response analyses were performed using Euler integration, for which the accuracy is highly dependent on the size of the time step. Therefore, different filter bandwidths and time steps were tested to find the best combination for the analyses.

For the pitch motion (fig. 17), it can be seen that without applying a filter a large resonant motion corresponding to the pitch natural period ($\sim$32 s) builds up. This motion is still visible for ϵ = 0.1. In the analyses, ϵ = 0.2 is used. This limits most of the resonant motions in pitch which is what would be expected from a motion controller.

The surge motion (fig. 18) is dominated by the pitch motion. This is because the motions are measured at SWL (z=0), and the center of rotation lies far below this point. When applying the filter and reducing the time step, the resonant motion of pitch dies out. Some periodic motions corresponding to the resonant period in surge ($\sim$ 115 s) is visible, as this frequency is not filtered out.

The time step also has an impact on the resonant response. The accuracy of the Euler method is, as mentioned above, highly dependent on the time step. To increase the accuracy of the integration, a smaller time step would be preferable, but was not possible due to the limited time available. The Euler method may not be suitable for complicated dynamic systems [42]. A better alternative could be to use a higher order Runge-Kutta method.

5.3 Fairlead location

Tab. 13 and 14 show the changes in natural period and response for different vertical positions of the fairleads.

It can be seen that the fairlead position has limited impact on the natural periods, especially for pitch. This is because in pitch, the hydrostatic stiffness is the dominating component of the restoring matrix (as can be seen in tab. 22 and 23 in appendix A). The surge restoring component is not dependent on the fairlead location, hence the change in natural period is due to surge-pitch coupling. When the mooring lines are attached at the center of rotation, there is almost no coupling between surge and pitch. It can be observed that this placement yields the same natural period in pitch as without mooring (tab. 12). This is when the natural period is lowest for surge and highest for pitch.

For pitch, the motion response increase with a lower placement of the fairlead. This is because a larger distance between the fairlead and the rotor increase the moment from

the wind thrust. Since the motion responses are measured at SWL, the pitch motion contributes in surge increasingly as z_m moves further away from z=0. Hence the surge motion increases for a decreasing z_m both because the pitch motion is increasing and because the pitch motions has a higher impact when the fairleads are placed further away from z=0.

The fairleads in the analyses are placed at the center of rotation since this is the location that gives the largest natural period in pitch. This location would also be favourable in regards to minimizing the dynamic loads acting on the mooring lines, but this effect is not investigated in this thesis.

5.4 Forces

Wind, wave and drag forces in surge and wave forces in heave are presented in sec. 4.3.3. The pitch moments are not included, as they have the same characteristics as surge.

The characteristics of the wind forces corresponds well to the thrust curve (fig.13b). The highest forces occur for wind speed near rater. The maximum thrust force is found to be $\sim$1500 kN, which corresponds well to the findings of Bak et al. [20]. For LC1 (below rated) the wind force is harmonic and varies about the mean. For LC2 (near rated) it can be seen that the maximum amplitudes reaches a limit of $\sim$1500 kN, which corresponds to the maximum thrust force. This limit is clearly visible in fig. 19. In LC3, the amplitude is asymmetric about the mean, as it has some peaks that reach the maximum thrust force. These peaks occur when the relative wind speed is near rated.

The wave and drag forces oscillates about y $\approx$ 0, and their amplitudes and standard deviations are increasing with higher load cases. Comparing the forces in surge, the highest amplitudes and standard deviations are found for wave forces. The amplitudes of the drag forces are very small compared to wave forces.

5.5 Dynamic response

The seed number determines how the wave/wind spectra are represented in the time series. Hence, different seed numbers will give different maximum amplitudes. The analyses of

dynamic response were run for ten different seed numbers. The results can be found in tab. 16 - 17. Time series of surge, heave and pitch for one seed number is given in appendix. C.

Surge

The mean value of surge is governed by the wind force, and its amplitude is mostly given by the wave force, with some contributions from drag, turbulence and pitch-coupling. The mean response in surge is highest for LC2 and lowest for LC1, which reflects the wind force. The amplitudes about the mean are increasing with higher load cases, which corresponds to the wave force. The mean value decrease for smaller drafts, which is due to pitch motion interaction when the motion is referred to SWL. That is also why the difference is very small for LC1 and LC3, which are associated with low pitch motions. The motion response in pitch and surge measured at center of gravity is given in appendix B.

Heave

The response in heave is determined by the wave force. Like the wave force, its mean value $\sim$0, and its amplitude increase for higher load cases. The amplitude is also increasing significantly when the draft is reduced. This is because the dynamic pressure on the bottom plate is decreasing with depth. The maximum heave response is found to be $\sim$2 m, and occurs for 60 draft in LC3. This corresponds to $\sim$40% of the significant wave height.

Pitch

As for surge, the mean pitch motion is wind-induced, and the amplitudes are influenced by the wave and drag forces. The mean value of pitch is below 5° for all cases, which is below the design criteria of a maximum static pitch of 6°. It is highest for LC2 and lowest for LC1. The amplitude is increasing for increasing load cases and decreasing draft.

Since the floaters are modelled based on a static pitch criteria, their mean values are very similar within each load case. The small difference in mean values is due to the different amplitudes and how they fit on the thrust curve, which is not linear.

The standard deviation of pitch is increasing significantly for smaller drafts, especially for

LC3. This is due to the wave forces which are largest for smaller drafts and higher load cases.

No extreme environmental conditions were tested in this thesis. At extreme wind speeds (above 25 m/s) the turbine would shut down and the thrust forces would be minimal. Thus an extreme condition is not expected to further increase the response in surge. However, higher waves would have a significant impact on the response in heave and some significance on the maximum response in pitch.

The highest mean and maximum value of surge were found to be $\sim$19 m and $\sim$28 m, respectively. For pitch the highest mean value was $\sim 5^{\circ}$ and highest maximum value was $\sim 11^{\circ}$. The maximum value of surge was $\sim$40% of the significant wave height. It is difficult to conclude whether the motion responses are within acceptable limits, as this depends on several factors. The acceptable motion response in surge is mainly dependent on the tolerance of the electric cables, while for pitch motion the tolerance of the wind turbine components are the main concern. The pitch motion could also impact the power output of the turbine. Nevertheless, the results are found to be within the same range as found in other studies [43, 44, 45, 46].

6 Conclusion and further work

6.1 Conclusion

Design solutions for four spar buoys with drafts ranging from 60 to 120 m supporting the DTU 10 MW RWT were identified and modelled. Analyses of natural periods and dynamic response in surge, heave and pitch were successfully carried out for all models for different environmental loads. The main findings are listed below:

- The natural period in pitch is decreasing with decreasing draft. For a draft of 60 m the natural period was just below the recommended limit of 25 s.
- The natural period in heave was well within acceptable limits for all drafts.
- The mean value of surge and pitch motion responses are governed by the wind force, and the amplitudes mainly reflects the wave force.
- The response in surge decrease with decreasing draft. The highest mean (19 m) and maximum (28 m) response was found for load case 2, which corresponds to a wind speed near rated.
- The pitch amplitudes are increasing with decreasing draft. The highest mean response (4.7 deg) was found for load case 2, and the highest maximum response (10 deg) was found for load case 3, both for 60 m draft.
- The response in heave is governed by the wave force. It is increasing with decreasing draft. For 60 m draft the surge response is $\sim$40% of the significant wave height.
- The dynamic responses are comparable to findings in previous studies.

It can be concluded that it is theoretically possible for a spar buoy, with a draft as low as 60 m, to support a 10 MW wind turbine, while still maintaining a dynamic response within acceptable limits.

However, the sites available for utilization of this structure depends on the mooring system which is very simplified in this analyses. When the draft is reduced the volume must be increased in order to achieve the necessary stability. This means an increase in material

which would drive up the costs. These aspects would have to be taken into account when assessing the utilization of the shallow draft spar platform system.

6.2 Recommendations for further work

Some aspects have not been covered in this thesis, and several assumptions were made. Therefore, it is recommended that the following work is conducted:

- Strength and fatigue analyses in order to determine the wall thickness and mass of the floater and tower more accurately.
- An in depth mooring analysis for a specified location, appropriate for each draft.
- Investigation of the dynamic response (especially for pitch and heave) in extreme conditions.
- Investigation of the yaw-motion.

References

[1] IEA. Next generation wind and solar power. *OECD/IEA*, 2016.

[2] Directive (eu) 2018/2001 of the european parliament and of the council of 11 december 2018 on the promotion of the use of energy from renewable sources (text with eea relevance.). *OJ*, L 328/82:82–209, 2018-12-21.

[3] European Commission. Communication from the comission to the european parliment, the european council, the council, the european economic and social committee and the committee of the regions. *The European Green Deal*, 2019-11-12.

[4] Wind Europe. Offshore wind in europe - key trends and statistics 2019. Feb 2020.

[5] Eurostat. Share of energy from renewable sources, March 2020. URL `https://appsso.eurostat.ec.europa.eu/nui/show.do?dataset=nrg_ind_ren&lang=en`. Accessed: 2020-04-21.

[6] Wind Europe. Floating offshore wind vision statement. June 2017.

[7] Equinor ASA. Hywind scotland, . URL `https://www.equinor.com/no/what-we-do/floating-wind/hywind-scotland.html`. Accessed: 2020-04-19.

[8] EDP. Windfloat atlantic starts supplying clean energy in portugal, Jan 2020. URL `https://www.edp.com/en/news/2020/01/02/windfloat-atlantic-starts-supplying-clean-energy-portugal`. Accessed: 2020-04-23.

[9] Wind Europe. Floating offshorw wind energy: a policy blueprint for europe. Oct 2018.

[10] Equinor ASA. Hywind tampen, . URL `https://www.equinor.com/no/what-we-do/hywind-tampen.html`. Accessed: 2020-04-23.

[11] Subhamoy Bhattacharya. *Design of Foundations for Offshore Wind Turbines*. John Wiley & Sons, Ltd, Hoboken, USA, 1 edition, 2019. ISBN 9781119128144.

[12] Feargal P. Brennan, Jeffrey Falzarano, Zhen Gao, Einar Landet, Marc Le Boulluec, Chae Whan Rim, Jaideep Sirkar, Liping Sun, Hideyuki Suzuki, Arnaud Thiry, Florent Trarieux, and Chien Ming Wang. Offshore renewable energy. *18th International Ship and Offshore Structures Congress*, 2:169 – 172, Sept 2012.

[13] Blue H Engineering. Historical development. URL `https://www.bluehengineering.com/tablet/historical-development.html`. Accessed: 2020-04-21.

[14] James G. Speight. *Handbook of Offshore Oil and Gas Operations*. Elsevier Science & Technology, USA, 1 edition, 2015. ISBN 9780080878195.

[15] Ideol. Floatgen demonstrator. URL `https://www.ideol-offshore.com/en/floatgen-demonstrator`. Accessed: 2020-04-21.

[16] Illustration of hywind tampen, Aug 2018. URL `https://commons.wikimedia.org/wiki/File:Hywind_Tampen.jpg`. Accessed: 2020-04-19. Licensed under Creative Commons Attribution-Share Alike 4.0 International.

[17] Principle power - windfloat, Feb 2011. URL `https://commons.wikimedia.org/wiki/File:Diagram_of_Principle_Power%27s_WindFloat.jpg`. Accessed: 2020-04-19. Licensed under Creative Commons Attribution-ShareAlike 3.0 Unported.

[18] Ideol - floatgen, Sept 2018. URL `https://commons.wikimedia.org/wiki/File:Floatgen.jpg`. Accessed: 2020-04-20. Licensed under Creative Commons Attribution-Share Alike 4.0 International.

[19] J Jonkman. Definition of the floating system for phase iv of oc3. *Contract*, 1:31, May 2010.

[20] Christian Bak, Frederik Zahle, Robert Bitsche, Anders Yde, Lars Christian Henriksen, Anand Nata, and Morten Hartvig Hansen. Description of the dtu 10 mw reference wind turbine. *DTU Wind Energy Report-I-0092*, pages 1–138, June 2013.

[21] Geerten van de Kaa, Martijn van Ek, Linda M. Kamp, and Jafar Rezaei. Wind turbine technology battles: Gerbox versus direct drive - opening up the black box of technology characteristics. *Technological Forecasting and Social Change*, 153, April 2020.

[22] Wind turbine, Aug 2009. URL `https://en.wikipedia.org/wiki/File:Wind.turbine.components.and.coordinates.svg`. Accessed: 2020-04-19. Licensed under Creative Commons Attribution-ShareAlike 3.0.

[23] Power curve, Feb 2012. URL `https://commons.wikimedia.org/wiki/File:Powercurve.png`. Accessed: 2020-04-21. Licensed under Creative Commons Attribution-ShareAlike 3.0 Unported.

[24] Erich Hau. *Wind Turbines - Fundamentals, Technologies, Application, economics*, chapter 3, pages 81 – 86. Springer, Munich, Germany, 3 edition, 2013.

[25] Det Norske Veritas. Environmental conditions and environmental loads. Standard, Det Norske Veritas, Oct 2010.

[26] Astrid Nybø, Finn Gunnar Nielsen, Joachim Reuder, Matt Churchfield, and Marte Godvik. Evaluation of different wind fields for the investigation of the dynamic response of offshore wind turbines. *Wind Energy*, July 2019. Submitted for peer review.

[27] Rieska Mawarni Putri. A study of the coherences of turbulent wind on a floating offshore wind turbine. Master's thesis, University of Stavanger, June 2016.

[28] Maylinn Haaskjold Myrtvedt. Investigation of the importance of wind field modelling for loads on a bottom fixed and spar floater wind turbine. Master's thesis, University of Bergen, Aug 2019.

[29] Ship movements on the wave, May 2006. URL `https://commons.wikimedia.org/wiki/File:Brosen_shipsmovemensonthewave.svg`. Accessed: 2020-04-22. Licensed under GNU Free Documentation License.

[30] Bjørnar Pettersen. *Marin teknikk 3 Hydrodynamikk*. Akademika, 2017.

[31] Sébastien Gueydon. Aerodynamic damping on a semisubmersible floating foundation for wind turbines. *Energy procedia*, 94:367 – 378, Sept 2016.

[32] Finn Gunnar Nielsen. *Lecture Notes ch. 7 - Floating Support Structures*. Geophysical Institute, University of Bergen, March 2020. Incomplete draft version, 16.03.2020.

[33] Lecture Notes in Introduction to Dynamics and Vibrations. Ch. 5.5 - introduction to vibration of systems with many degrees of freedom, 2019. URL `https://www.brown.edu/Departments/Engineering/Courses/En4/Notes/vibrations_mdof/vibrations_mdof.htm`.

[34] DNVGL. Floating wind turbine structures. Standard, Det Norske Veritas, July 2018.

[35] E.C. Tupper. *Introduction to Naval Architecture*. Elsevier Science & Technology, Amsterdam, 5 edition, 2013. ISBN 9780080982724.

[36] Metacentric height, Sep 2011. URL `https://commons.wikimedia.org/wiki/File:MetacentricHeight.svg`. Accessed: 2020-05-21. Licensed under Creative Commons Attribution-ShareAlike 2.5 Generic.

[37] Robert W. Fox, Alan T. McDonald, Philip J. Pritchard, and John C. Leylegian. *Fluid Mechanics*. John Wiley and Sons, Inc., Hoboken, NJ, 8 edition, 2012. ISBN 978-1-118-02641-0.

[38] J.N. Newman. *Marine Hydrodynamics*. The MIT Press, Cambridge, Massachusetts, 2018. ISBN 0-262-53482-7.

[39] DNV GL. *Sesam User Manual - GeniE*. DNV GL Software, Feb 2016.

[40] DNV GL. *Sesam User Manual - HydroD*. DNV GL Software, Dec 2016.

[41] DNV GL. *Sesam User Manual - Wadam*. DNV GL Software, March 2017.

[42] Finn Gunnar Nielsen. *Lecture Notes ch. 5 - Linear dynamics*. Geophysical Institute, University of Bergen, Jan 2020. Incomplete draft version, 20.01.2020.

[43] Wenfei Xue. Design, numerical modelling and analysis of a spar floater supporting the dtu 10mw wind turbine. Master's thesis, Norwegian University of Science and Technology, July 2017.

[44] Meng Long, Zhou Tao, He Yan-ping, Zhao Yong-sheng, and Liu Ya-dong. Concept design and coupled dynamic response analysis on 6-mw spar-type floating offshore wind turbine. *Chine Ocean Eng.*, 31(5):567 – 577, July 2017.

[45] Meng Long, He Yanping, Zhou Tao, Zhao Yongsheng, and Liu Yadong. Research on dynamic response characteristics of 6 mw spar-type floating offshore wind turbine. *Journal of Shanghai Jiaotong University (Science)*, 23(4):505 – 514, 2018.

[46] Zhengshun Cheng, Kai Wang, Zhen Gao, and Torgeir Moan. A comparative study on dynamic responses of spar-type floating horizontal and vertical axis wind turbines. *Wind Energy*, 20(2):305 – 323, 2017.

A Mass, damping and restoring matrices and graphs

Appendix A includes the elements of the dry mass and restoring matrices, as well as the added mass and potential damping matrices used in the analyses (for the natural period in pitch for each draft). Graphs of the frequency dependent added mass and potential damping in surge, surge-pitch, heave and pitch for all drafts are also included. The data are collected from Wadam.

Draft	Md_{11}	Md_{33}	Md_{55}	Md_{13}	Md_{15}	Md_{35}
120	1.69e7	1.69e7	1.71e11	0	-1.38e9	0
100	1.89e7	1.89e7	1.39e11	0	-1.31e9	0
80	2.20e7	2.20e7	1.11e11	0	-1.25e9	0
60	2.79e7	2.79e7	8.66e10	0	-1.23e9	0

Table 19: Dry mass matrix elements

Draft	A_{11}	A_{33}	A_{55}	A_{13}	A_{15}	A_{35}
120	1.62e7	8.49e5	7.85e10	0	-1.01e9	0
100	1.76e7	1.48e6	6.0e10	0	-9.32e8	0
80	1.95e7	3.06e5	4.35e10	0	-8.51e8	0
60	2.18e7	8.30e6	2.91e10	0	-7.59e8	0

Table 20: Added mass matrix elements used in the dynamic response analyses

Draft	$B_{P,11}$	$B_{P,33}$	$B_{P,55}$	$B_{P,13}$	$B_{P,15}$	$B_{P,35}$
120	2.56e3	1.27e1	9.06e6	0	-1.52e5	0
100	4.49e3	5.30e2	1.17e7	0	-2.29e5	0
80	1.08e4	1.34e4	1.95e7	0	-4.59e5	0
60	2.64e4	1.15e4	3.10e7	0	-9.04e5	0

Table 21: Potential damping matrix elements used in the dynamic response analyses

Draft	$C_{H,11}$	$C_{H,33}$	$C_{H,55}$	$C_{H,13}$	$C_{H,15}$	$C_{H,35}$
120	0	5.44e5	2.93e9	0	0	0
100	0	5.44e5	2.77e9	0	0	0
80	0	5.44e5	2.58e9	0	0	0
60	0	5.44e5	2.38e9	0	0	0

Table 22: Hydrostatic stiffness matrix elements

Draft	$C_{M,11}$	$C_{M,33}$	$C_{M,55}$	$C_{M,13}$	$C_{M,15}$	$C_{M,35}$
120	1e5	0	5.21e8	0	-7.22e6	0
100	1e5	0	3.27e8	0	-6.15e6	0
80	1e5	0	2.57e8	0	-5.07e6	0
60	1e5	0	1.60e8	0	-4.00e6	0

Table 23: Mooring stiffness matrix elements

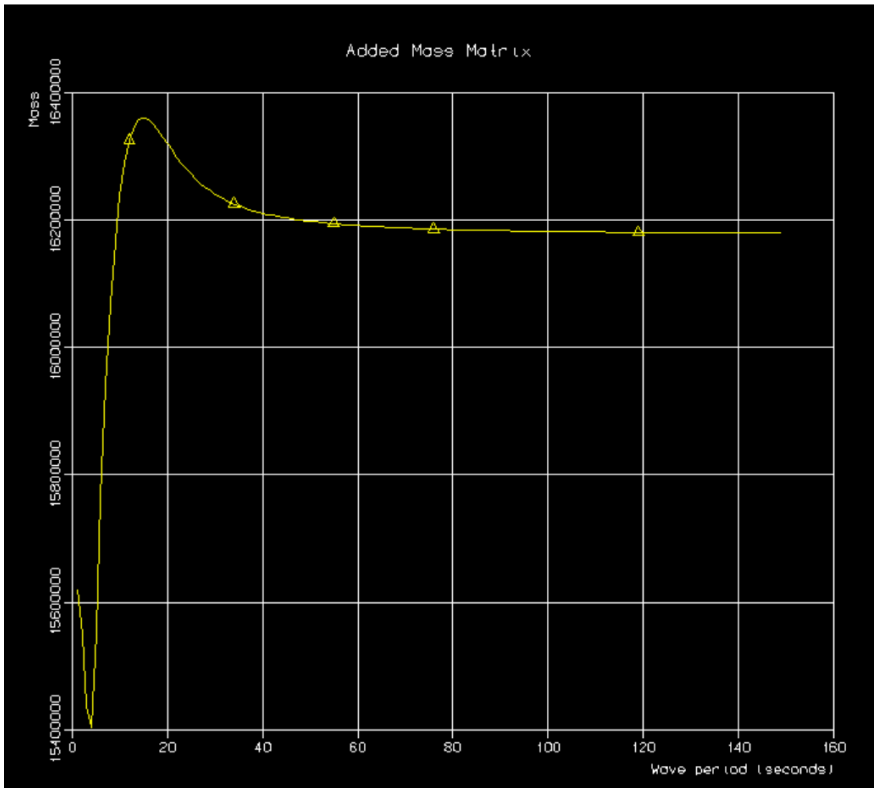

Figure 23: Added mass in surge, 120 m draft

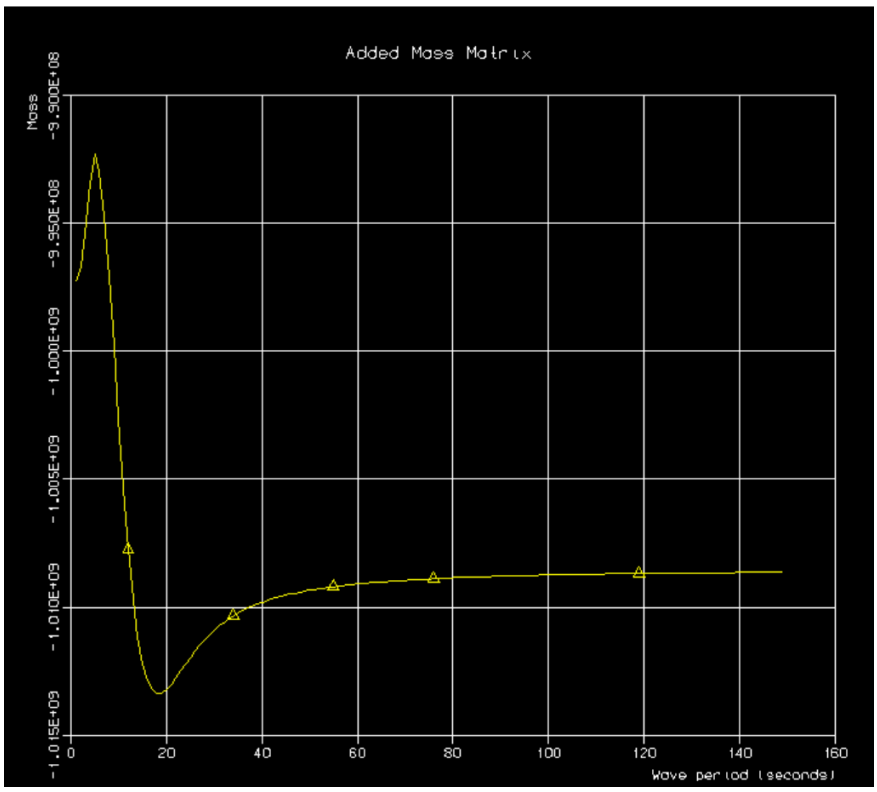

Figure 24: Added mass in coupled surge-pitch, 120 m draft

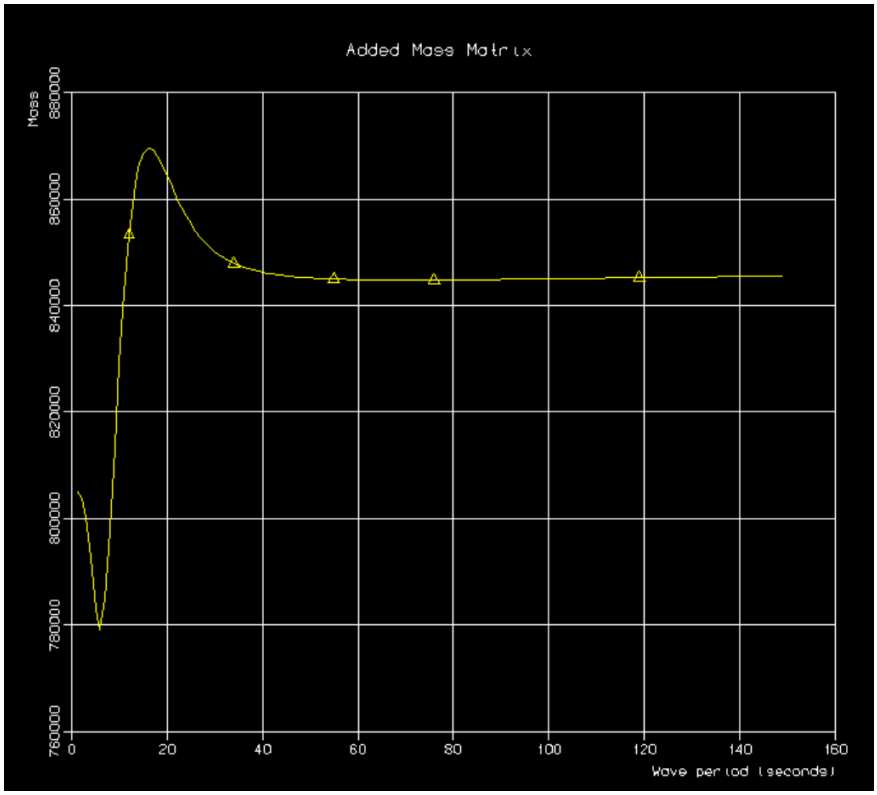

Figure 25: Added mass in heave, 120 m draft

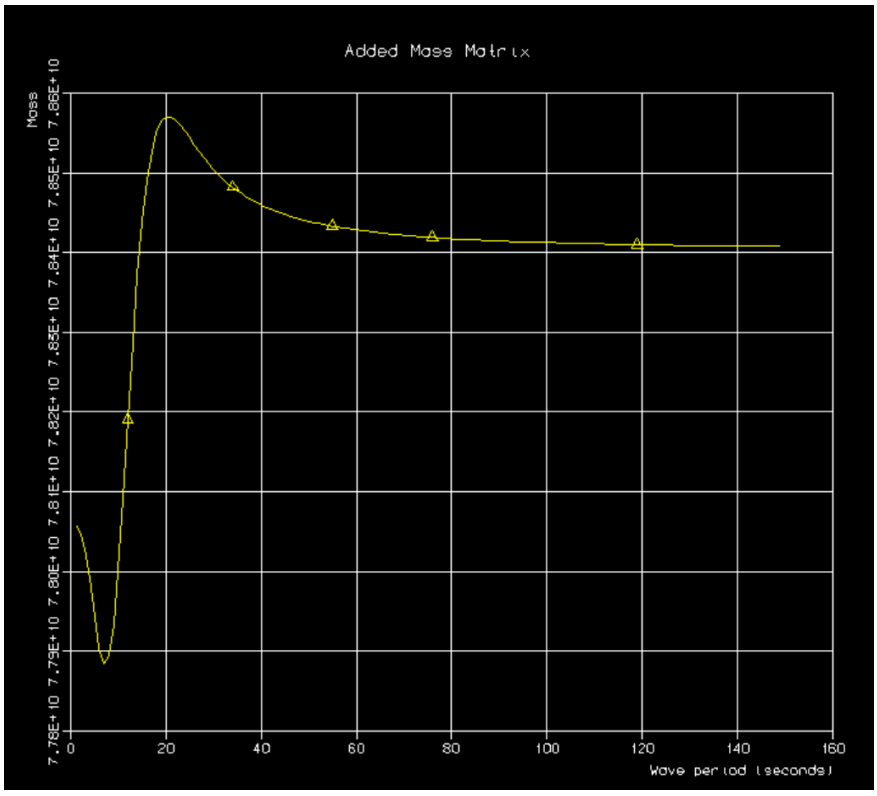

Figure 26: Added mass in pitch, 120 m draft

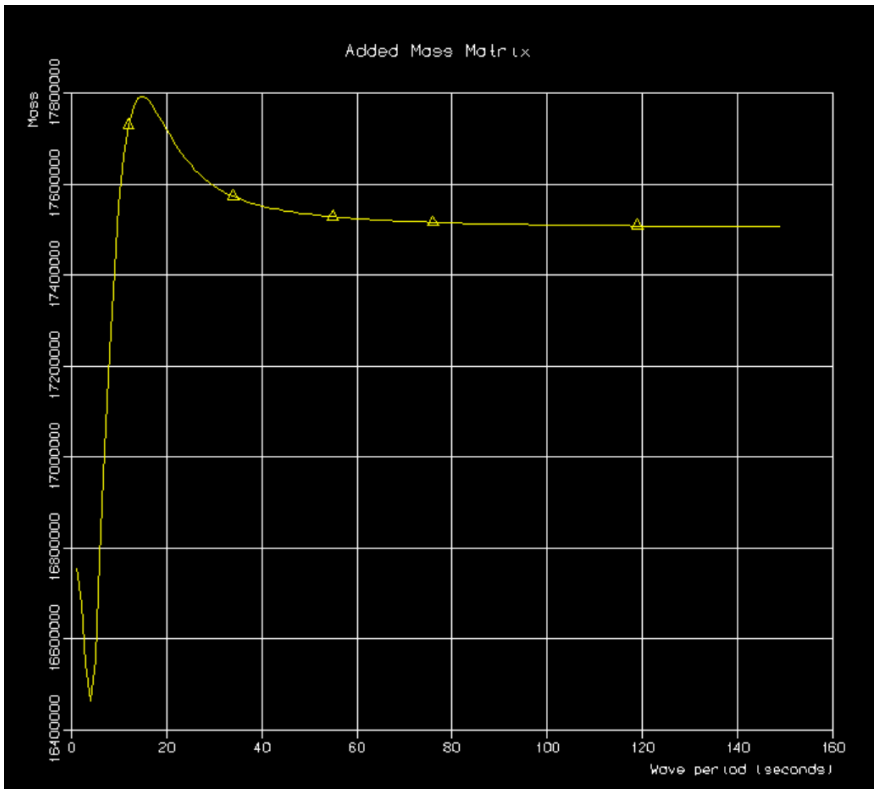

Figure 27: Added mass in surge, 100 m draft

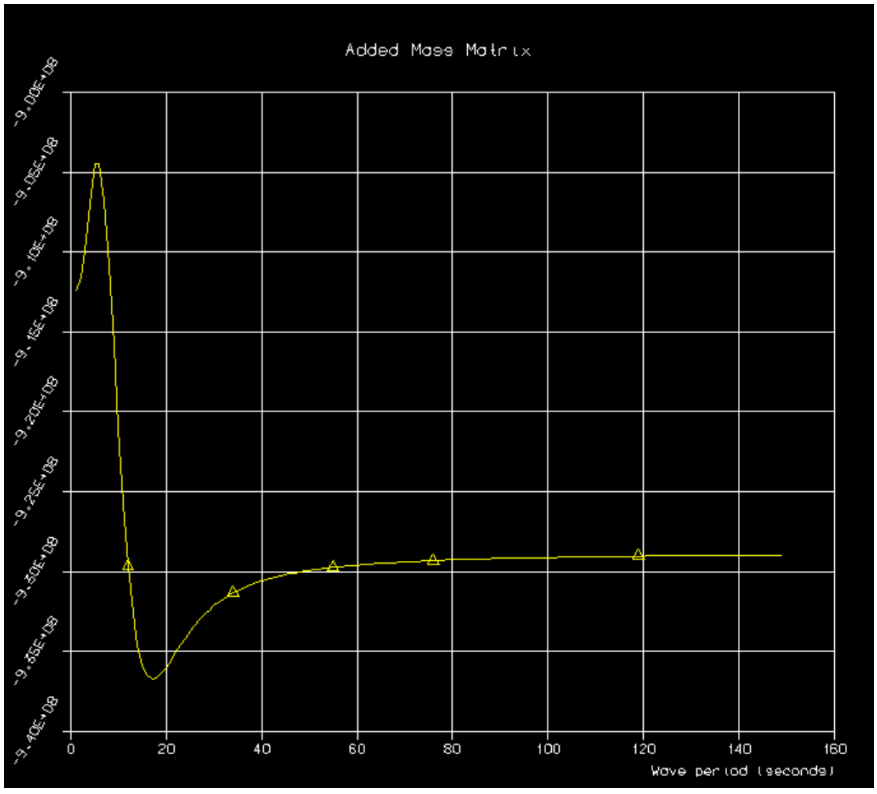

Figure 28: Added mass in coupled surge-pitch, 100 m draft

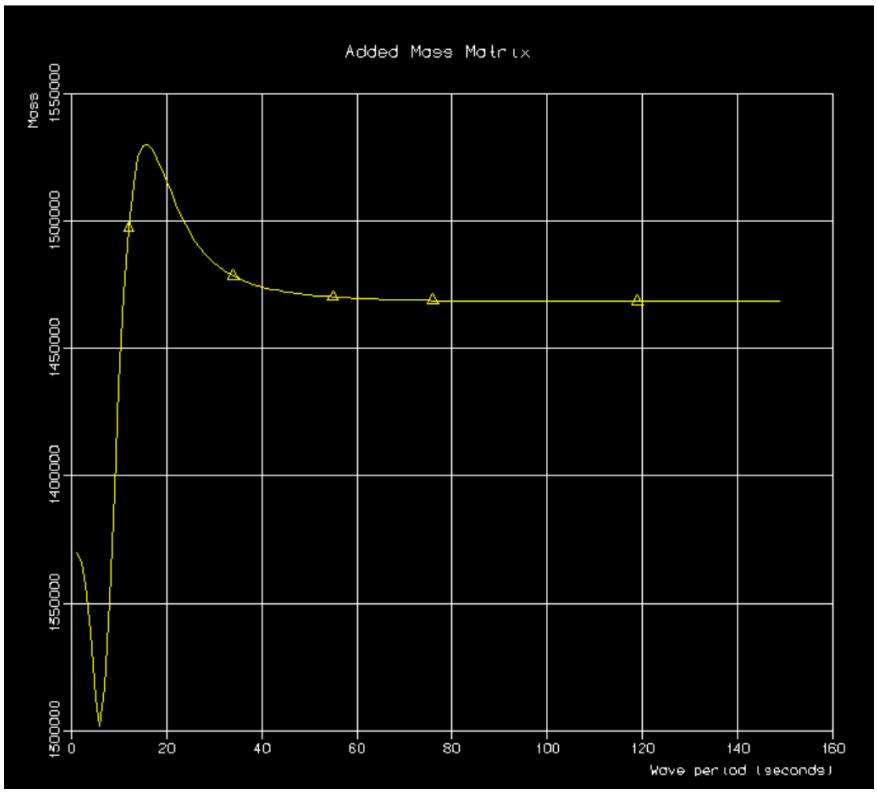

Figure 29: Added mass in heave, 100 m draft

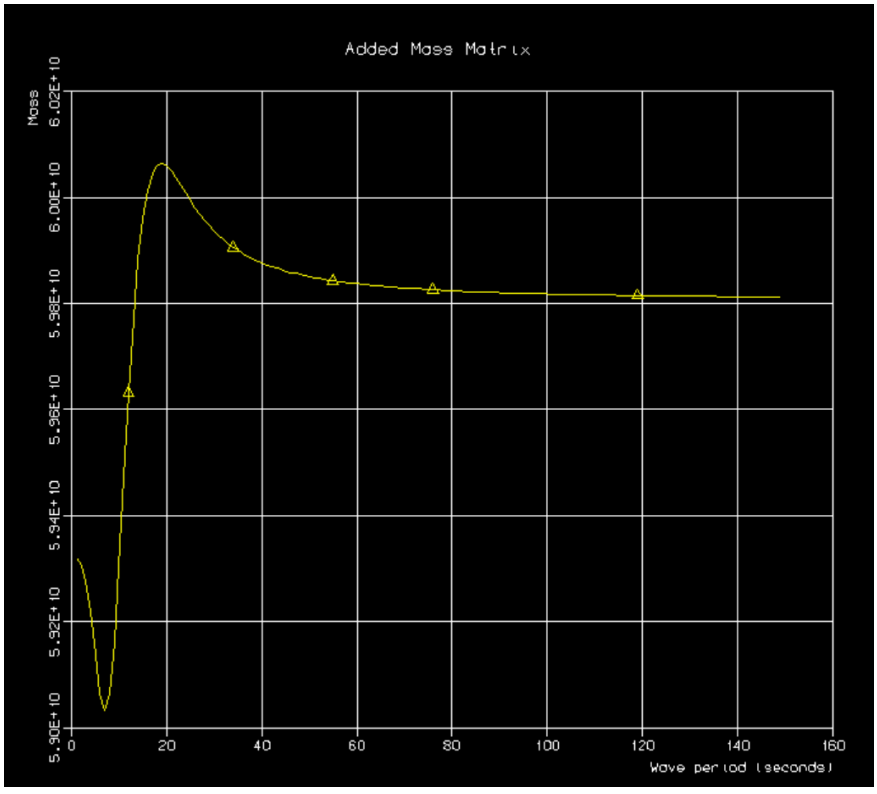

Figure 30: Added mass in pitch, 100 m draft

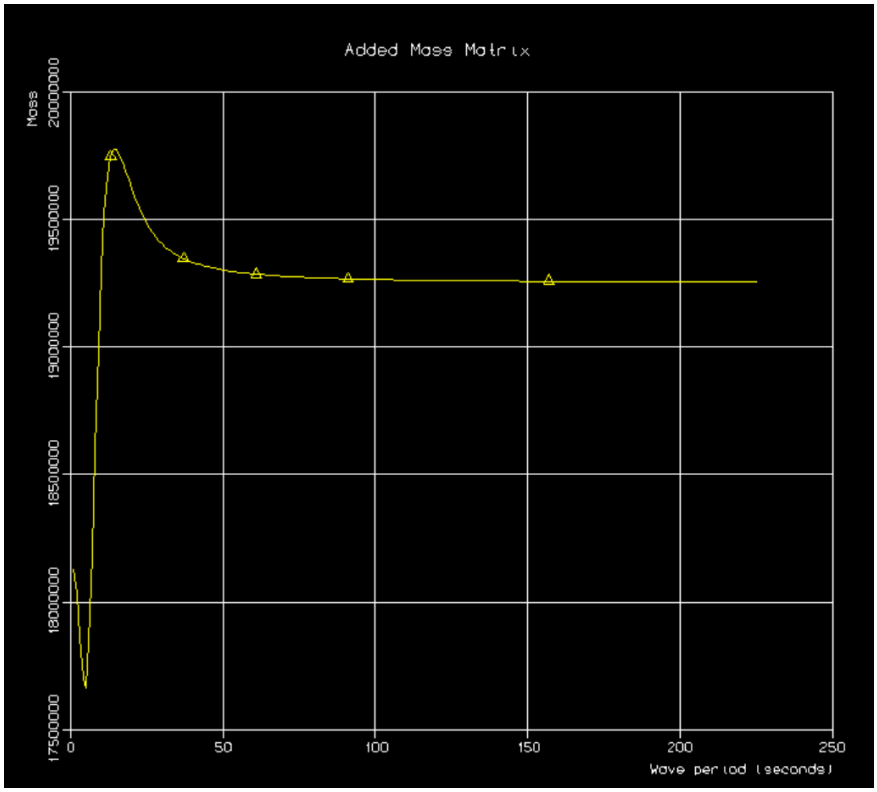

Figure 31: Added mass in surge, 80 m draft

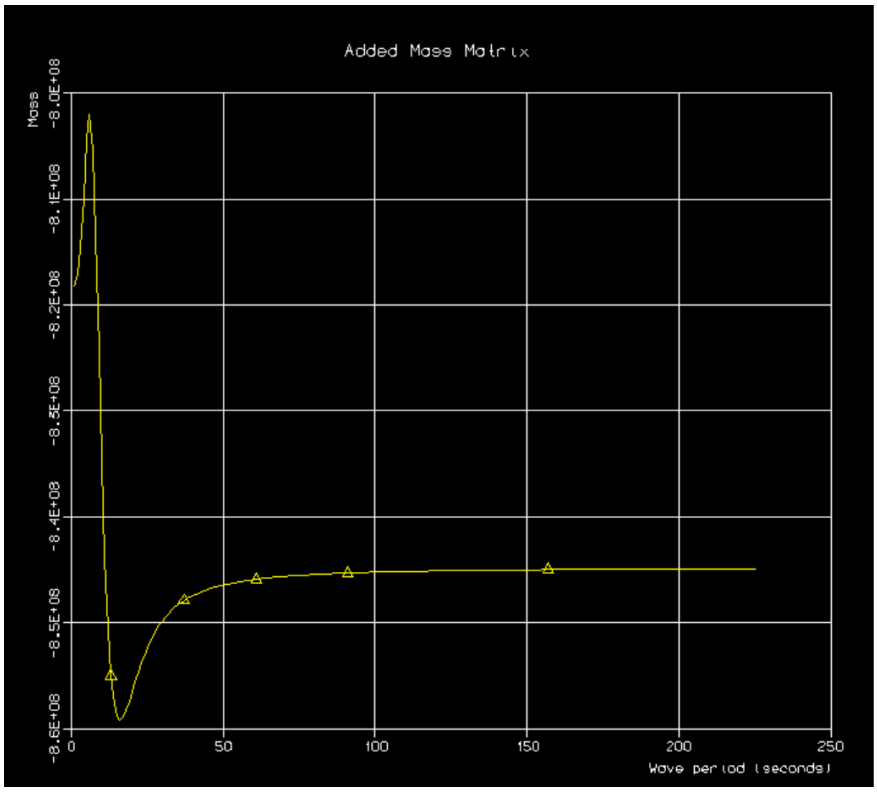

Figure 32: Added mass in coupled surge-pitch, 80 m draft

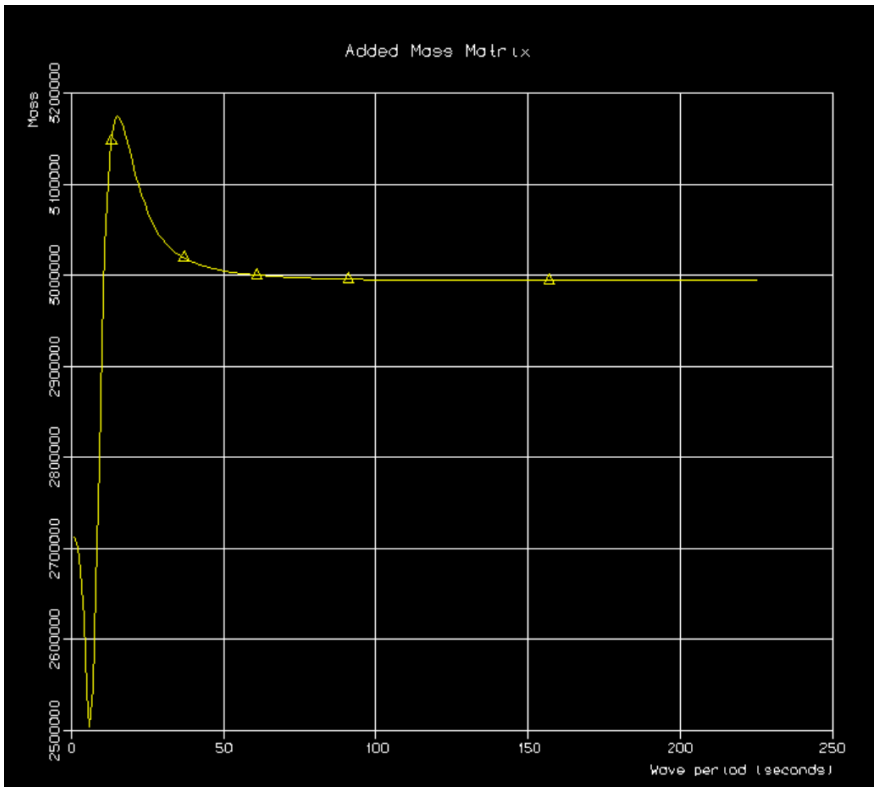

Figure 33: Added mass in heave, 80 m draft

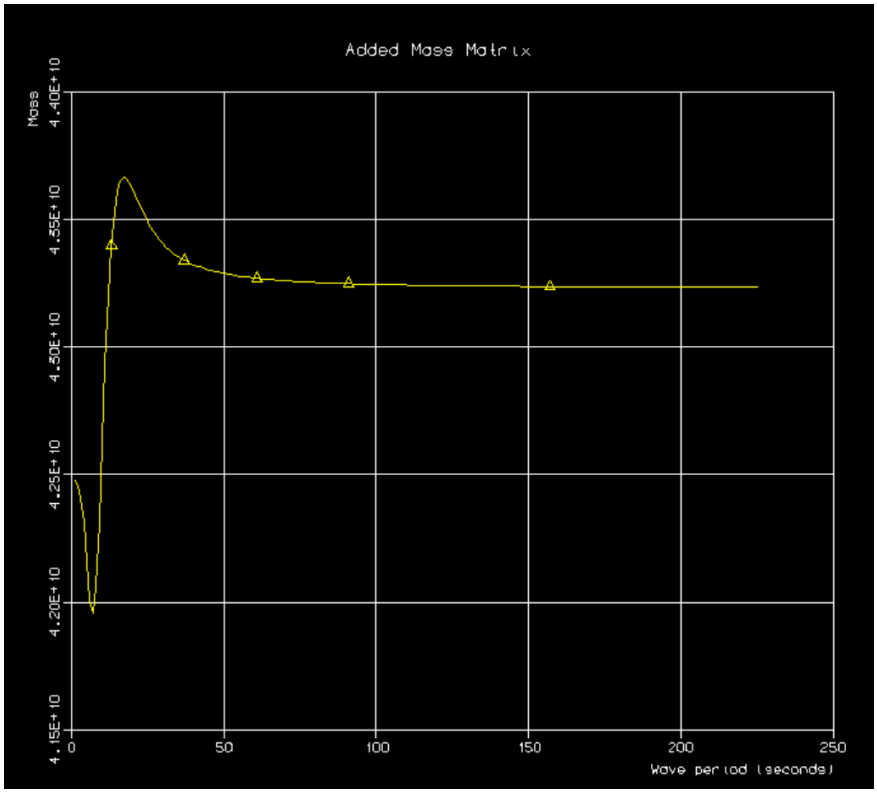

Figure 34: Added mass in pitch, 80 m draft

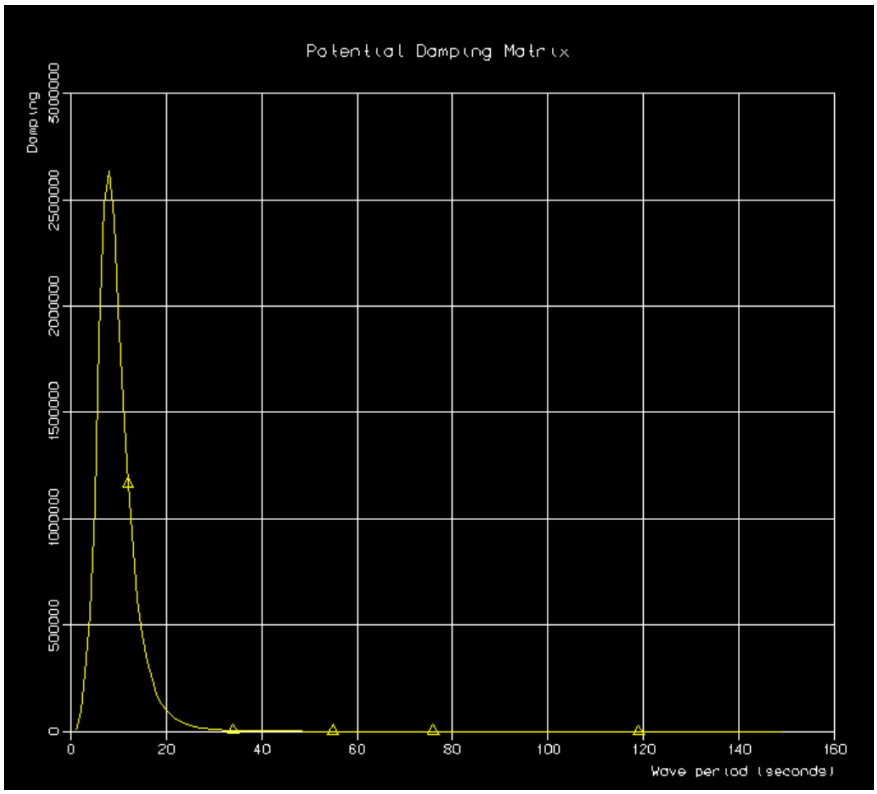

Figure 35: Potential damping in surge, 60 m draft

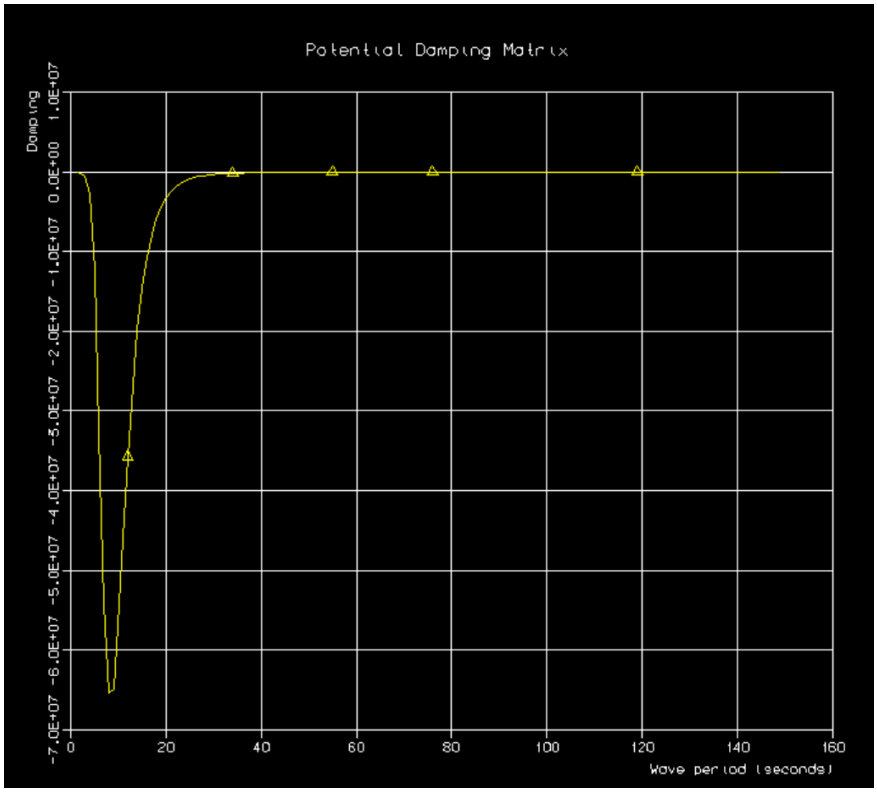

Figure 36: Potential damping in coupled surge-pitch, 60 m draft

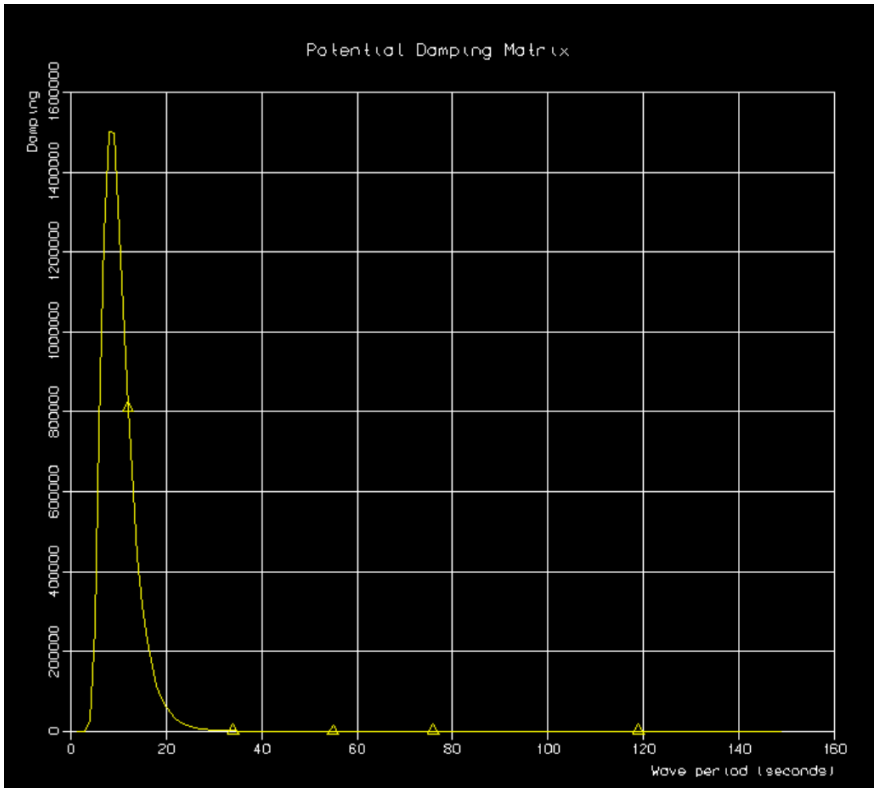

Figure 37: Potential damping in heave, 60 m draft

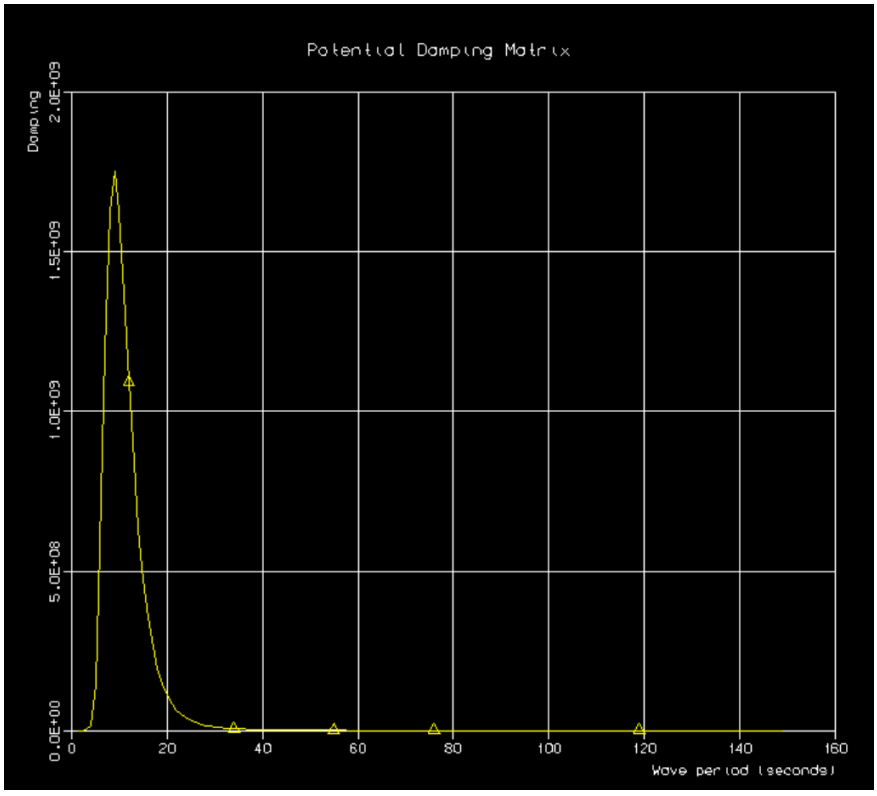

Figure 38: Potential damping in pitch, 60 m draft

B Dynamic response in surge and pitch measured at center of gravity

When the responses were measured at SWL, the surge motion were greatly affected by the pitch motion, especially for large drafts. Therefore the dynamic response at z_G were also investigated for 120 and 60 m draft, in surge (tab. 24) and pitch (tab. 25). These analyses are only run for one wave and wind realization, which cause some inaccuracies, especially for maximum/minimum values. As expected the responses in pitch remains the same, while the responses in surge are smaller. The difference in the surge response for 120 and 60 m draft are very small, unlike when the responses were measured at SWL.

Surge				
Load case no. 1				
Draft [m]	Mean [m]	St.dev. [m]	Max. [m]	Min. [m]
120	6.48	0.93	9.47	4.14
60	6.74	1.17	10.40	3.52
Load case no. 2				
Draft [m]	Mean [m]	St.dev [m]	Max. [m]	Min. [m]
120	12.14	4.24	20.53	2.56
60	12.38	4.02	20.78	4.58
Load case no. 3				
Draft [m]	Mean [m]	St.dev [m]	Max. [m]	Min. [m]
120	7.43	1.71	12.99	2.37
60	7.78	1.46	12.62	2.58

Table 24: Dynamic response in surge measured at center of gravity

Pitch				
Load case no. 1				
Draft [m]	Mean [m]	St.dev. [m]	Max. [m]	Min. [m]
120	2.58	0.23	3.25	1.73
60	2.66	0.38	3.97	1.27
Load case no. 2				
Draft [m]	Mean [m]	St.dev [m]	Max. [m]	Min. [m]
120	4.81	1.20	8.56	1.00
60	4.86	1.07	8.16	1.73
Load case no. 3				
Draft [m]	Mean [m]	St.dev [m]	Max. [m]	Min. [m]
120	2.94	0.38	4.41	1.32
60	3.08	1.34	9.77	-3.23

Table 25: Dynamic response in pitch measured at center of gravity

C Time series of the dynamic response

Appendix A includes time series of motion response in surge, heave and pitch for all drafts and load cases. These are made using the same seed number for the wave and wind realization.

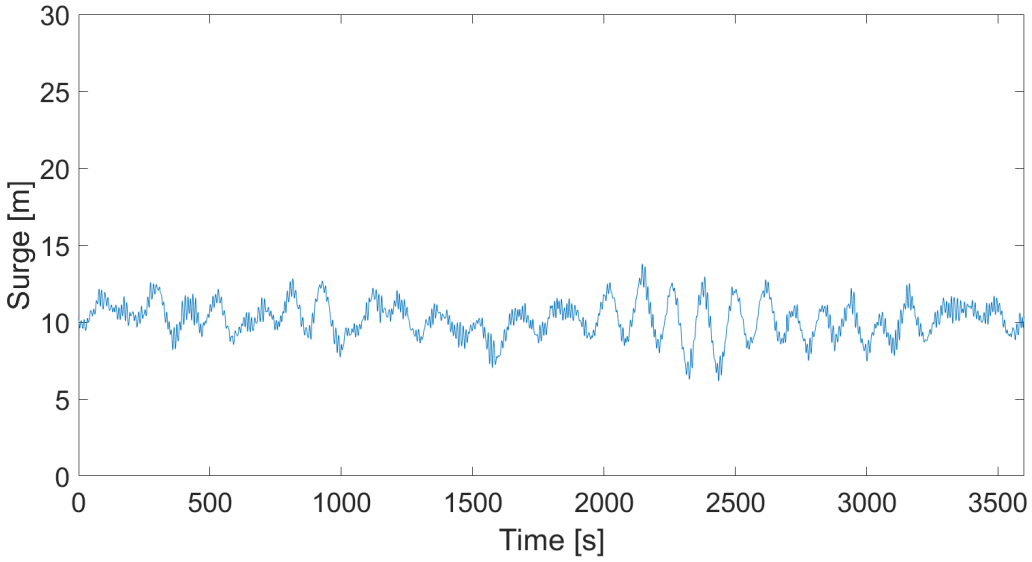

Figure 39: Dynamic response in surge, LC1, draft = 120 m

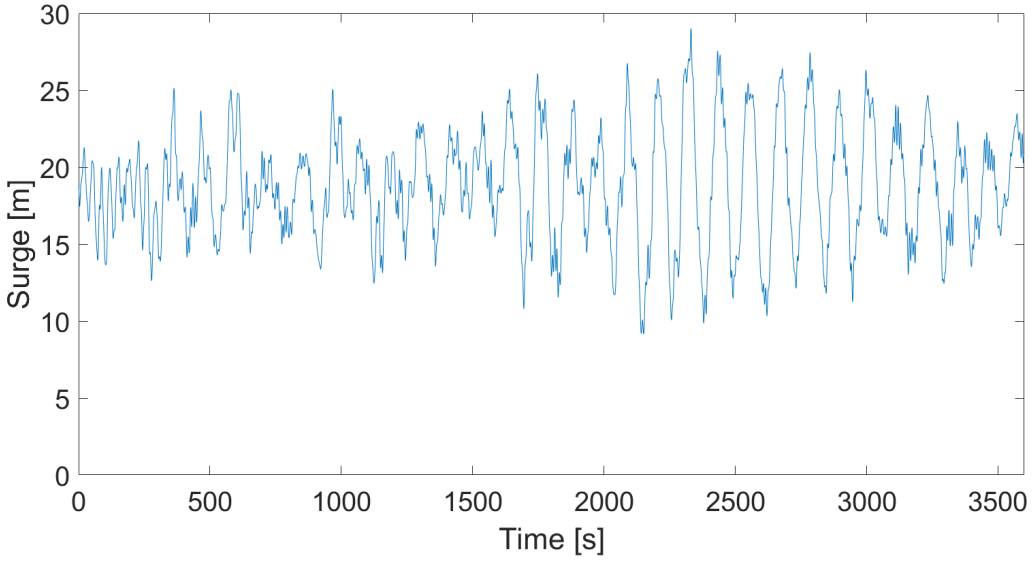

Figure 40: Dynamic response in surge, LC2, draft = 120 m

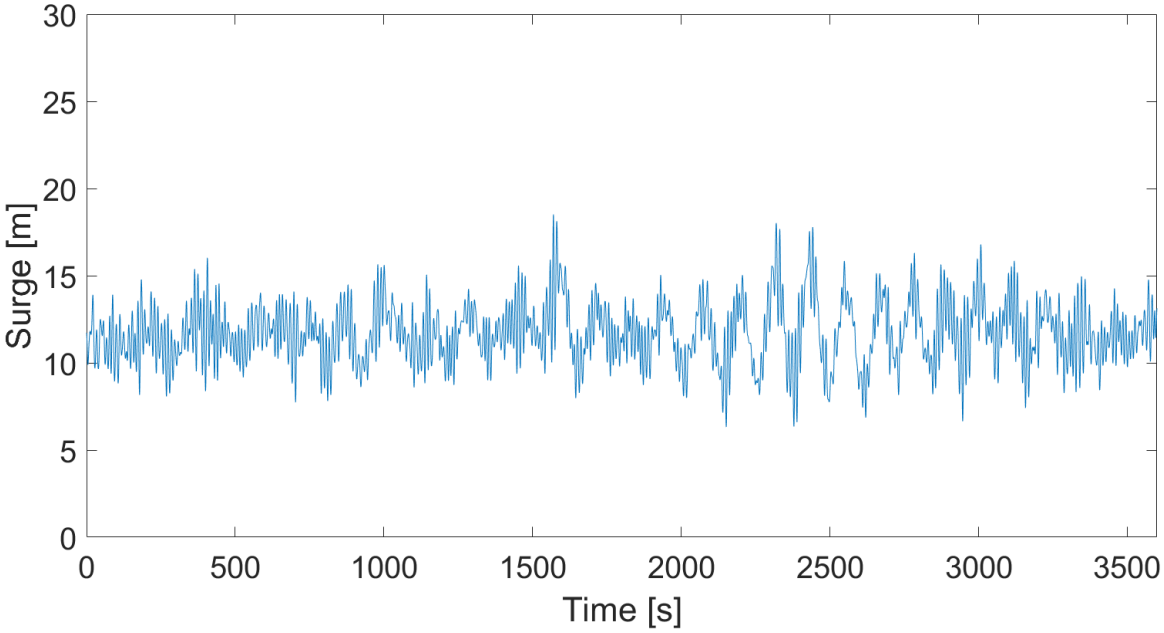

Figure 41: Dynamic response in surge, LC3, draft = 120 m

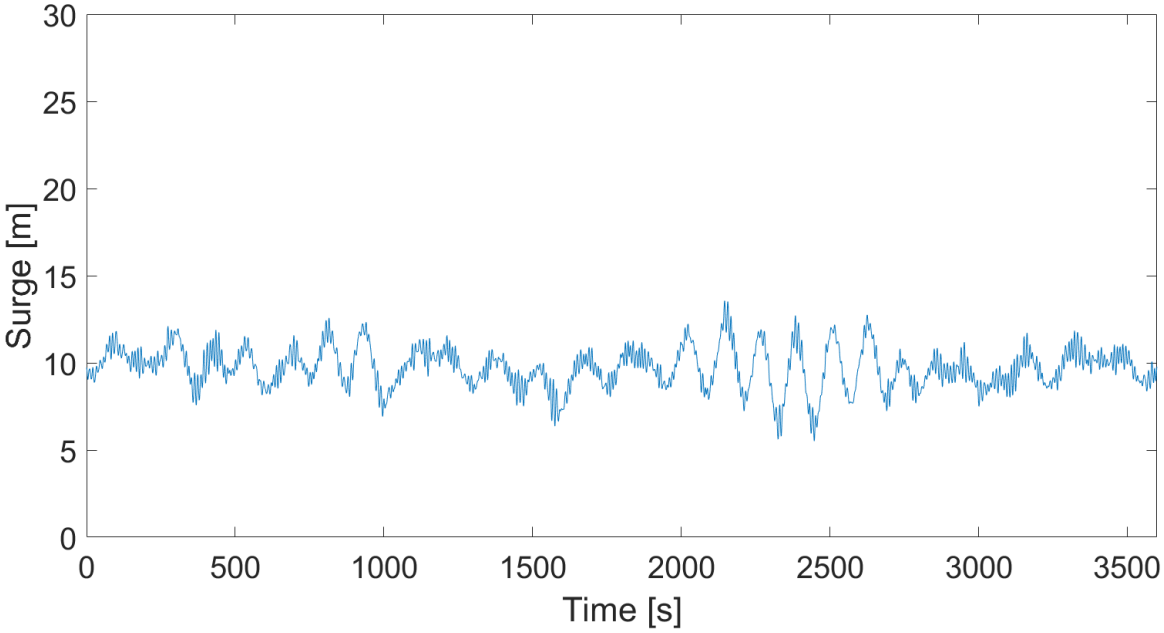

Figure 42: Dynamic response in surge, LC1, draft = 100 m

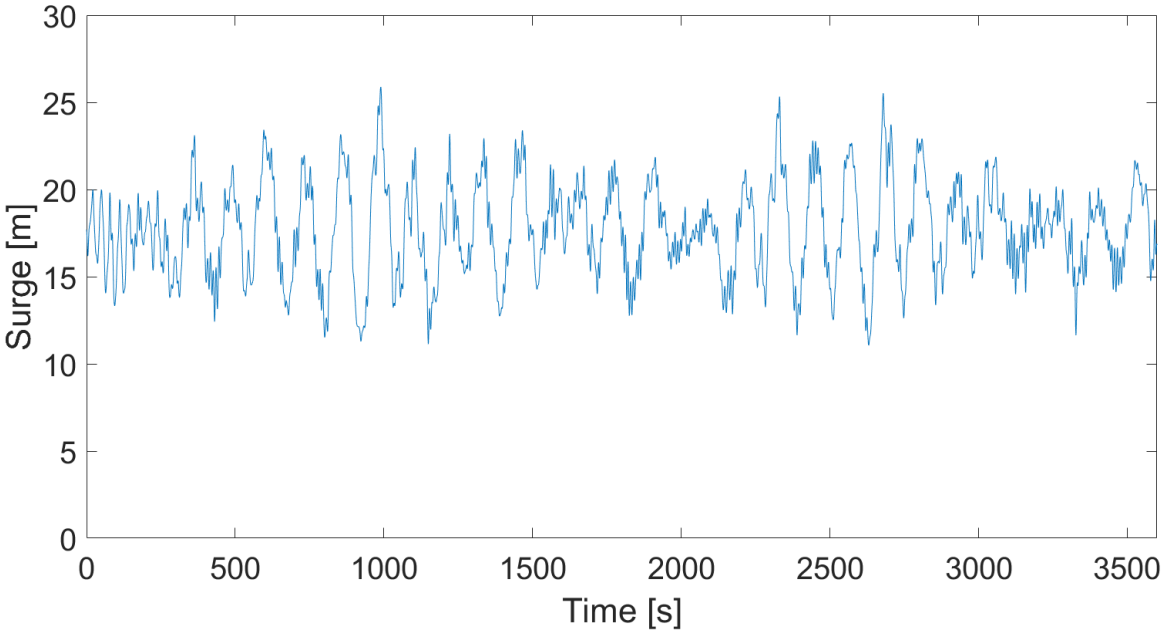

Figure 43: Dynamic response in surge, LC2, draft = 100 m

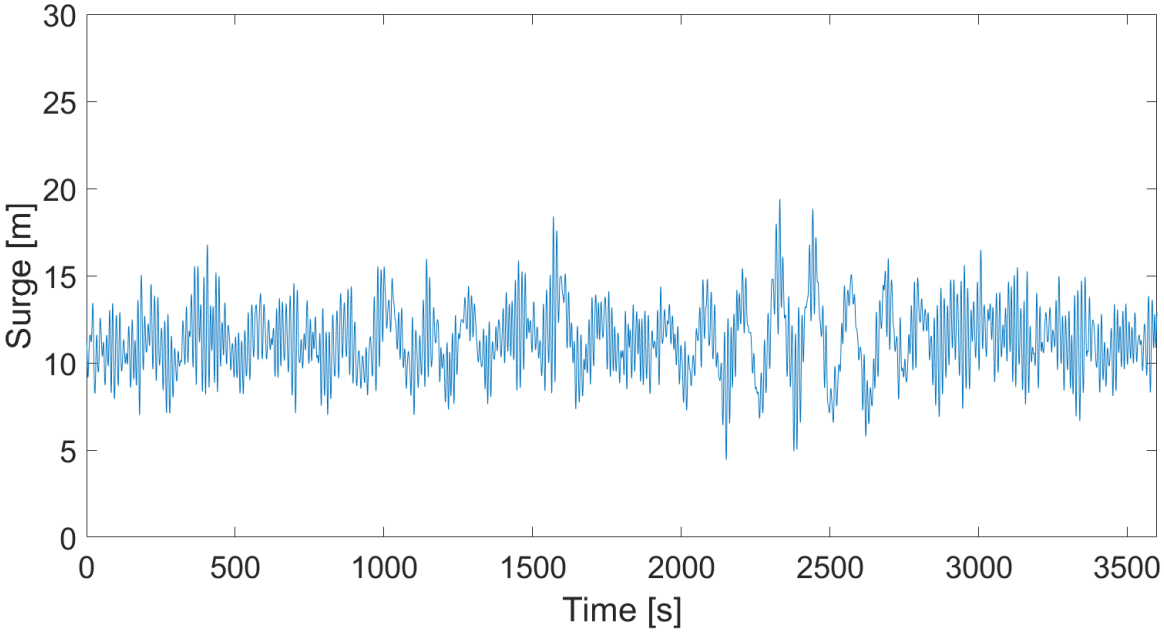

Figure 44: Dynamic response in surge, LC3, draft = 100 m

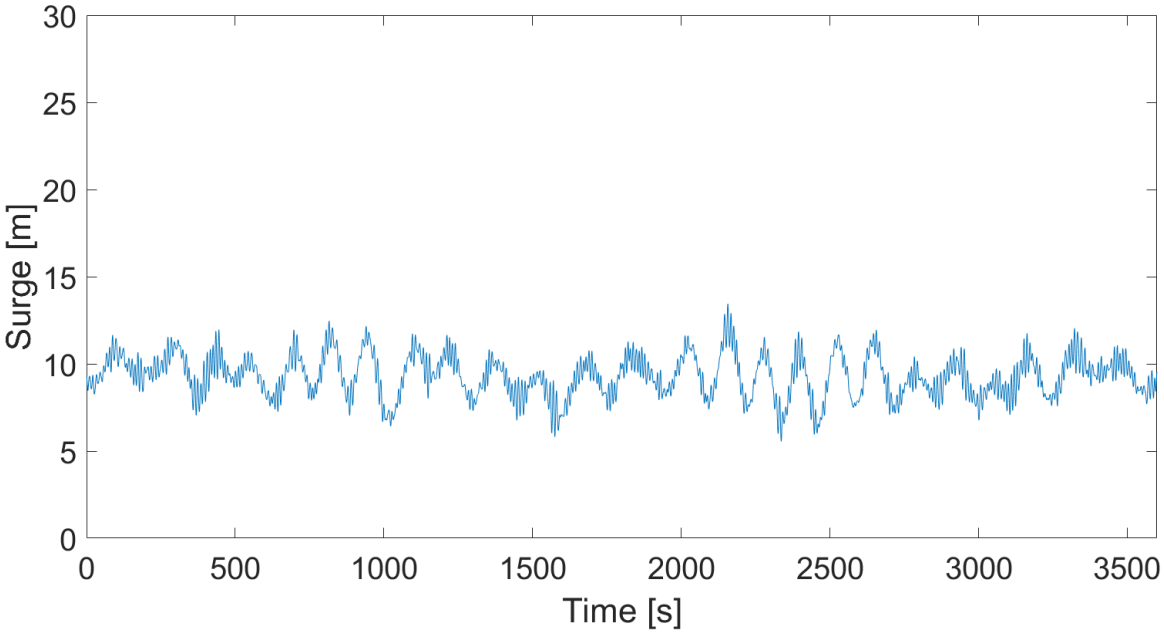

Figure 45: Dynamic response in surge, LC1, draft = 80 m

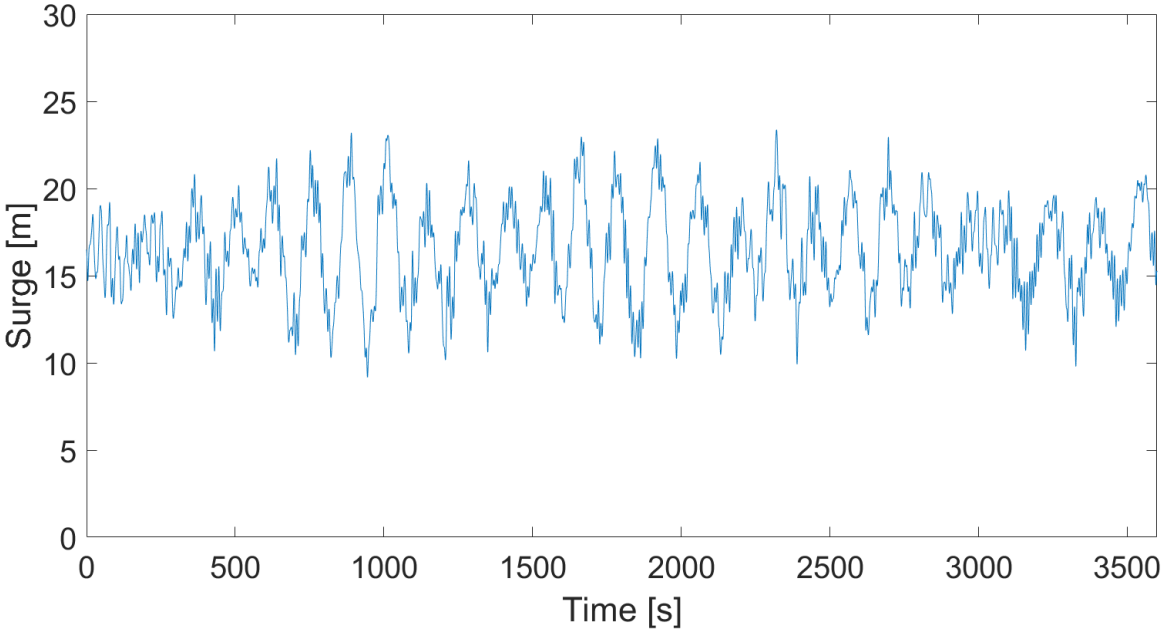

Figure 46: Dynamic response in surge, LC2, draft = 80 m

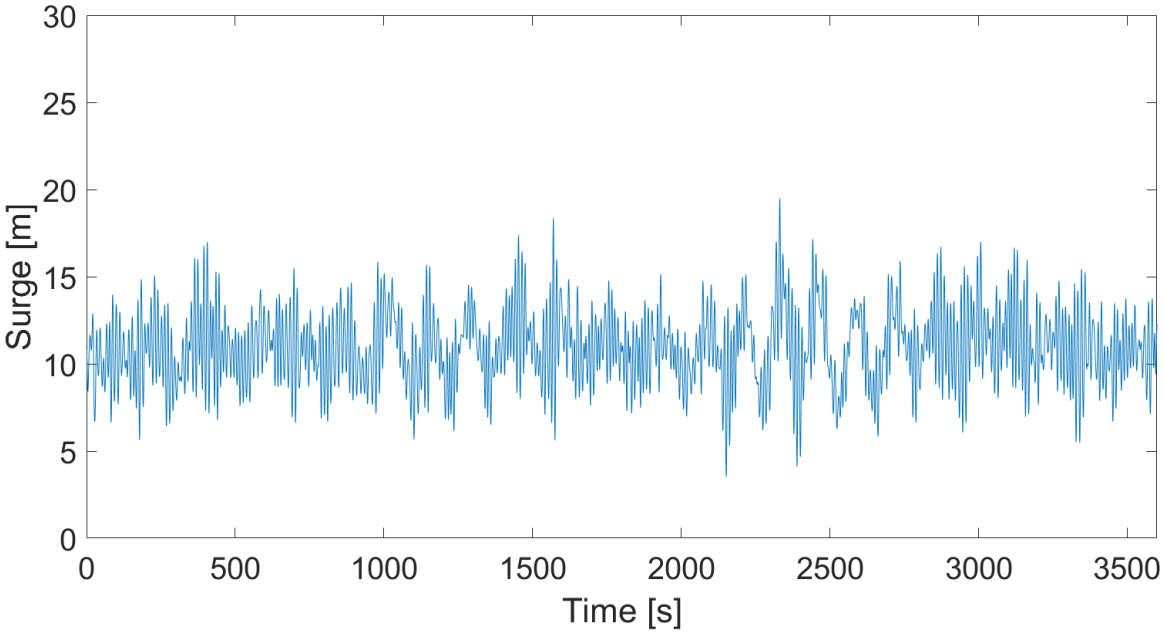

Figure 47: Dynamic response in surge, LC3, draft = 80 m

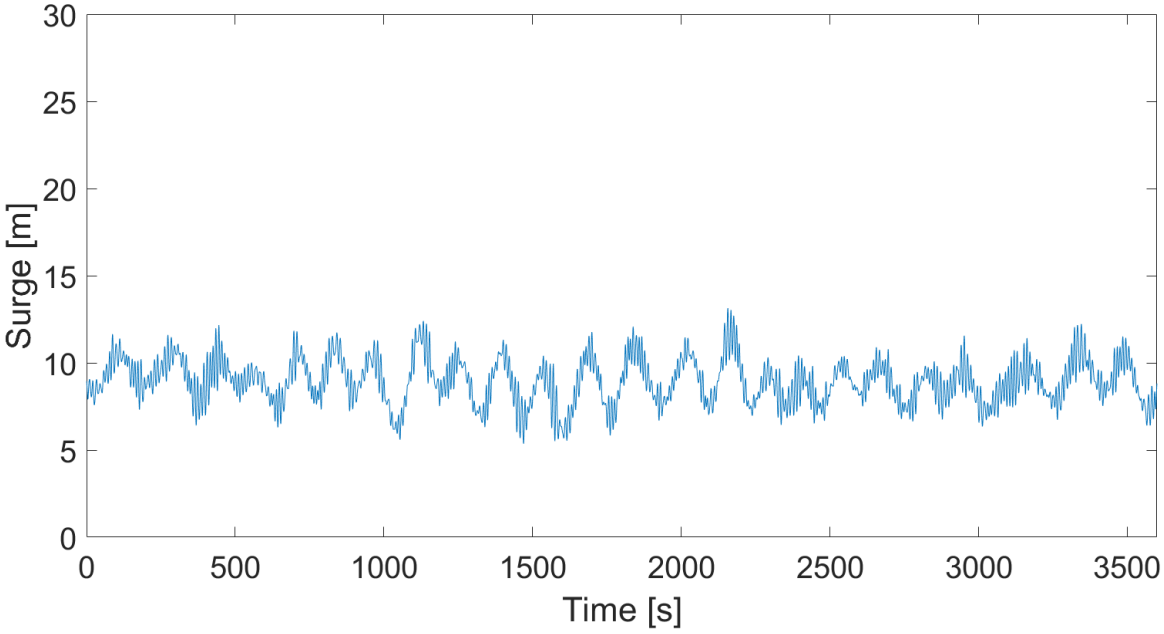

Figure 48: Dynamic response in surge, LC1, draft = 60 m

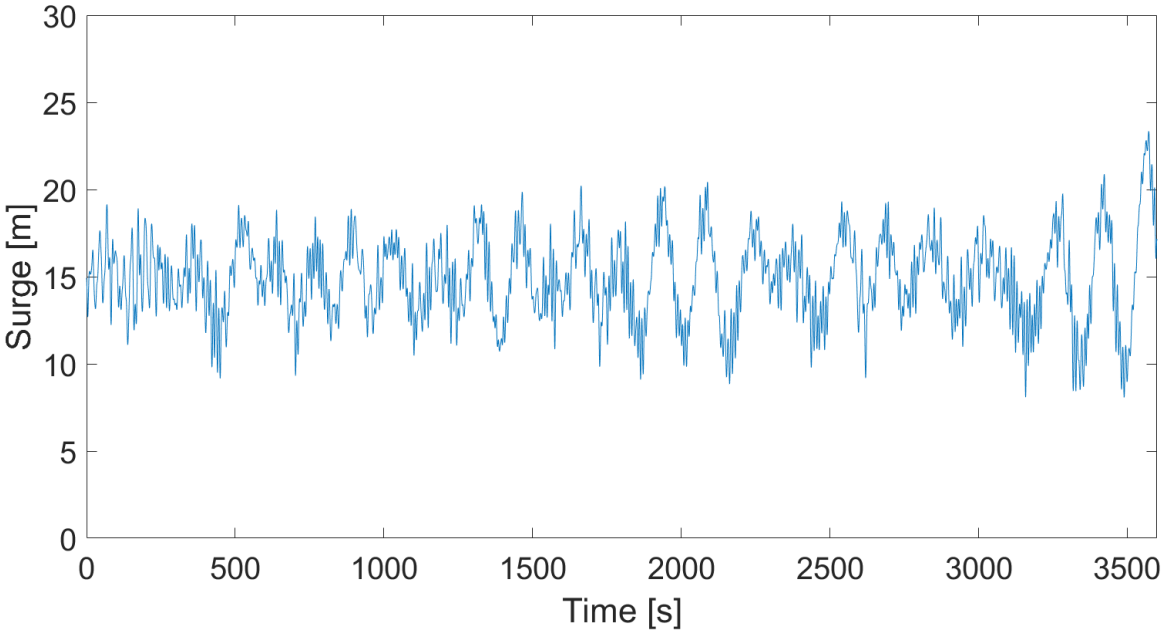

Figure 49: Dynamic response in surge, LC2, draft = 60 m

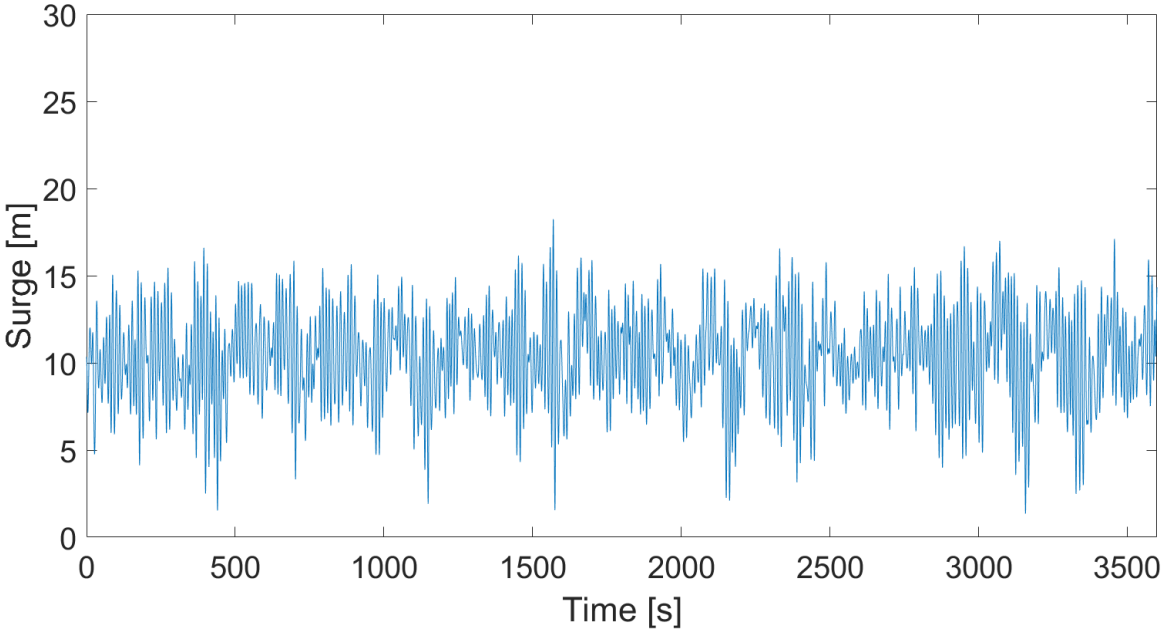

Figure 50: Dynamic response in surge, LC3, draft = 60 m

Heave

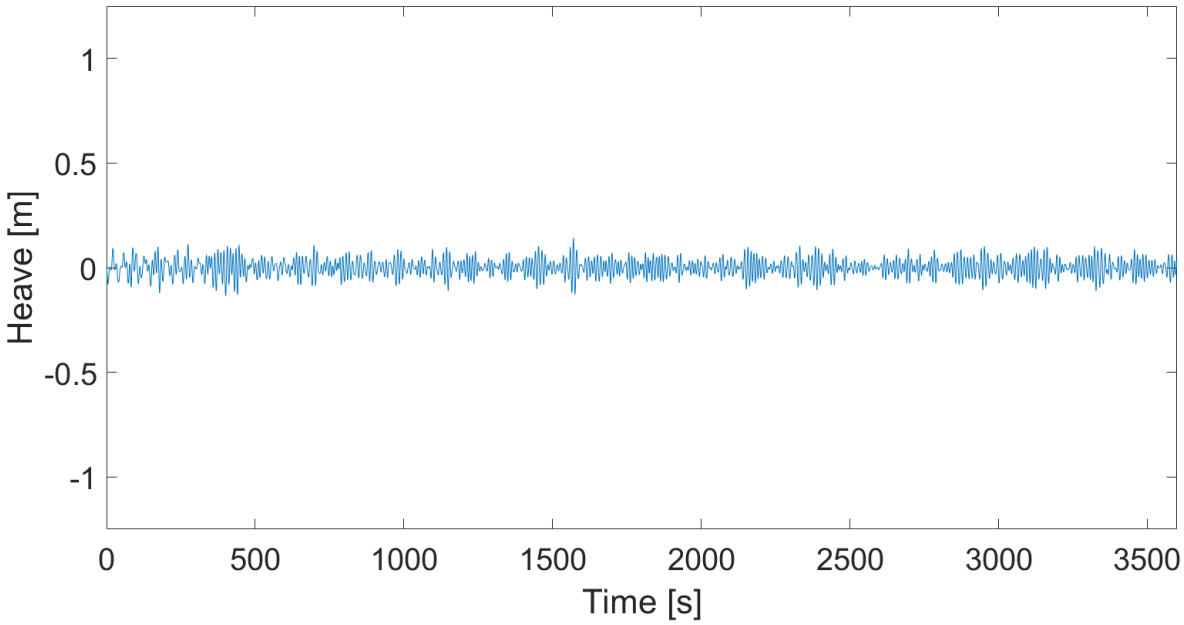

Figure 51: Dynamic response in heave, LC1, draft = 120 m

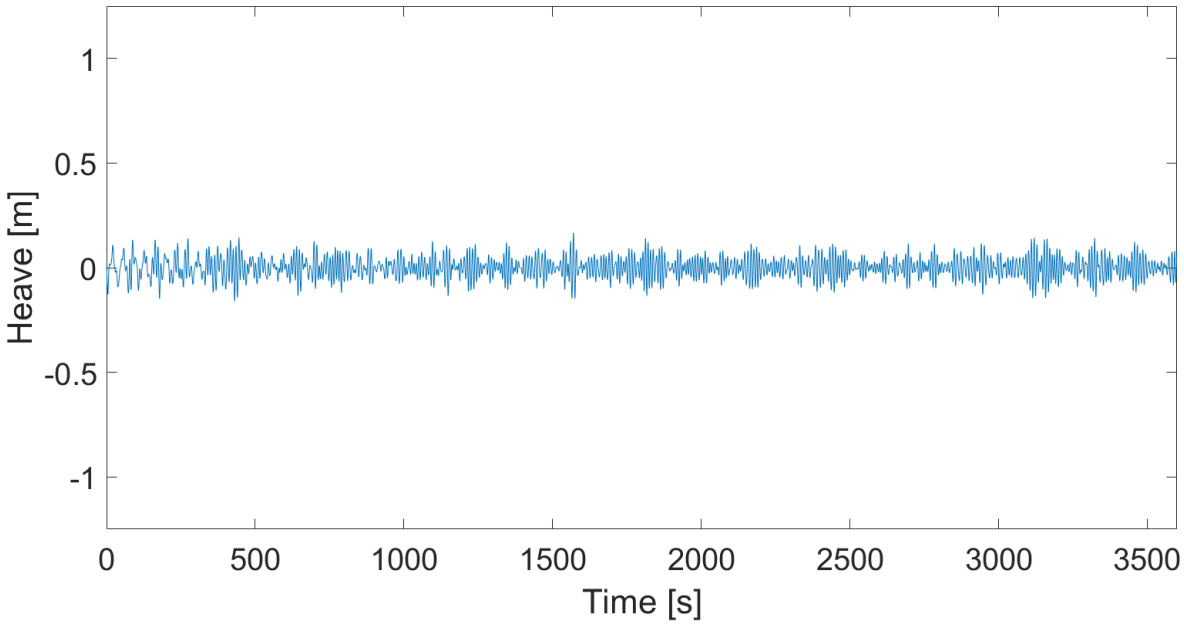

Figure 52: Dynamic response in heave, LC2, draft = 120 m

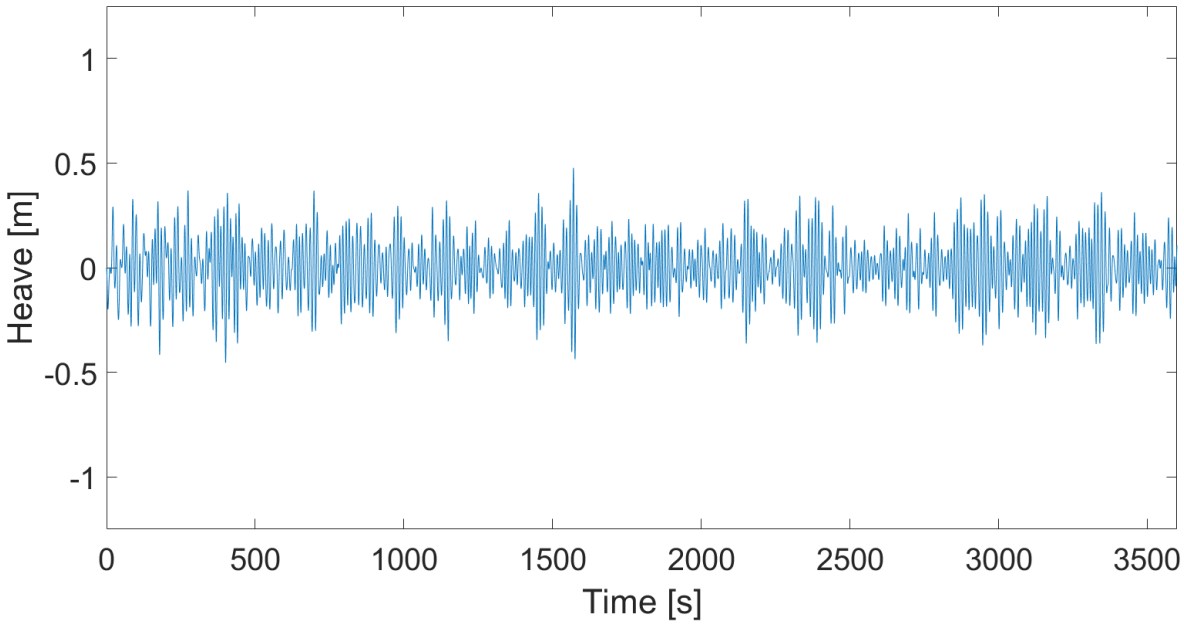

Figure 53: Dynamic response in heave, LC3, draft = 120 m

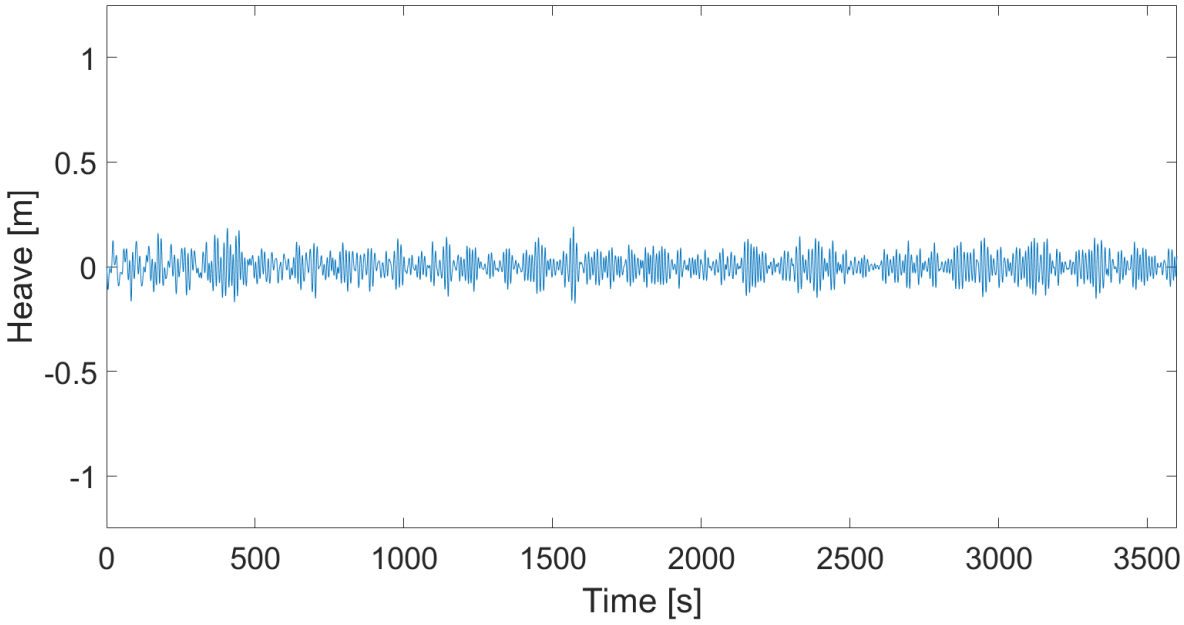

Figure 54: Dynamic response in heave, LC1, draft = 100 m

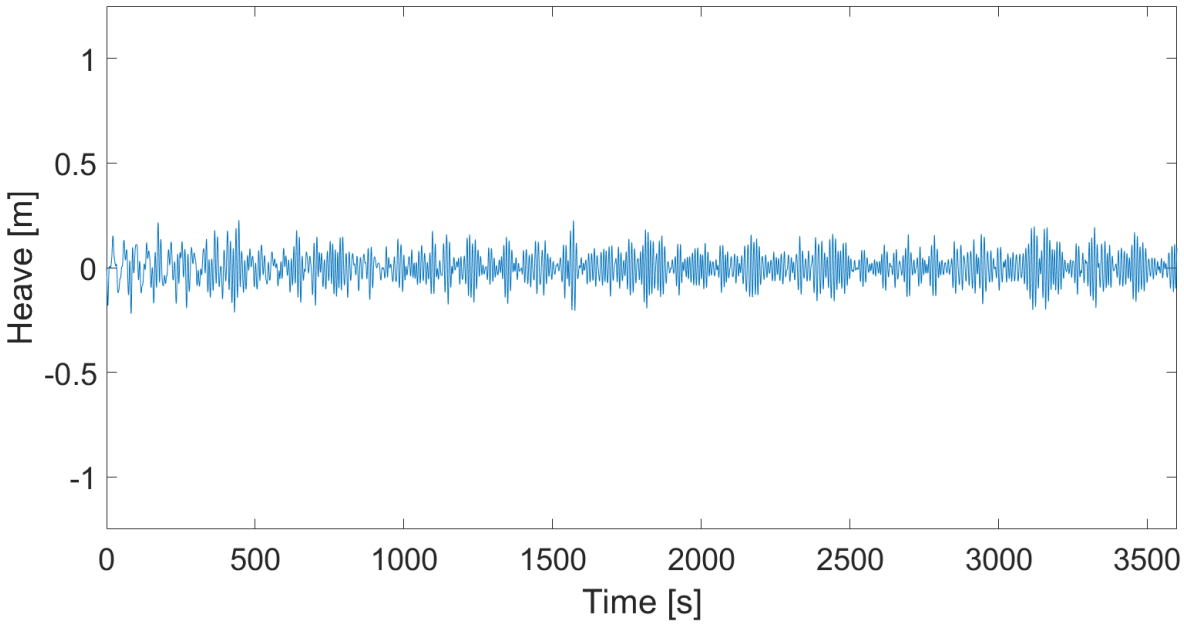

Figure 55: Dynamic response in heave, LC2, draft = 100 m

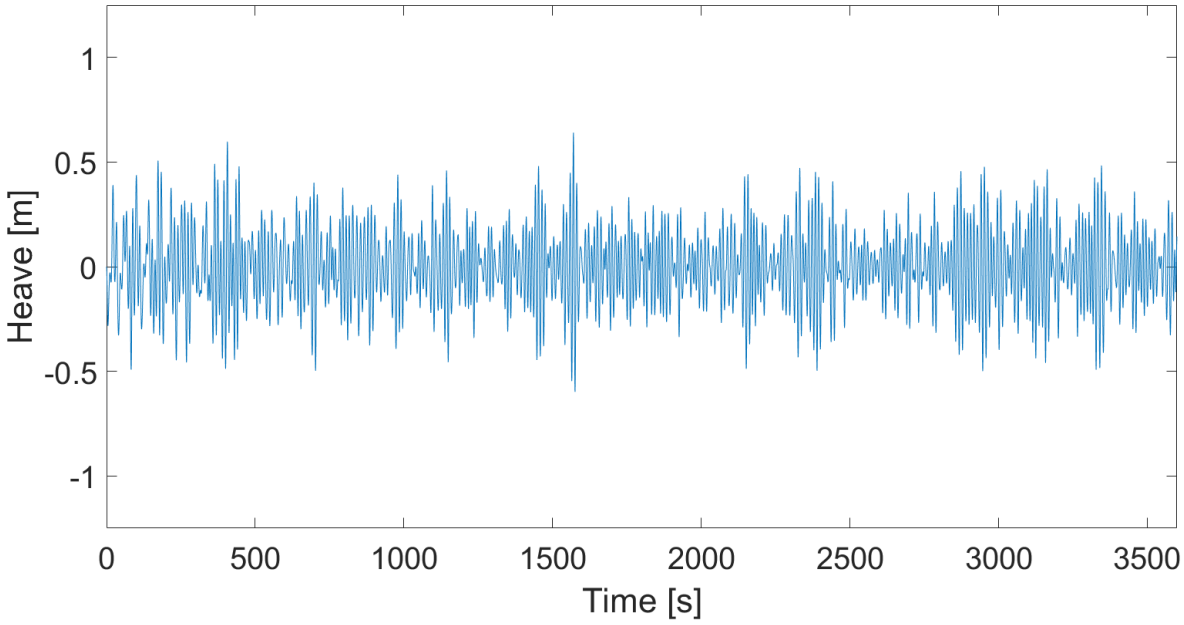

Figure 56: Dynamic response in heave, LC3, draft = 100 m

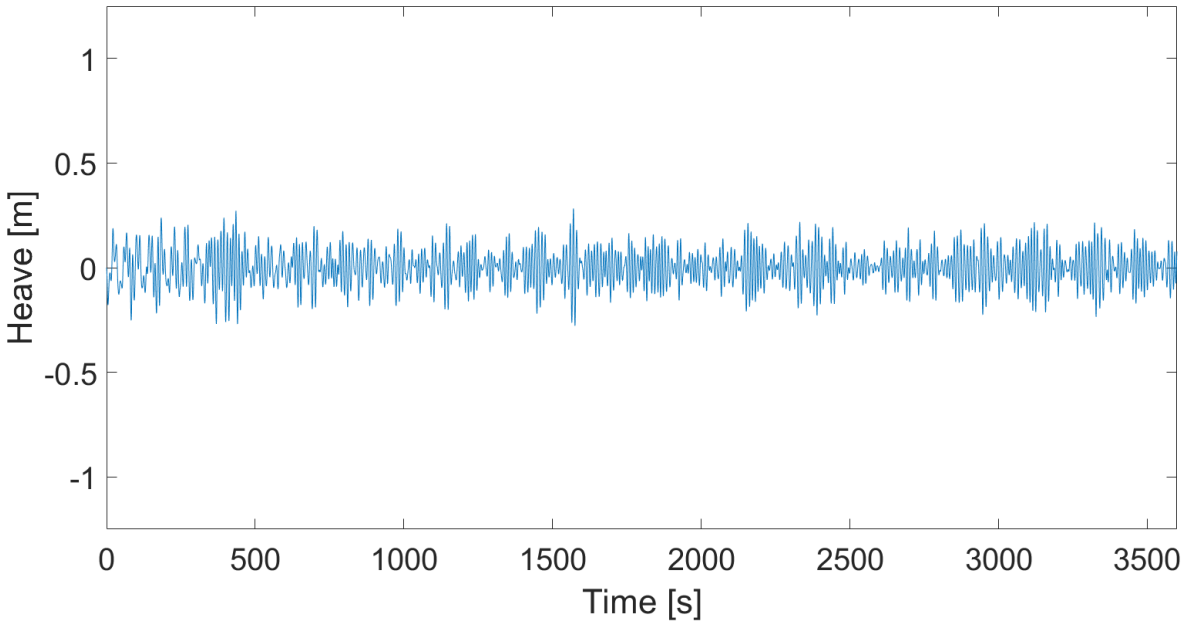

Figure 57: Dynamic response in heave, LC1, draft = 80 m

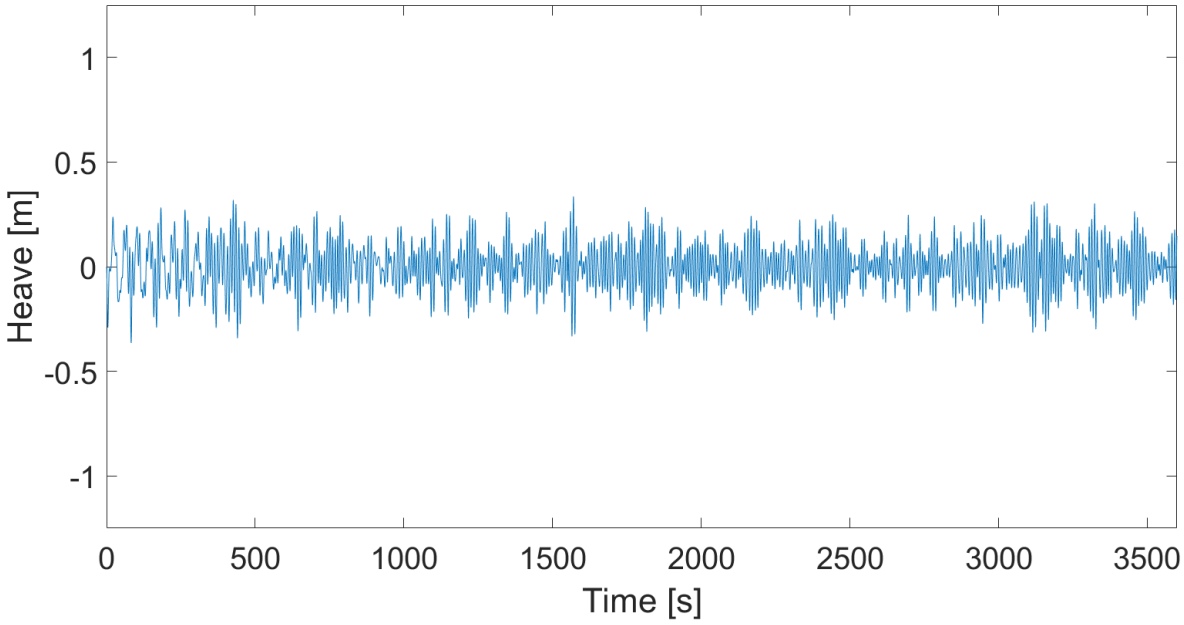

Figure 58: Dynamic response in heave, LC2, draft = 80 m

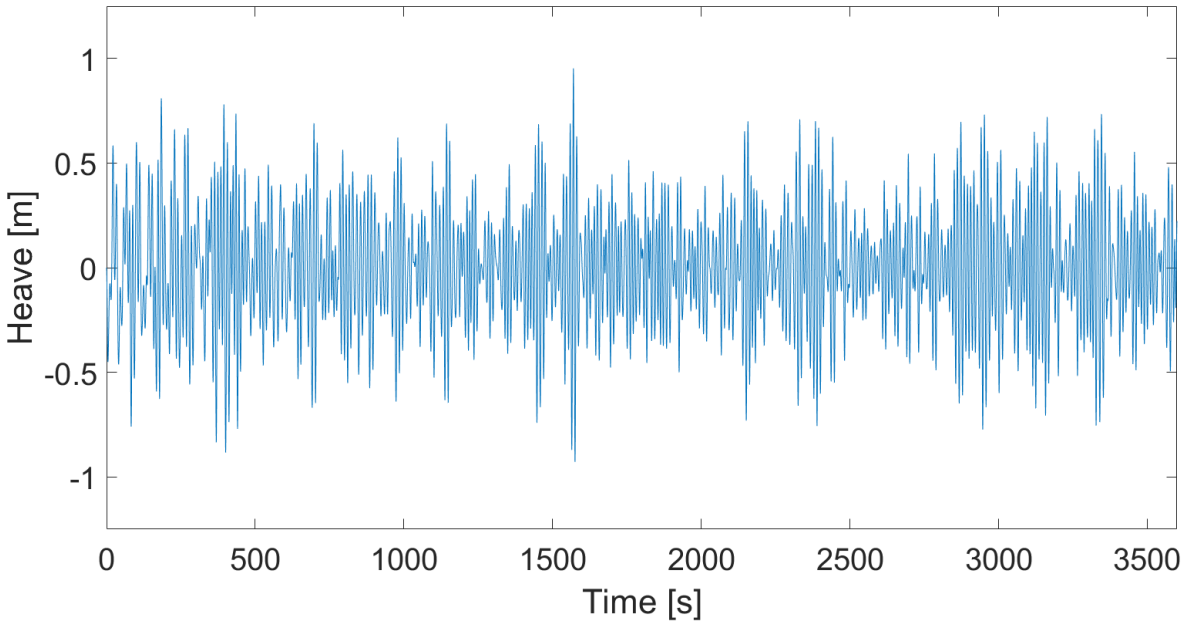

Figure 59: Dynamic response in heave, LC3, draft = 80 m

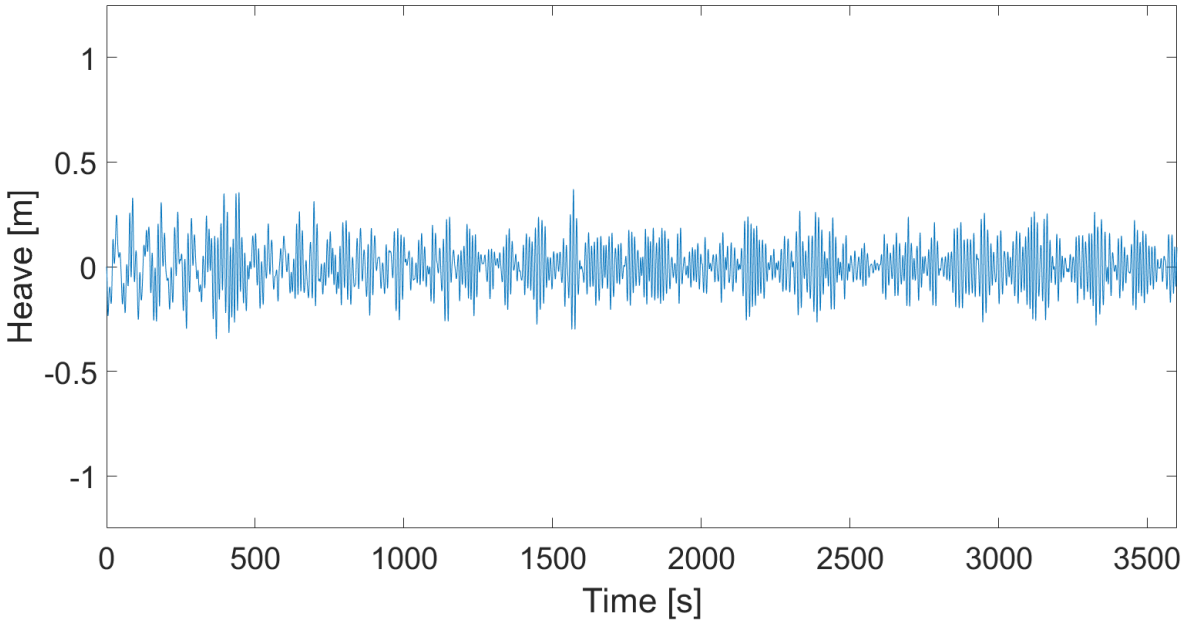

Figure 60: Dynamic response in heave, LC1, draft = 60 m

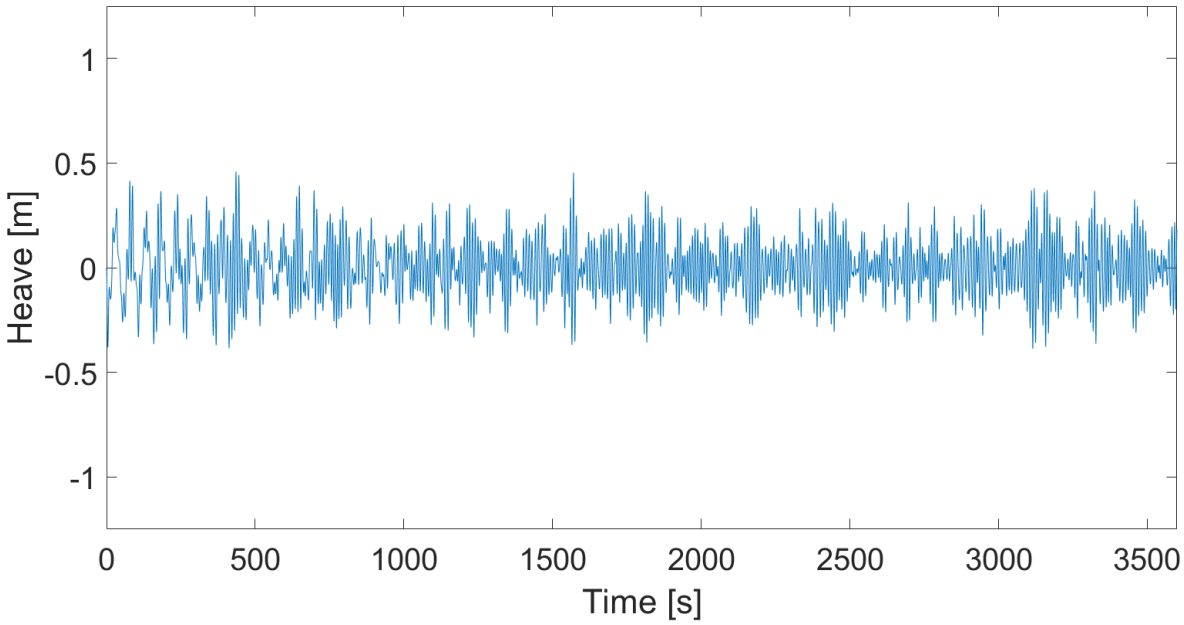

Figure 61: Dynamic response in heave, LC2, draft = 60 m

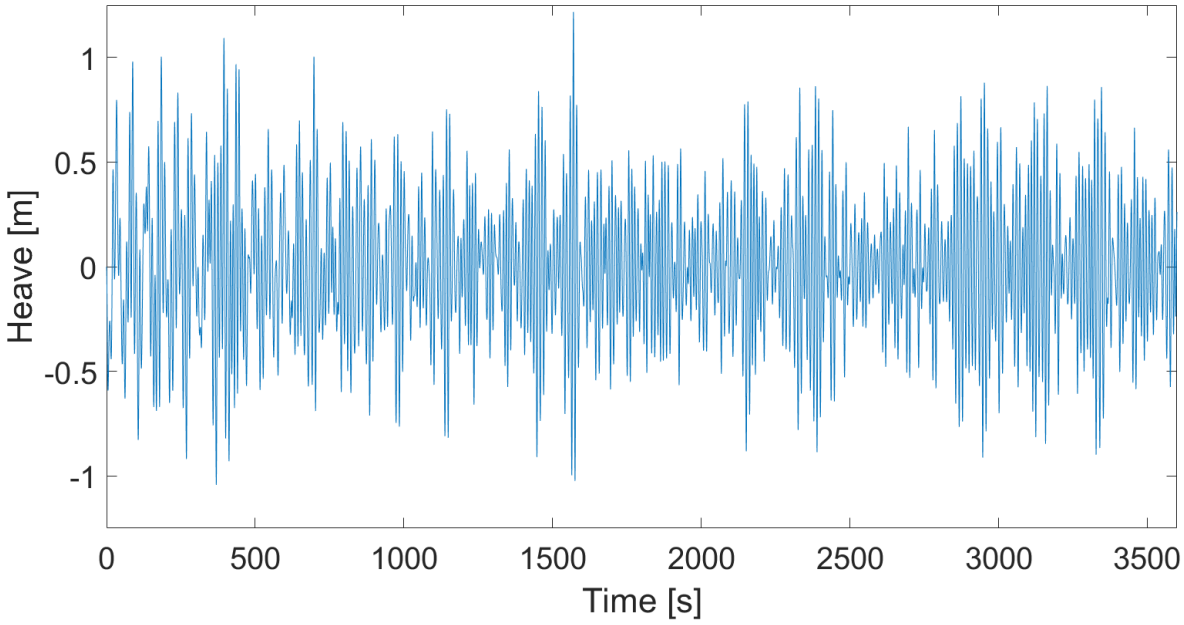

Figure 62: Dynamic response in heave, LC3, draft = 60 m

Pitch

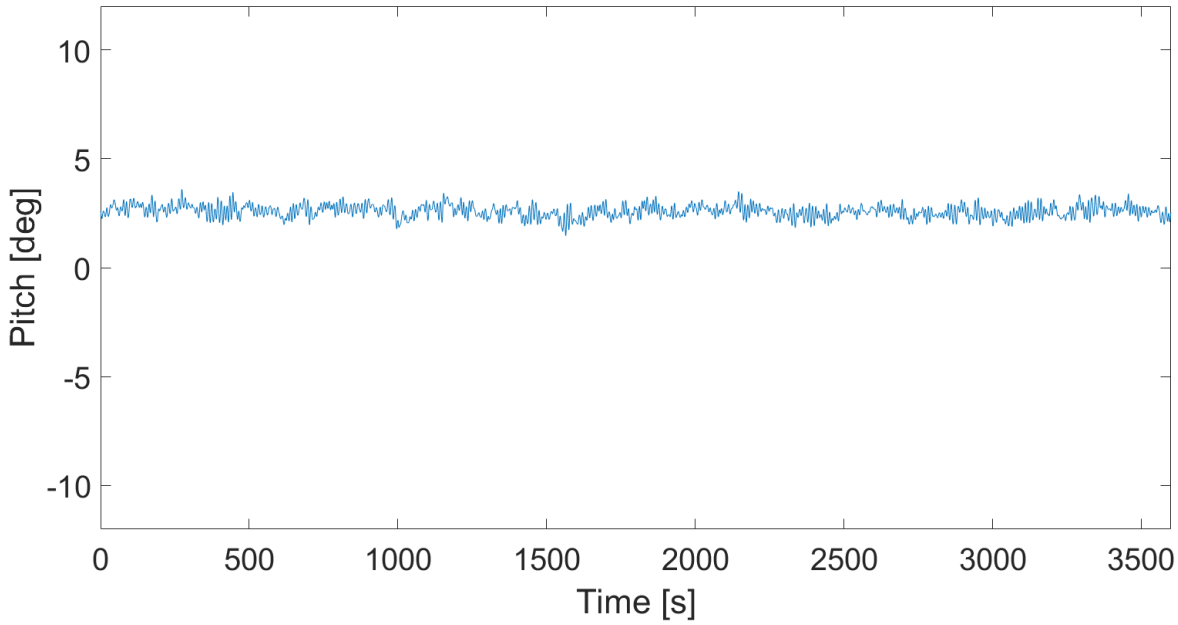

Figure 63: Dynamic response in pitch, LC1, draft = 120 m

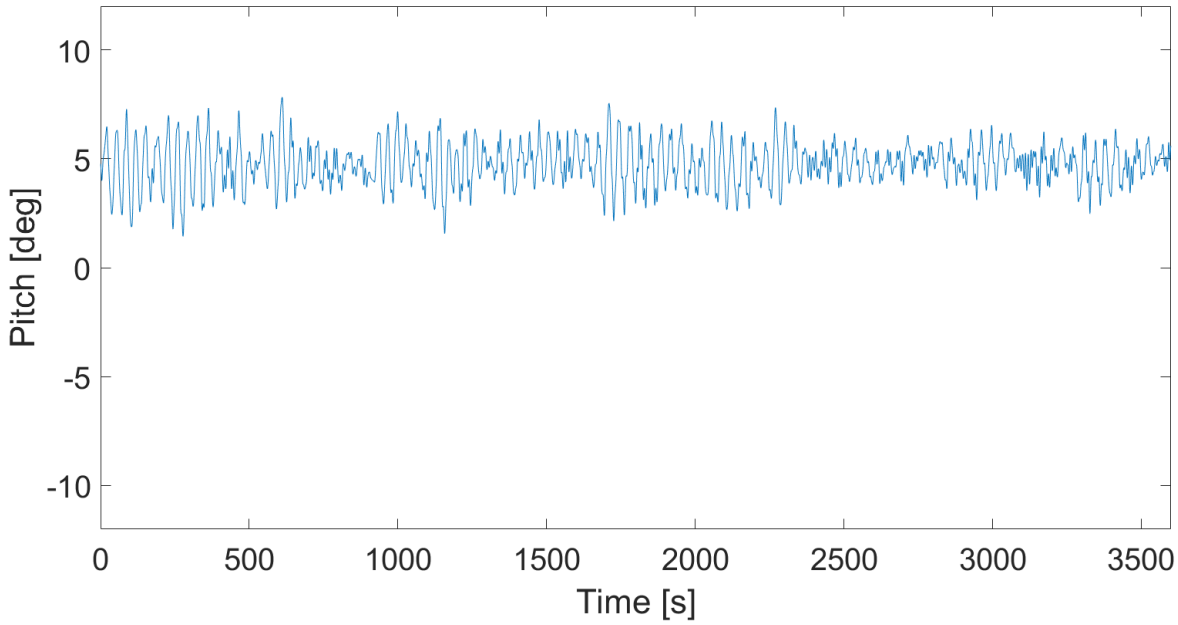

Figure 64: Dynamic response in pitch, LC2, draft = 120 m

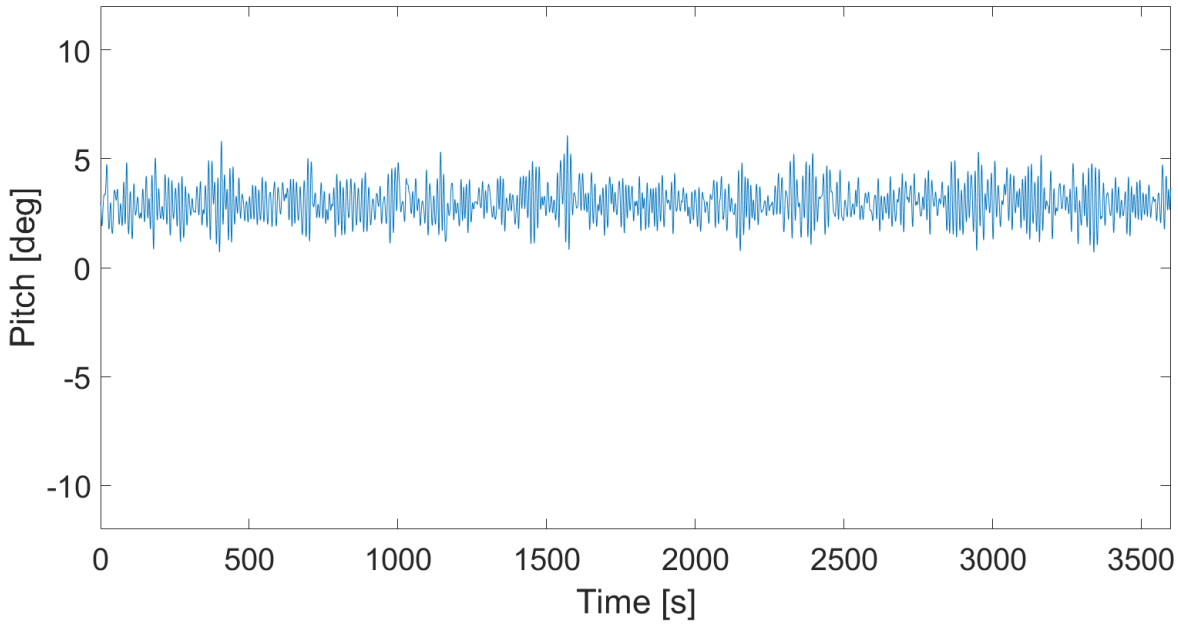

Figure 65: Dynamic response in pitch, LC3, draft = 120 m

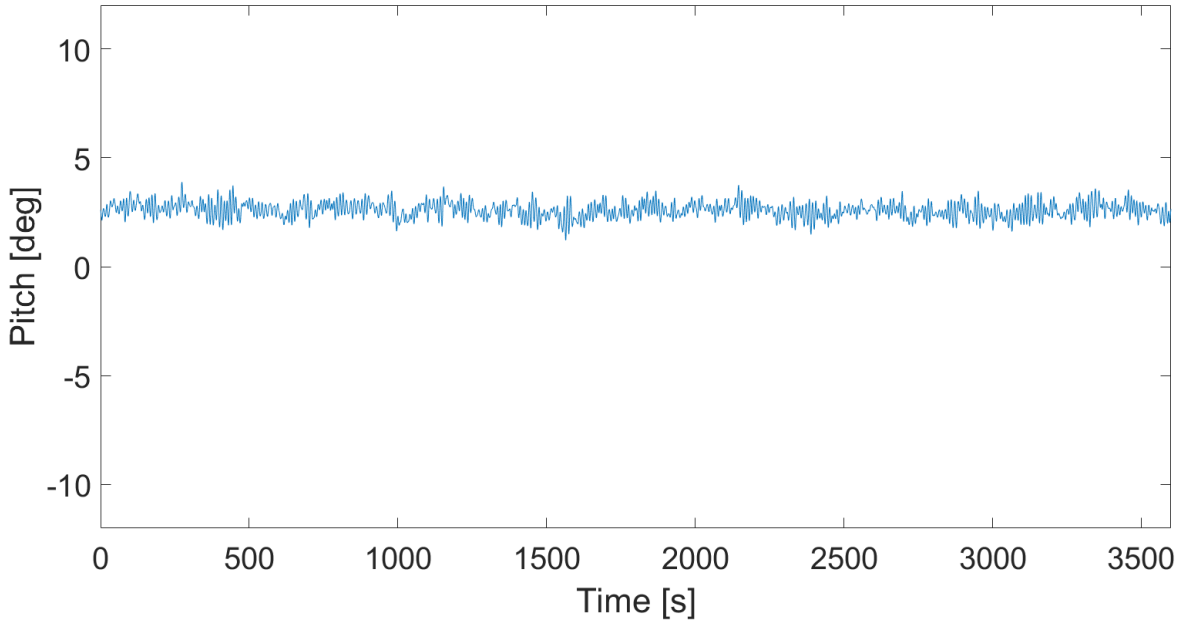

Figure 66: Dynamic response in pitch, LC1, draft = 100 m

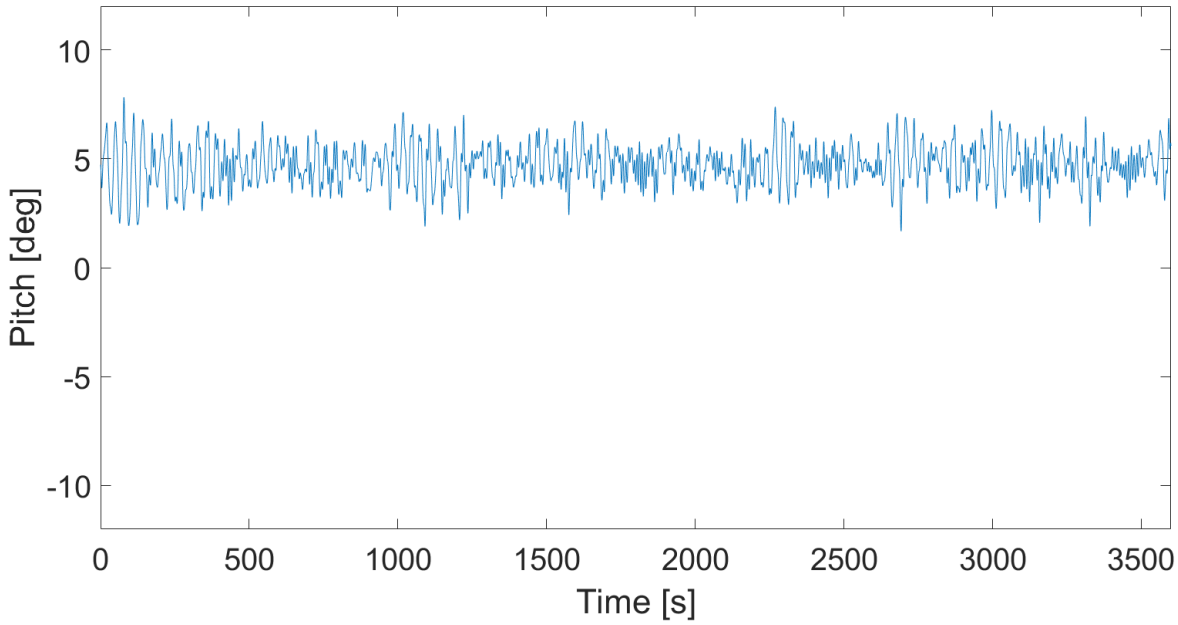

Figure 67: Dynamic response in pitch, LC2, draft = 100 m

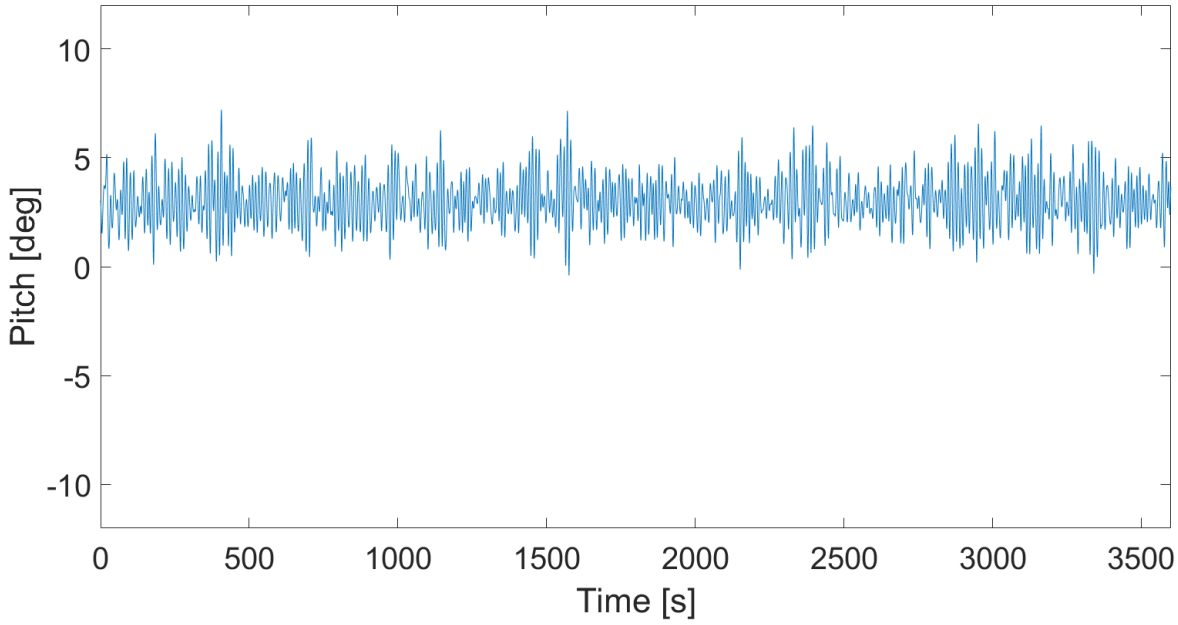

Figure 68: Dynamic response in pitch, LC3, draft = 100 m

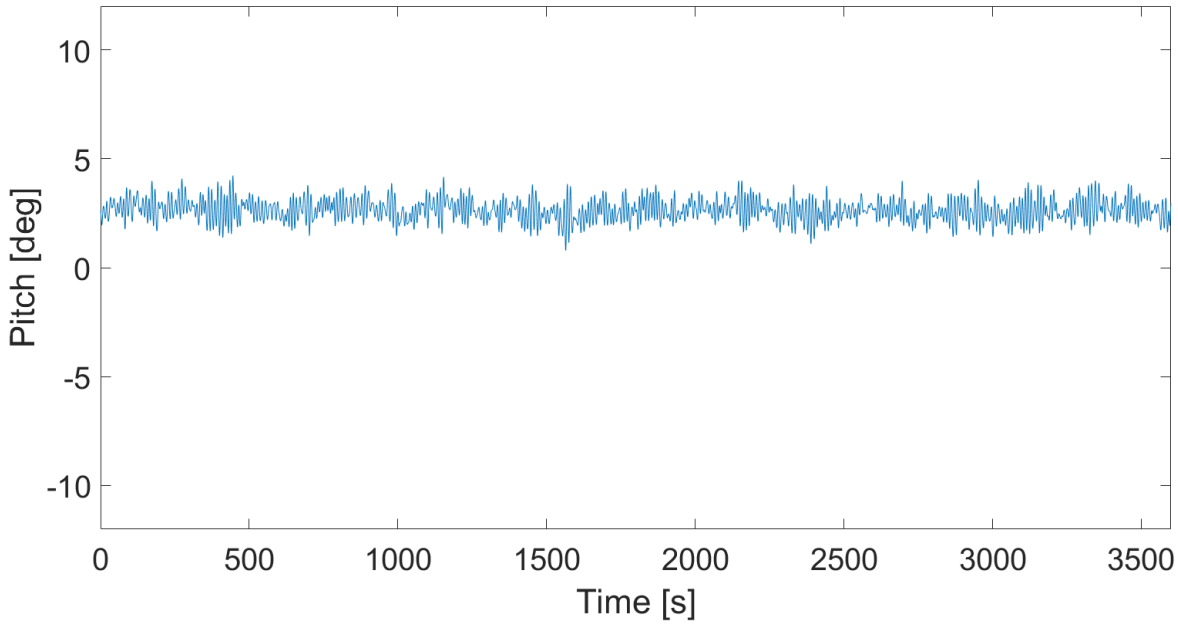

Figure 69: Dynamic response in pitch, LC1, draft = 80 m

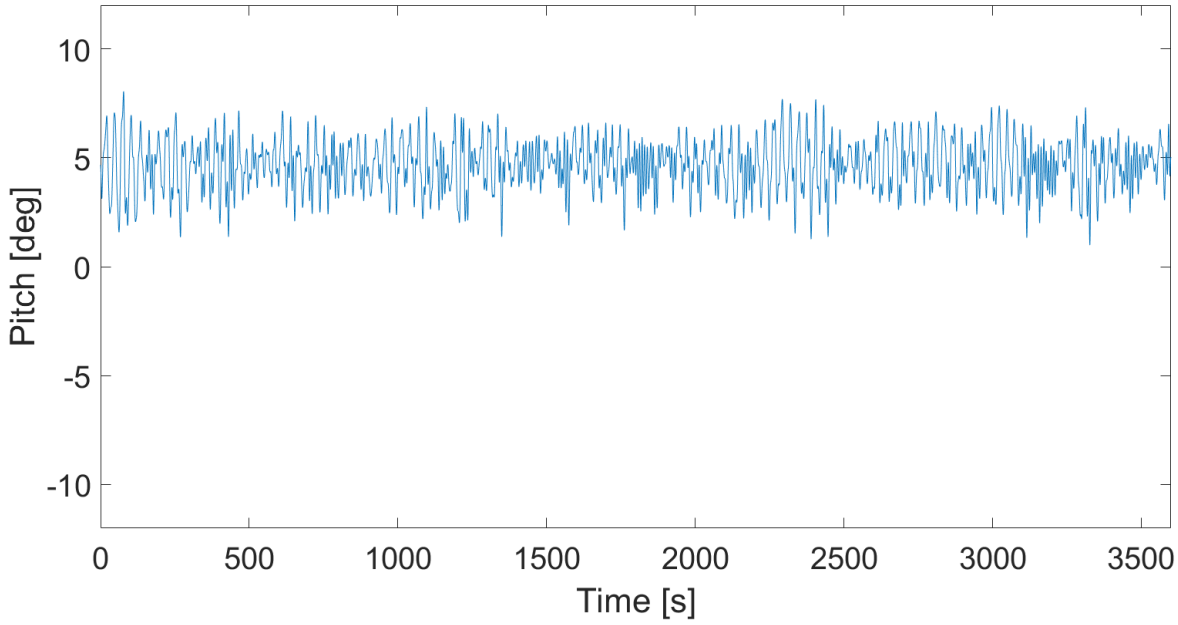

Figure 70: Dynamic response in pitch, LC2, draft = 80 m

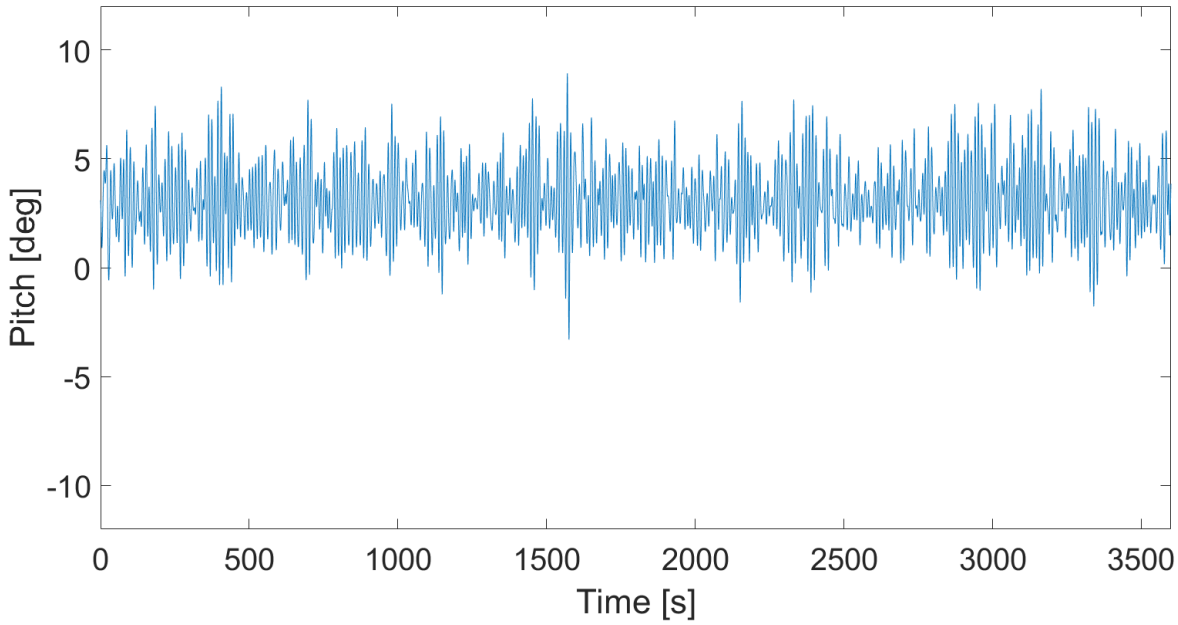

Figure 71: Dynamic response in pitch, LC3, draft = 80 m

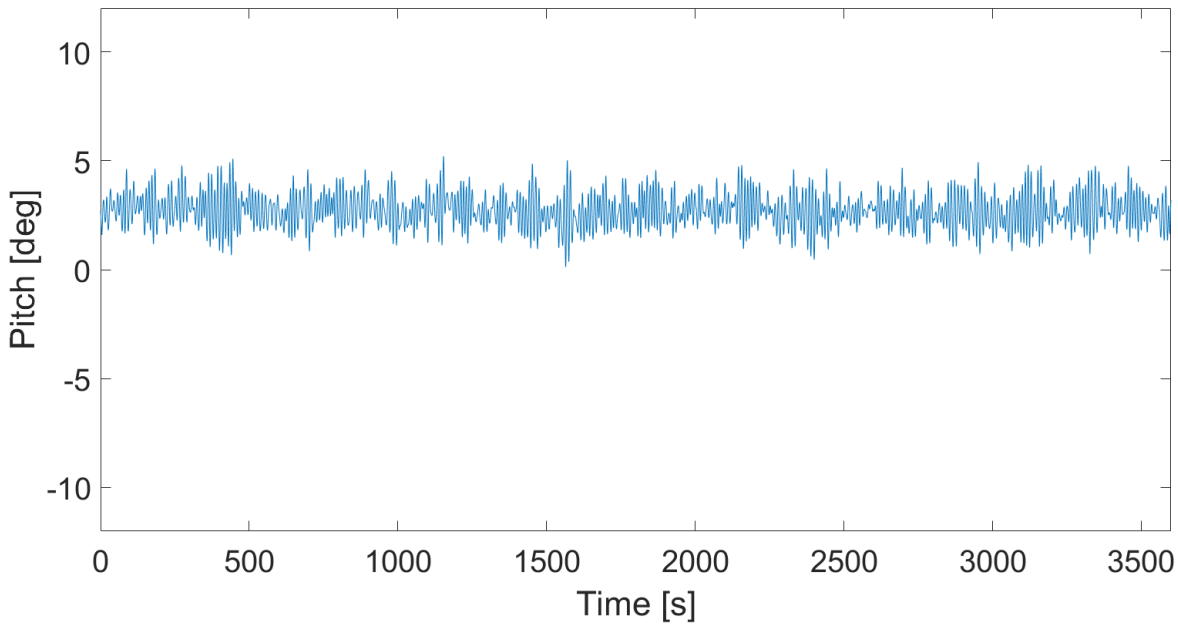

Figure 72: Dynamic response in pitch, LC1, draft = 60 m

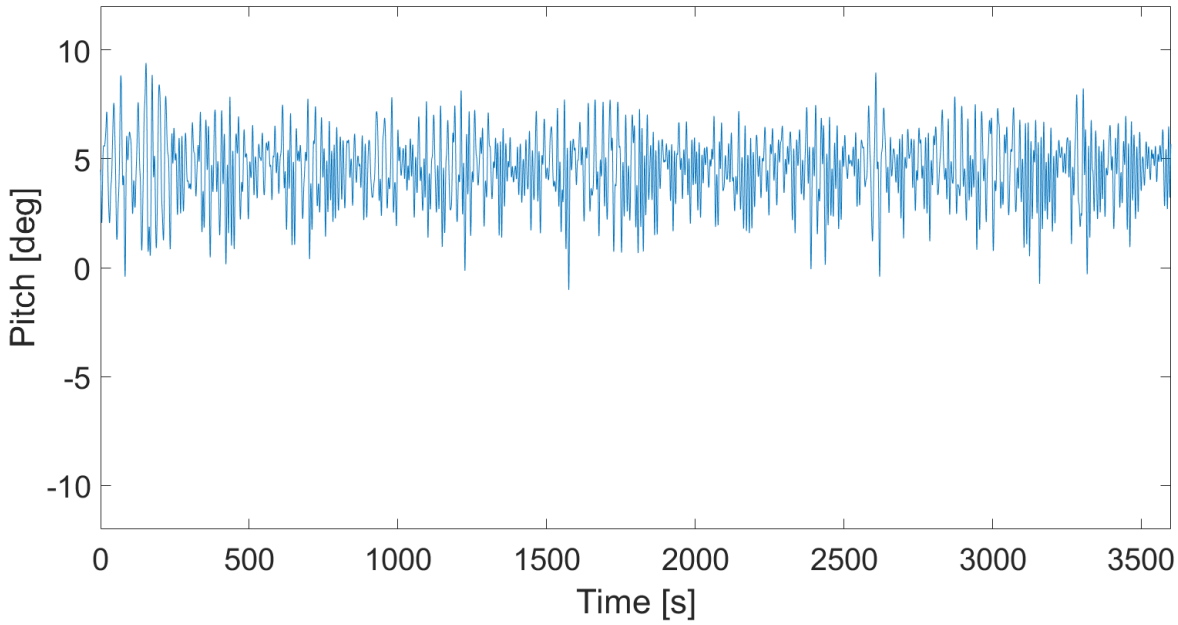

Figure 73: Dynamic response in pitch, LC2, draft = 60 m

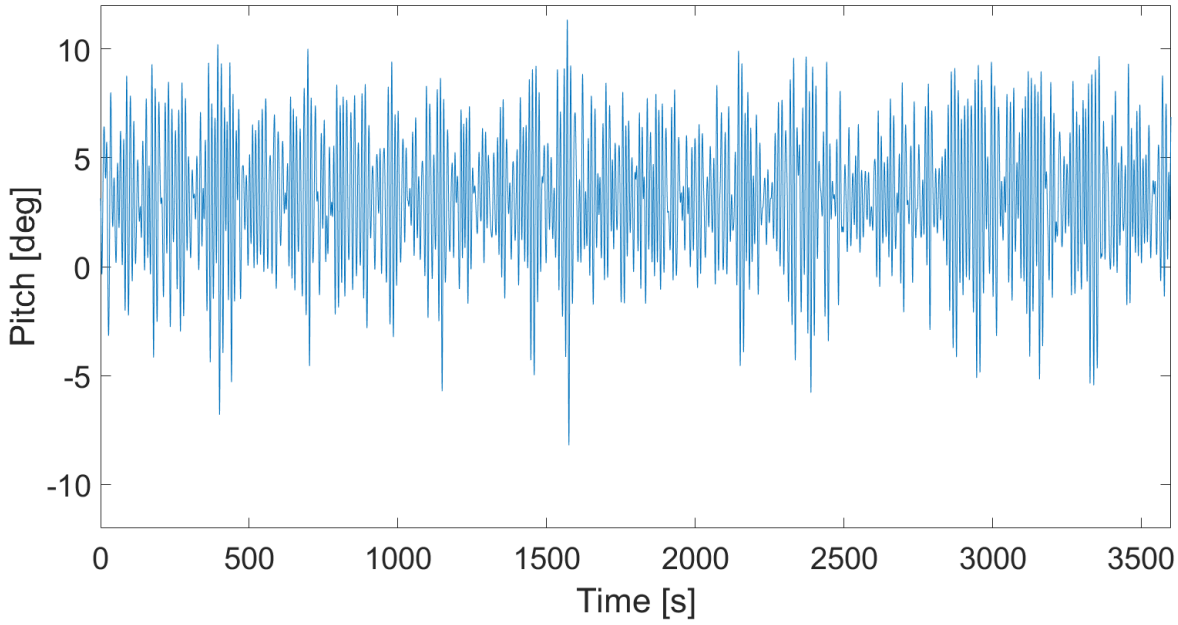

Figure 74: Dynamic response in pitch, LC3, draft = 60 m